

INFORMATION TO USERS

This manuscript has been reproduced from the microfilm master. UMI films the text directly from the original or copy submitted. Thus, some thesis and dissertation copies are in typewriter face, while others may be from any type of computer printer.

The quality of this reproduction is dependent upon the quality of the copy submitted. Broken or indistinct print, colored or poor quality illustrations and photographs, print bleedthrough, substandard margins, and improper alignment can adversely affect reproduction.

In the unlikely event that the author did not send UMI a complete manuscript and there are missing pages, these will be noted. Also, if unauthorized copyright material had to be removed, a note will indicate the deletion.

Oversize materials (e.g., maps, drawings, charts) are reproduced by sectioning the original, beginning at the upper left-hand corner and continuing from left to right in equal sections with small overlaps. Each original is also photographed in one exposure and is included in reduced form at the back of the book.

Photographs included in the original manuscript have been reproduced xerographically in this copy. Higher quality 6" x 9" black and white photographic prints are available for any photographs or illustrations appearing in this copy for an additional charge. Contact UMI directly to order.

UMI

A Bell & Howell Information Company
300 North Zeeb Road, Ann Arbor MI 48106-1346 USA
313/761-4700 800/521-0600

**ANALYSIS OF OPTICAL OBSERVATIONS AND
THREE-DIMENSIONAL HYBRID CODE SIMULATION OF THE
CRRES PLASMA INJECTION EXPERIMENTS IN SPACE**

A
THESIS

Presented to the Faculty
of the University of Alaska Fairbanks
in Partial Fulfillment of the Requirements
for the Degree of

DOCTOR OF PHILOSOPHY

By

Peter A. Delamere, B.A.

Fairbanks, Alaska

May 1998

UMI Number: 9840268

UMI Microform 9840268
Copyright 1998, by UMI Company. All rights reserved.

**This microform edition is protected against unauthorized
copying under Title 17, United States Code.**

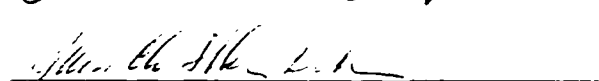
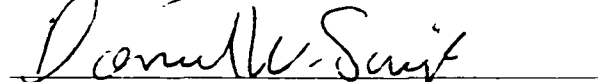
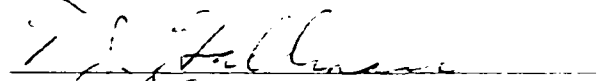

UMI
300 North Zeeb Road
Ann Arbor, MI 48103

**ANALYSIS OF OPTICAL OBSERVATIONS AND THREE-DIMENSIONAL
HYBRID CODE SIMULATION OF THE CRRES PLASMA INJECTION
EXPERIMENTS IN SPACE**

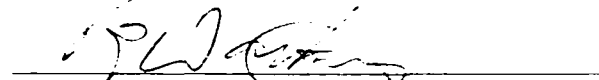
By

Peter A. Delamere

RECOMMENDED:

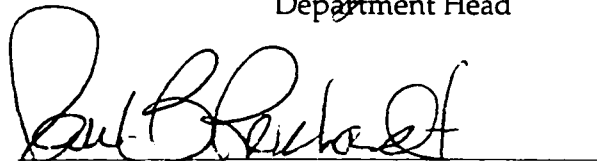


Advisory Committee Chair



Department Head

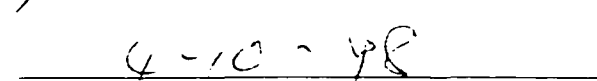
APPROVED:



Dean, College of Natural Sciences



Dean of the Graduate School



Date

Abstract

The Combined Release and Radiation Effects Satellite (CRRES) was a NASA funded campaign designed to study a variety of plasma processes in the Earth's space environment. These space plasma processes were studied using a chemical release technique whereby a neutral gas is injected into the Earth's ionosphere or magnetosphere. The neutral vapor ionizes and both neutral and ion components are optically observable which enable the direct measurement of plasma processes. The ion cloud is coupled to the ambient medium via Alfvén waves which transport momentum away from the cloud in directions parallel to the ambient magnetic field. The purpose of this study was to provide an in-depth analysis of the coupling between the release cloud and the ambient plasma while looking for signatures of Alfvén's critical ionization velocity (CIV) effect. Moreover, chemical releases represent a general physical system with broad application to such geophysical and astrophysical phenomena as cometary environments, Io's plasma torus, and the auroral regions of the ionosphere and magnetosphere.

An analysis of the optical observations from the CRRES G1, G9, and G11A releases, in conjunction with results from a three-dimensional hybrid code simulation, showed that CIV was not present and that the momentum transfer was significantly diminished by a current limiting process. The simulation results suggest that the decoupling of the ion cloud from the ambient plasma occurred via parallel electric fields associated with inertial Alfvén waves propagating in filamentary current layers at the edges of the ion cloud. The observations indicate that parallel electric fields were present, but other sources of parallel electric fields that should be considered include a variety of plasma instabilities that are appropriate to this physical system.

Contents

List of Figures	7
List of Tables	10
Acknowledgements	11
1 Introduction	12
1.1 General	12
1.2 Critical Ionization Velocity Effect	13
1.3 The Anatomy of a Chemical Release	16
1.4 Studies of Cloud Expansion Processes	18
1.5 A Hybrid Code	20
1.6 Thesis Content and Organization	21
2 Observations	23
2.1 CRRES chemical releases	23
2.2 Optical Data	26
2.2.1 G1	27
2.2.2 G9	27
2.2.3 G11A	29
2.3 Image Analysis	31
2.3.1 Vignetting corrections	31
2.3.2 Image Calibration	33
2.3.3 Ion Inventories	34
2.3.4 Ion cloud profiles	36
2.4 Summary	41

	5
3 Inferred Processes	43
3.1 General Model Considerations	43
3.2 Skidding	45
3.2.1 Calculated initial skidding distance	47
3.3 Expanding Neutral Disk	50
3.3.1 Calculated Neutral Disk Inventory	51
3.4 Ion Cloud Morphology	54
3.4.1 Polarization Electric Field Model	54
3.5 Closure	57
4 Hybrid Code	59
4.1 Algorithms	60
4.2 Time Stepping Algorithm	62
4.3 Simulation Coordinates and Grid Structure	66
4.4 Boundary Conditions	69
4.5 Energy and Momentum Conservation	70
5 Simulation Results	71
5.1 Introduction	71
5.2 G9 Release	72
5.2.1 Skidding	72
5.2.2 Ion cloud morphology	76
5.2.3 Field and fluid quantities near the release region	76
5.2.4 Field and fluid quantities away from release region	78
5.3 G1 and G11A Releases	100
5.4 Summary	106
6 Discussion and Conclusions	108
6.1 Cloud-Ionosphere Coupling	108
6.2 Neutral Disk	114
6.3 Ion Cloud Morphology	115
6.4 Conclusions	119

6.4.1	Future extensions of this study	121
A	An energy conservation theorem for the hybrid code	123
B	A momentum conservation theorem for the hybrid code	126
C	Inertial Alfvén waves	129
	Bibliography	132

List of Figures

1.1	An Ionization front	15
1.2	Chemical release cloud	18
2.1	The location of the CRRES G1, G9 and G11A releases	26
2.2	G1 observations from Aircraft 127	28
2.3	G1 cloud morphology	29
2.4	G9 observations from Aircraft 131 and Aircraft 127	30
2.5	Expanding disk of particles	31
2.6	G11A observations from Aircraft 131 and Aircraft 127	32
2.7	Image flat-fielding	33
2.8	Image calibration	35
2.9	G1 ion cloud profile from Aircraft 127 at $t = 12.0$ s	38
2.10	G9 ion cloud profile from Aircraft 127 at $t = 19.3$ s	39
2.11	G11A ion cloud profile from Aircraft 127 at $t = 30.7$ s	40
3.1	Energy parameters for the CRRES releases	44
3.2	Skidding model results for G1, G9, and G11A	49
3.3	Calculated charge exchange rates versus time	53
3.4	Early ion cloud structuring	56
4.1	The time stepping algorithm	63
4.2	An illustration of the simulation coordinate system	66
4.3	The coordinate cell	67
4.4	PIC weighting	69

5.1	Projections of the barium ion densities in the xy and xz planes	74
5.2	G9 ion distribution along the satellite path	75
5.3	Ion cloud in the xy plane with electric field.	77
5.4	Ion cloud in the xz plane with electric field.	77
5.5	Slices of the ion cloud rendered in three-dimensions	78
5.6	Field and fluid quantities in the xy plane at $z = 151$ and $t = 0.4$ s	79
5.7	Field and fluid quantities in the xy plane at $z = 152$ and $t = 0.8$ s	80
5.8	Field and fluid quantities in the xy plane at $z = 152$ and $t = 1.2$ s	81
5.9	Field and fluid quantities in the xy plane, $t = 1.6$ s	82
5.10	Field and fluid quantities in the xy plane at $z = 154$ and $t = 2.0$ s	83
5.11	Field and fluid quantities in the xy plane at $z = 155$ and $t = 2.4$ s	84
5.12	Field and fluid quantities in the xz plane at $y = 30$ and $t = 0.4$ s	85
5.13	Field and fluid quantities in the xz plane at $y = 30$ and $t = 0.8$ s	86
5.14	Field and fluid quantities in the xz plane at $y = 30$ and $t = 1.2$ s	87
5.15	Field and fluid quantities in the xz plane at $y = 30$ and $t = 1.6$ s	88
5.16	Field and fluid quantities in the xz plane at $y = 30$ and $t = 2.0$ s	89
5.17	Field and fluid quantities in the xz plane at $y = 30$ and $t = 2.4$ s	90
5.18	B_x contours in the xz plane at $y = 32$ and $t = 2.6$ s	92
5.19	B_y contours in the xz plane at $y = 35$ and $t = 2.6$ s	93
5.20	$(u_i - u_e)_z$ contours in the xz plane at $y = 32$ and $t = 2.6$ s	94
5.21	Magnetic Field topology in the xz plane at $y = 32$ and $t = 2.6$ s	95
5.22	E_x contours in the xz plane at $y = 32$ and $t = 2.6$ s	96
5.23	E_y contours in the xz plane at $y = 32$ and $t = 2.6$ s	97
5.24	u_{f_x} contours in the xz plane at $y = 32$ and $t = 2.6$ s	98
5.25	u_{f_y} contours in the xz plane at $y = 32$ and $t = 2.6$ s	99
5.26	Small release ion distribution along the satellite path	101
5.27	Small release ion distribution along the satellite path using $n_e = 5 \times 10^{11}$ (m^{-3})	102
5.28	Small release ion distribution along the satellite path with Ba-Ba ⁺ charge exchange and billiard collisions	103
5.29	Small release charge exchange rates using $1 \times$ neutral densities	104
5.30	Billiard collision rates using $5 \times$ neutral densities	105

5.31	Ion cloud in the xz plane at $y = 13$ and $t = 1.2$ s with electron pressure	106
6.1	Alfvén wave damping	111
6.2	Magnetic reconnection	114
6.3	An illustration of the mechanism for generating density gradients in the core along the magnetic field	118
A.1	Energy conservation for the large G9 simulation	125
B.1	Momentum conservation for the large G9 simulation	128

List of Tables

1.1	CIV chemical releases	16
1.2	Chemical Properties for CRRES releases	17
2.1	CRRES (low altitude) Sunlit Release Experiment Parameters	25
2.2	Emission rates for a barium cloud in full sunlight	36
2.3	A summary of the observations made of the CRRES G1, G9, and G11A sunlit barium releases	42
5.1	Parameters for the five hybrid code simulation runs of the CRRES releases .	73

Acknowledgements

Behind every thesis is a great support crew. Foremost is the committee. I started my graduate career thanks entirely to my committee chair, Professor Hans Nielsen. He paved the way by bringing me to Alaska as a summer intern during the summer of 1990. After flying me to the Brooks Range, and Denali National Park for weekend backpacking trips and providing a simulating summer research project there was no turning back. The following summer I returned to Alaska to start graduate school. The first four years were spent working with Hans on analysis of the optical observations of the CRRES releases. Following the optical data analysis I commenced the hybrid code simulation project with Professor Dan Swift. Dan's ability to motivate is unparalleled. His insights into coding errors and patience during the debugging phase were greatly appreciated. To the other three committee members, Tom Hallinan, Roger Smith, and Gene Wescott go many thanks for insightful comments and helpful discussions.

Secondly I would like to thank the my fellow graduate students and friends for making the experience so much fun! Thanks first to the office mates, Don Hampton, Geoff McHarg, and Curt Szuberla. Other graduate students include Will Cantrell, Fred Hall, Matt Heavner, Tom Immel, Moose Kimball, Dana Moudry, Andy Nicholas, Laura Peticolos, John Williams, and Ryan Woodard. Friends include many members of the Nordic Ski Club of Fairbanks, the Front Street gang, and everybody who has ever set foot on the ultimate field in Fairbanks.

Lastly, and really most importantly, thanks to the Toad who is soon to be my life partner. It must have been miserable to return home with me every day during the debugging phase. But she still apparently likes me. The wedding is scheduled for July 25, 1998.

Chapter 1

Introduction

1.1 General

Chemical release techniques have been employed in ionospheric and magnetospheric research since the advent of the research rocket in the 1950s [Davis, 1979; Haerendel, 1986]. Early releases of sodium, lithium, aluminum and nitric oxide at altitudes above 50 km were used as tracers of atmospheric transport processes. Later, in the 1960s and 1970s, the use of barium in thermite and shaped charge release techniques provided optically observable ion and neutral components in the release vapor, enabling the measurement of plasma processes in the Earth's space environment. These plasma releases have been used in a wide range of such geophysical applications as the production of artificial comets, auroral studies, geomagnetic field line tracing, and particle trapping in the Van Allen belts.

Recently a series of chemical releases were made as a part of the NASA's Combined Release and Radiation Effects Satellite (CRRES) campaign. These releases were designed to study a variety of basic plasma processes in the space environment [Bernhardt, 1992; Reasoner, 1992]. The first set of releases, made in the fall of 1990, were designed to investigate the critical ionization velocity (CIV) effect in space [Wescott et al., 1994]. The second series of releases, made in the summer of 1991, were designed to study such processes as diamagnetic cavity formation, structuring of the expanding plasma, plasma wave dynamics, magnetic conjugacy, and the coupling between a release and the ambient ionospheric plasma.

Of particular interest here is the CIV effect. CIV has been verified in laboratory experiments [Piel, 1990; Danielsson, 1973]; however, the results from a variety of rocket-borne CIV experiments [Haerendel, 1982; Stenbaek-Nielsen et al., 1990b,a; Torbert, 1990] and the CRRES campaign are inconsistent at best. These results have generated considerable interest in the topic and have provided the motivation for this thesis.

In an attempt to isolate observable signatures of the CIV process, we broadened our analysis to a general investigation of all physical processes that are associated with the early phase ($t < 5$ s) of a barium release. The goal is to identify observable morphological features in a barium cloud and affiliate each feature with a specific physical process. For the analysis we used video data from the CRRES G1, G9 and G11A releases in conjunction with the results from a three-dimensional hybrid code simulation. Although CIV provided the motivation for the study, the results from the simulation are applicable to the general system of an ionizing neutral gas streaming across an ambient magnetized plasma. Thus the results are relevant, for example, to cometary environments and to the design of future release experiments.

1.2 Critical Ionization Velocity Effect

The critical ionization velocity (CIV) effect occurs when a neutral gas ionizes while passing through a magnetized plasma. [Newell, 1985; Piel, 1990; Torbert, 1990; Brenning, 1992]. The requirement for the CIV ionization is that the neutral gas traverse a magnetized plasma with a relative critical velocity that is perpendicular to the magnetic field. This critical velocity corresponds to the kinetic energy that equals the ionization potential of the neutral particles, or

$$\frac{m_n v_{cr}^2}{2} = e\phi_i \quad (1.1)$$

where m_n is the mass of the neutral particles, v_{cr} is the critical velocity in the plasma reference frame, and $e\phi_i$ is the ionization energy. If the velocity exceeds v_{cr} , then free energy is available for the plasma interactions that drive a self-sustaining ionization mechanism.

The CIV effect was first proposed by *Alfvén* [1954] in his band structure theory on the origin of the solar system. He theorized that neutral gases accelerating gravitationally toward a central body (the sun) will ionize via the CIV mechanism. The subsequent ionized

gas will then experience a Lorentz force due to the magnetic field of the central body (IMF) and concentrate toward an equatorial plane as dictated by the field lines. The accumulation of mass, according to his theory, will occur at a distance

$$R_i = \frac{GMm}{e\phi_i} \quad (1.2)$$

from the central body where G is the gravitational constant, M is the mass of the central body, m is the mass of the gas particles. This suggests that mass will accumulate at various distances as governed by the critical velocity given in equation 1.1. For instance, O, C, N, and Ne have critical velocities of roughly 13 km/s which corresponds to the region (band) where Jupiter, Saturn, Uranus and Neptune lie. However, the chemical composition of these planets do not consistently resemble the bands that supposedly gave rise to their formation. As a result, Alfvén's theory is not widely accepted. But successful laboratory CIV experiments have sparked continued interest in potential applications of the CIV mechanism in space physics and astrophysics. Some of these applications include cometary coma ionization [Formisano et al., 1982], Io's plasma torus [Galeev and Chabibrachmanov, 1983], space shuttle glow [Hunton, 1989], and the lunar transient phenomena [Cameron, 1991]

A fully self-consistent theory for the CIV effect has yet to be formulated, though considerable progress has been made by *Moghaddam-Taaheri and Goertz* [1993] with their numerical quasi-linear study. Perhaps the most common element to any CIV theory is the role of the modified two-stream instability for electron heating [McBride et al., 1972; Möbius, 1983]. Given a seed ionization mechanism (i.e. photoionization or collisional processes), polarization charge layers form at the boundaries of the cloud as the heavy ions out run the magnetized electrons as shown in figure 1.1. The ions are assumed to be unmagnetized for time scales $\ll \omega_i$ (the ion gyrofrequency). The resulting electric field that is set up by the charge separation gives rise to subsequent $\mathbf{E} \times \mathbf{B}$ drift of the electrons which excites waves described by the modified two-stream instability. This instability can heat the electrons to energies in excess of the neutral ionization potential and electron-neutral collisions complete what is now a feedback process. If the neutral densities are high enough to allow for at least one electron-neutral collision then the feedback process can result in an avalanche of ionization [Brenning, 1982].

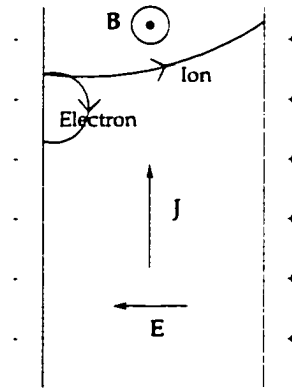


Figure 1.1: An ionization front. Note the charge separation and the cross field current J associated with the electron $E \times B$ drift.

Another possible mechanism for electron heating was proposed by *Machida* [1986] where heating arises from elastic collisions of electrons with neutrals. In this model the neutrals are again considered streaming with velocity v perpendicular to a strong magnetic field. Upon ionization, the electron is magnetized and in the frame of reference of the neutral beam there is a static electric field given by $E = v \times B$. In this frame the electrons drift opposite to the electric field and gain energy through elastic collisions with the neutrals. This heating mechanism is referred to as resistive heating as it is associated with the Pedersen current. Clearly, this "resistive" CIV requires a high neutral density whereas the heating via modified two-stream instabilities can be relatively low.

The first experimental indication of CIV in space plasmas was from the lunar impact measurements with the Apollo 13 launch vehicle on April 13, 1970. [*Newell*, 1985]. The impact liberated a cloud of neutral particles comprised of vaporized plastics from the rocket as well as lunar surface particles. As the gas bubble expanded into the solar wind and into the sunlight a small population of photoions were expected. However, the actual number of ions observed suggested the presence of an additional ionization mechanism, possibly CIV.

More recently, a number of experiments using chemical releases have been conducted to test the CIV effect in space. Table 1.1 summarizes the results these CIV experiments. *Moghaddam-Taaheri and Goertz* [1993] demonstrated that the fastest growing mode of the lower-hybrid waves generated from the modified two-stream instability will resonate with

Experiment	Angle to B	% ionization	Reference
Chachalaca	10-15 °	~5	Wescott et al. [1975]
Porcupine	28 °	24-32	Haerendel [1982]
Bubble Machine	90 °	10 ⁻⁴	Deehr et al. [1982]
Star of Lima	90 °	< 2 × 10 ⁻³	Wescott et al. [1986b]
Star of Condor	all angles	< 3 × 10 ⁻⁵	Wescott et al. [1986a]
George Orwell	90 °	0	Newell [1985]
Crit I	45 °	< 10 ⁻²	Torbert et al. [1992]
Crit II	57 °	0.6	Stenbaek-Nielsen et al. [1990b]
SR90	45 °	0	Wescott et al. [1990]
CRRES (CIV I, CIV II)	80 °	0.014, 0.40	Wescott et al. [1994]

Table 1.1: CIV chemical releases

the electrons most efficiently at a release angle, $\theta = 30^\circ$, to the magnetic field. This is consistent with the Porcupine results [Haerendel, 1982]. However, they also point out that the time scale for CIV ignition for a 90° release should be the same as the 30° case because of the availability of more free energy. Why then are the ion yields so small for the other experiments? Further complications for the analysis arise when other competing ionization mechanisms are considered as a source of contamination to the observed ion yield. Other ionization processes to consider are charge stripping, charge exchange, and associative ionization. Investigations of these competing ionization mechanisms have been made by Hampton [1996]; Hunton [1995]; Hunton et al. [1997]; Wolf and Hunton [1997]. Hampton [1996] found that charge exchange is the dominant collisional process in the CRRES CIV releases and that contributions from CIV are extremely small. These results therefore pose a serious challenge for a definitive identification of the CIV processes in the CRRES chemical releases.

1.3 The Anatomy of a Chemical Release

Techniques for injecting chemical vapor into the ionosphere and magnetosphere include the shaped charge and thermite releases. Shaped charges provide an anisotropic vapor beam, either confining the vapor to a plane (radial) or to a narrow beam (conical). Shaped charges are commonly used for rocket experiments for the purpose of injecting the vapor

Species	Mass (AMU)	Photoionization time constant (sec)	Emission Lines	
			Neutral (nm)	Ion (nm)
Lithium	7.0	3450	670.8	19.9
Calcium	40.0		422.7	396.8
Strontium	87.6	2000	460.7	421.6
Barium	137.3	28	553.5	455.4
Europium	152.0		466.2	420.5

Table 1.2: Chemical Properties for CRRES releases

along or across the magnetic field. Thermite releases, used in CRRES, provide an isotropic distribution of vapor relative to the release canister where the bulk flow of the cloud with respect to the magnetic field is given by the satellite velocity. The discussion that follows will be confined to the CRRES thermite releases.

The relatively low ionization potentials (5-6 eV) of Lithium, Calcium, Strontium, Barium, and Europium make these elements appropriate for plasma releases. All have emission lines in or near the visible for the additional requirement of making optical observations. Table 1.2 summarizes the properties of the CRRES chemicals *Bernhardt* [1992]. Barium provides an excellent combination of prompt ionization and optically observable fluorescent and resonant emission lines. Detailed studies of barium emission rates have been performed by *Stenbaek-Nielsen* [1989]; *Stenbaek-Nielsen et al.* [1993] enabling reliable ion inventories for the observed release clouds.

The CRRES releases proceeded via an exothermic boron-titanium reaction that burned at a temperature of 2750 K, vaporizing roughly 40% of the release element [*Huba et al.*, 1992b,a]. Observations of the CRRES CIV release clouds by *Wescott et al.* [1994] provided a velocity distribution of the neutral vapor of the form

$$f(v) = e^{-[(v-v_0)/v_{th}]^2} \quad (1.3)$$

where v is the radial velocity, $v_0 = 1.33$ km/s and $v_0/v_{th} = 4.5$. The spherical shell of vapor moved at satellite velocity (~ 9.5 km/s) leaving behind a trail of magnetized ions (figure 1.2).

The releases were generally made during local dawn or dusk so that the optical sites were in darkness and the release cloud was exposed to sunlight. The CIV releases were

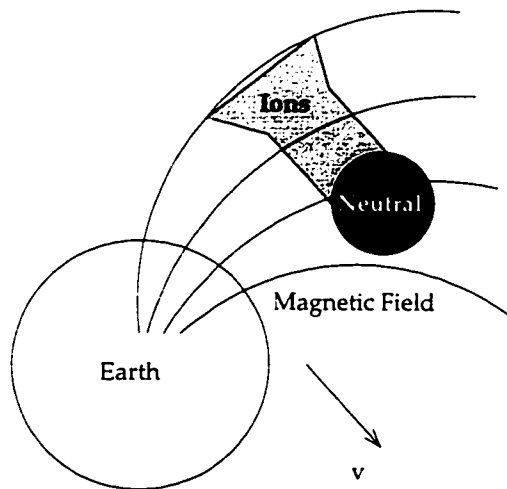


Figure 1.2: Chemical release cloud. Schematic (not to scale) of a typical chemical release cloud. Initially the neutral cloud moves in the direction indicated at satellite velocity leaving behind a trail of ions.

made just below the solar terminator to isolate the non-photoionization processes, and the geographic location of the release was selected so that any ions created would move up the magnetic field and into sunlight where they could be observed. The CRRES G1, G9, and G11A releases, analyzed in Chapter 2, were all fully sunlit barium releases.

1.4 Studies of Cloud Expansion Processes

Much of the previous work on the expansion processes of a chemical release cloud is relevant to the early ($t < 5$ s) phase of the release, though long-term processes have also been examined [Milinevsky et al., 1993; Hunton, 1993]. Interest stems primarily from observed morphological characteristics of the ion clouds and from in situ measurements of densities, temperature, and field quantities.

In the case of a passive release, designed such that the ions serve as tracer particles, one would expect a distribution of ions across the magnetic field that is consistent with the velocity distribution of the neutrals and the ionization time constant. In the case of the CRRES releases, a uniform and amorphous ion cloud should result. This is, however, not the case. Irregularities, striations, and density inhomogeneities are commonly observed.

For many years, field-aligned striations and other small scale inhomogeneities have been scrutinized [Linson and Workman, 1970; Davis et al., 1974; Goldman et al., 1976; Bernhardt et al., 1993; Milinevsky et al., 1994]. These field-aligned structures develop in times ranging from seconds to minutes after the release. The striations are elongated with respect to the rest of the cloud which suggests a modification to the particle velocity distribution. Plasma instabilities such as the gradient drift and Farley-Buneman instabilities have been cited as the cause of these striations [Gokhman and Ivanov, 1991; Blaunstein et al., 1993]. However, Zaitsev et al. [1996] and Scales and Bernhardt [1991] have both found, using two-dimensional electrostatic computer models, that ion filaments occurring within seconds after the release could be explained by non uniform polarization of the ion cloud which causes bifurcation on the back side of the cloud. Bernhardt et al. [1993], on the other hand, suggests that short-term striations can also arise from a so-called "cyclotron bunching" effect. This is a geometric effect from the ion cyclotron motion that occurs when the perpendicular injection velocity of the neutrals is greater than the characteristic expansion speed of the cloud. As the ions gyrate, density inhomogeneities separated by a distance given by $\lambda = 2\pi v_n / \omega_i$ occur, where v_n is the injection velocity and ω_i is the ion gyrofrequency. These density inhomogeneities can lead to both field-aligned striations and non-field-aligned irregularities.

Another avenue of interest deals with polarization charge layers associated with the chemical release. These charge layers form due to charge separation at the boundaries of the ion cloud as demonstrated by Galvez and Borovsky [1991] with two-dimensional electrostatic particle-in-cell computer simulations. In situ measurements of the resultant electric fields and plasma waves were made by Koons and Pongratz [1981]; Koons and Roeder [1995] and Brenning et al. [1991b]. Brenning et al. [1991a] demonstrated that these electric fields significantly affected the barium ion motion. Related studies have also been made regarding space charges surrounding rocket payloads [Neubert et al., 1990; Gatsonis and Hastings, 1992], and results applied to the chemical release environment as well. [Gatsonis and Hastings, 1991; Neubert et al., 1992].

If the polarization electric fields are sufficiently strong, then the ion cloud can $\mathbf{E} \times \mathbf{B}$ drift across the magnetic field. This drift motion of the ion cloud was observed in the CRRES releases, but only during the early phase of the release. An initial simulation study

of this process, termed "skidding", was provided by *Huba et al. [1992b]* who found that the "skidding" of the cloud was limited to within the first 2 seconds due to current dissipation in the ambient plasma. It should be noted, however, that the analysis in chapter 2 shows that much of the cloud skidded for at least 6 to 10 seconds. Issues regarding the transfer of momentum from the cloud to the ambient plasma are clearly important and will be revisited later in the thesis.

Finally, a number of relevant computer simulation studies have been made. *Ma and Schunk [1990]* started with a two-dimensional model for plasma expansion in the ionosphere which later was developed into a three-dimensional code [*Ma and Schunk, 1991*]. Their code was then applied directly to barium clouds [*Ma and Schunk, 1993*] and later included the coupling of the cloud to the ambient ionospheric plasma [*Ma and Schunk, 1994*]. *Neubert et al. [1992]* developed a three-dimensional electromagnetic code for investigating the dynamics of low- β plasma clouds. This code treated the cloud as a uniform distribution of plasma and successfully demonstrated many of the fundamental features of the system including polarization charge layer formation and the associated ambient response which inhibited cross-field motion of the plasma. In an effort to estimate an upper limit to anomalous ion production for CIV release experiments, *Biasca et al. [1993]* developed an implicit particle-in-cell (PIC) code. This code simulated a neutral beam (nitric oxide) propagating across an ambient oxygen plasma with electron elastic collisions, non-resonant and resonant charge exchange and electron impact ionization.

1.5 A Hybrid Code

Our goal for modeling a chemical release is to include both ion kinetic effects¹ and the momentum coupling to the ambient ionospheric plasma. The gyroradius of a barium ion at 450 km in the equatorial ionosphere is roughly 0.5 km. The momentum coupling proceeds via Alfvén waves which propagate in the ionosphere with velocities of order 10^2 to 10^3 km/s. This poses a serious challenge to the computational feasibility of this problem.

¹The term "kinetic" pertains to the motion of particles. Kinetic effects refer to processes that result from the individual particle motion rather than the average motion of the particles in the plasma. Fluid models consider only the average motion of the particles while kinetic models include the motion of each individual particle. Kinetic effects are especially important when size scales are on the order of the ion gyroradius.

Specifically, the grid must be fine enough to resolve ion kinetic effects, yet coarse enough to span the large ionospheric volume.

Previous simulation studies have either neglected kinetic effects, or are limited, in the case of electromagnetic codes, by the electrostatic interaction. Electromagnetic codes provide the most complete description of a plasma but unfortunately the time stepping is severely constrained by the electron plasma period and the Courant condition² is set with respect to the velocity of light. Such a code would require too many grid points and too many time steps to be feasible with current state-of-the-art computers.

A hybrid code, of the type posed by *Harned* [1982], provides a reasonable solution at the expense of neglecting electron inertia. The release ions are treated as fully kinetic particles, the electrons as a massless fluid, and the ambient plasma as an magnetohydrodynamic (MHD) fluid. The code assumes quasi-neutrality eliminating the aforementioned problems of the electrostatic interaction. It is non-radiative thereby removing the constraint on the Courant condition with respect to the speed of light. In particular, the electric fields are solved for algebraically from the electron momentum equation rather than from the computationally intensive Poisson's equation. Ampere's law provides the electron bulk flow velocity and Faraday's law provides the magnetic field update. Further details regarding the hybrid code can be found in chapter 3.

Using a three-dimensional hybrid code, a direct comparison between the optical observations and the simulation results can be made. A projection of the ion densities onto the plane of observations provides a synthetic image from which morphological comparisons can be made. The code also serves as a diagnostics platform for investigating the effects of electron heating on the ion cloud morphology. This is a valuable numerical experiment for investigating effects that might be attributed to CIV.

1.6 Thesis Content and Organization

This thesis contains an observational analysis of the CRRES G1, G9, and G11A releases, a complementary simulation study using a three-dimensional hybrid code, and a recon-

²The Courant condition ensures numerical stability by requiring that the maximum physical velocity be less than the lattice speed $\Delta x/\Delta t$ where Δx is the minimum grid size and Δt is the simulation time step.

ciliation of the observations with the simulation results. The observational analysis has been published [Delamere et al., 1996] and is contained in chapters 2 and 3. Preliminary information and setup of the hybrid code are discussed in chapter 4. Chapter 5 contains simulation results while chapter 6 is reserved for discussions of the simulation results and the comparison of those results with observations.

Chapter 2

Observations

This chapter details the analysis of the CRRES G1, G9 and G11A barium release optical data. First we present the optical data which reveals skidding, structuring of the ion cloud, and an expanding disk of particles that is centered 20 to 30 km downstream from the release point. We then follow with an analysis of the ion distribution along the satellite path and a discussion of our quantitative image analysis technique.

2.1 CRRES chemical releases

The Combined Release and Radiation Effects Satellite (CRRES), jointly sponsored by the National Aeronautics and Space Administration (NASA) and the Department of Defense (DOD), was launched on July 25, 1990, on the first commercial Atlas I rocket [Johnson and Kierein, 1992]. The purpose of the mission was threefold: to conduct a series of chemical release experiments in the ionosphere and magnetosphere, to study the effect of the earth's natural radiation environment on state-of-the-art microelectronic components, and to measure naturally occurring ionospheric irregularities using LASSII (Low Altitude Satellite Studies of Ionospheric Irregularities) instruments. Although these projects were somewhat unrelated it should be noted that the LASSII instruments were particularly beneficial to the chemical releases mission by providing in situ measurements of various ionospheric parameters such as electron densities.

The CRRES orbit was 350 x 33,584 km with an inclination of 18.1 ° providing a wide

range of altitudes for conducting a variety ionospheric and magnetospheric chemical release experiments labeled G1 through G14. The CRRES payload consisted of 16 large canisters and 8 small canisters that were ejected from the satellite either singly or in pairs. The releases occurred in three phases. The first phase consisted of low-altitude releases (near perigee) over the South Pacific in September of 1990. This included the G13 and G14 CIV releases. The second phase were high-altitude releases (from 6000 to about 33,500 km) over North America in January and February of 1991. Finally the third phase were low-altitude releases over the Caribbean in July and August of 1991 among which were the G1, G9 and G11A releases.

The CRRES G1, G9, and G11A barium releases were all made under similar conditions. At the time of release the satellite was in full sunlight and moving nearly perpendicular to the geomagnetic field with an orbital velocity of 9.6 km/s. Release altitudes ranged between 400 and 500 km. The neutral barium cloud expanded as a spherical shell (equation 1.3) at 1.3 km/s [Wescott et al., 1994] and photoionized with a time constant of 23s Hallinan [1988]; Hoch and Hallinan [1993]. Table 2.1 summaries the release parameters of these three releases. One important difference to note is that G9 was made using two large canisters that were separated by 6 km while G1 and G11A were made using single small canisters.

Optical observations were made from a number of ground-based stations and from two instrumented Air Force KC-135 aircraft operated by the 4950th Test Wing at Wright Patterson Air Force Base, Ohio. This analysis uses the video data taken from the aircraft, numbered 127 and 131, by members of a team of scientists from the University of Alaska Fairbanks, Geophysical Institute. Figure 2.1 shows the location of the aircraft with respect to the releases. Aircraft 127 was flying southwest of the releases looking nearly perpendicular to the geomagnetic field, while aircraft 131 was flying to the northwest looking mostly up and along the field. The data were taken using intensified CCD (ICCD) TV cameras mounted on gyrostabilized platforms. The field of view was $11^\circ \times 14^\circ$. For these three releases the cameras were initially run unfiltered at TV frame rates (30 frames per second) for the purpose of quickly and accurately locating the release cloud. Later, 455.4 nm (the dominant barium emission line) filters were applied and the video signal integrated, but those images are well beyond the times of interest here. Because of the rapid separation of the ion and neutral clouds, the ion cloud could be unambiguously identified

	G1	G9	G11A
Date	(July 13, 1991)	(July 19, 1991)	(July 22, 1991)
Time, UT	0835:25	0837:07	0838:24
Latitude, ° N	17.8	17.4	16.8
Longitude, ° E	-62.9	-62.6	-60.3
Altitude, km	495	441	411
Solar screening height, km	247.8	192.1	217.1
Angle, v-sun	31.87	34.06	34.68
Angle, B-sun	66.89	67.80	70.93
Angle, B - v	94.78	98.35	102.41
v, km/s (total satellite velocity)	9.53	9.58	9.61
v , km/s	0.79	1.39	2.07
v _⊥ , km/s	9.50	9.48	9.39
Amount of Ba released, g	1468	10,405	1471
Moles at 40% efficiency	4.3	30.3	4.3
Atoms at 40% efficiency	2.6×10^{24}	1.8×10^{25}	2.6×10^{24}
B, nT	31,089	31,637	31,310
Gyrofrequency, Hz	3.5	3.5	3.5
Gyroradius, m	443.0	433.0	431.6
Ambient electron density, m ⁻³	9.0×10^{11}	5.0×10^{11}	1.5×10^{12}
<i>Aircraft 127 position</i>			
Latitude, ° N	12.5	12.9	13.0
Longitude, ° E	-67.3	67.5	-67.4
Altitude, km	11.0	11.0	11.0
<i>Aircraft 127 look angles</i>			
Azimuth	38.5	44.7	62.2
Elevation	28.5	27.1	18.3
Slant range, km	916.2	852.1	1039.9
<i>Angles between directional vectors, Aircraft 127</i>			
Look-sun	54.24	50.51	41.74
Look-v	64.33	58.56	45.15
Look-B	93.15	94.94	99.22
<i>Aircraft 131 position</i>			
Latitude, ° N	...	21.0	20.9
Longitude, ° E	...	-67.0	-67.0
Altitude, km	...	11.0	11.0
<i>Aircraft 131 look angles</i>			
Azimuth	...	131.4	121.2
Elevation	...	32.2	20.9
Slant range, km	...	750.7	955.0
<i>Angles between directional vectors, Aircraft 131</i>			
Look-sun	...	84.32	72.18
Look-v	...	54.40	40.76
Look-B	...	152.08	142.79

Table 2.1: CRRES (low altitude) Sunlit Release Experiment Parameters. Aircraft 131 did not fly for the G1 release.

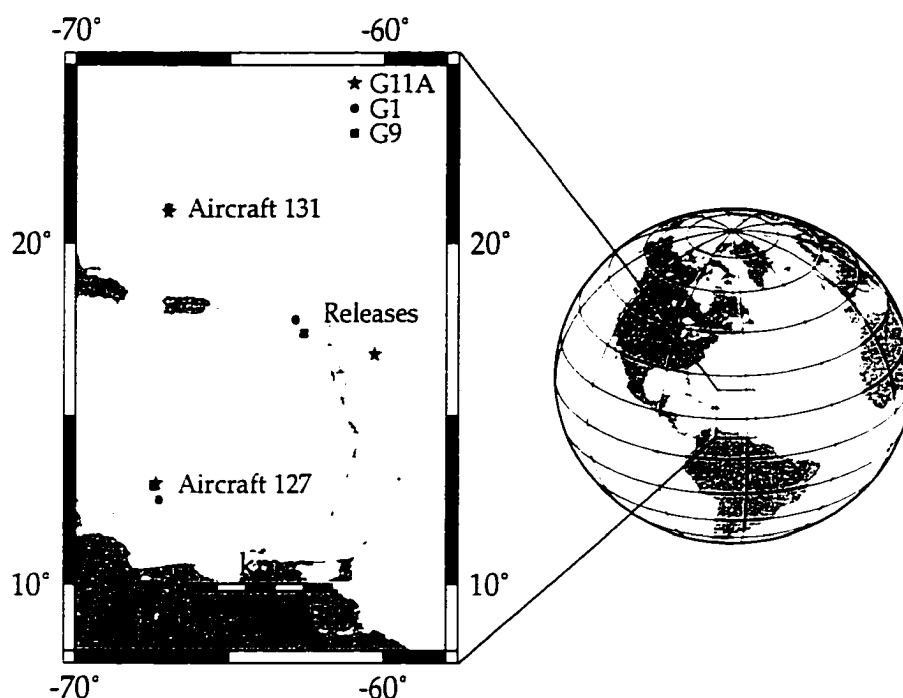


Figure 2.1: The location of the CRRES G1, G9 and G11A releases.

in the unfiltered images. Other groups did observe the release with filtered cameras from ground-based locations.

2.2 Optical Data

Samples of the optical data from the three releases are shown in figures 2.2, 2.4, and 2.6. The original data from the ICCD cameras were recorded on 3/4" U-matic and VHS video tape. Individual frames were digitally captured as 512×486 byte arrays in a *Targa* format. These images represent the raw and unprocessed data. However, for the purpose of illustration, subarrays of the complete image were extracted so the field of view does not necessarily reflect that of the camera system.

2.2.1 G1

Figure 2.2 shows 8 frames of the G1 release from 3 to 14 seconds after release from Aircraft 127. The look direction is approximately the same with respect to the bottom left corner in all 8 frames. Note that the cameras were tracking the neutral cloud so the ion cloud began to leave the field of view at 14 seconds. The release point in the images is next to the star, indicated by the arrow, in the 3 second frame. The geomagnetic field line through the release point is indicated in the 7 second frame and the satellite velocity vector is indicated in the 3 second frame. The ion and neutral clouds are labeled in the 12 second frame¹. Note that the bright neutral cloud saturated the CCD detector during this time causing light to bleed vertically. This accounts for the column of light above and below the neutral cloud and for the "tongue" of light below the circular neutral cloud. Finally, the distance scale only applies along the satellite velocity vector.

The images show several interesting features. With respect to the release point, we note that the edge of the ion cloud is roughly 10 km down the satellite path as clearly seen in the 7 second frame. However, luminosity is also seen expanding backwards along the satellite path. At 3 and 4 seconds this luminosity appears as two "prongs" and by 5 seconds a substantial amount of material is actually visible behind the release point. The ion cloud shows a "herringbone" structure² (8 s) within roughly 40 km of the release point as well as elongation along the geomagnetic field. Associated with this elongation is a faint striation along the release edge of the ion cloud. Figure 2.3 illustrates these observed features.

2.2.2 G9

Unlike the G1 release, both Aircraft 127 and 131 were flying for the G9 release. Figure 2.4 shows 4 unprocessed images from each aircraft at 5, 7, 9 and 11 seconds. The geomagnetic field and satellite velocity are indicated in the 7 second frame by the directional vectors \mathbf{B} and \mathbf{v} respectively. The vector origin is placed at the release point and the distance scales are given along the satellite path.

¹Ions and neutrals are easily differentiated in color images. The dominant barium ion emission line is blue while the dominant barium neutral emission line is green. Color observations of the CRRES releases confirm the separation of the ions and neutrals as indicated in figure 2.2

²The herringbone is not an artifact of the discrete digitization levels.

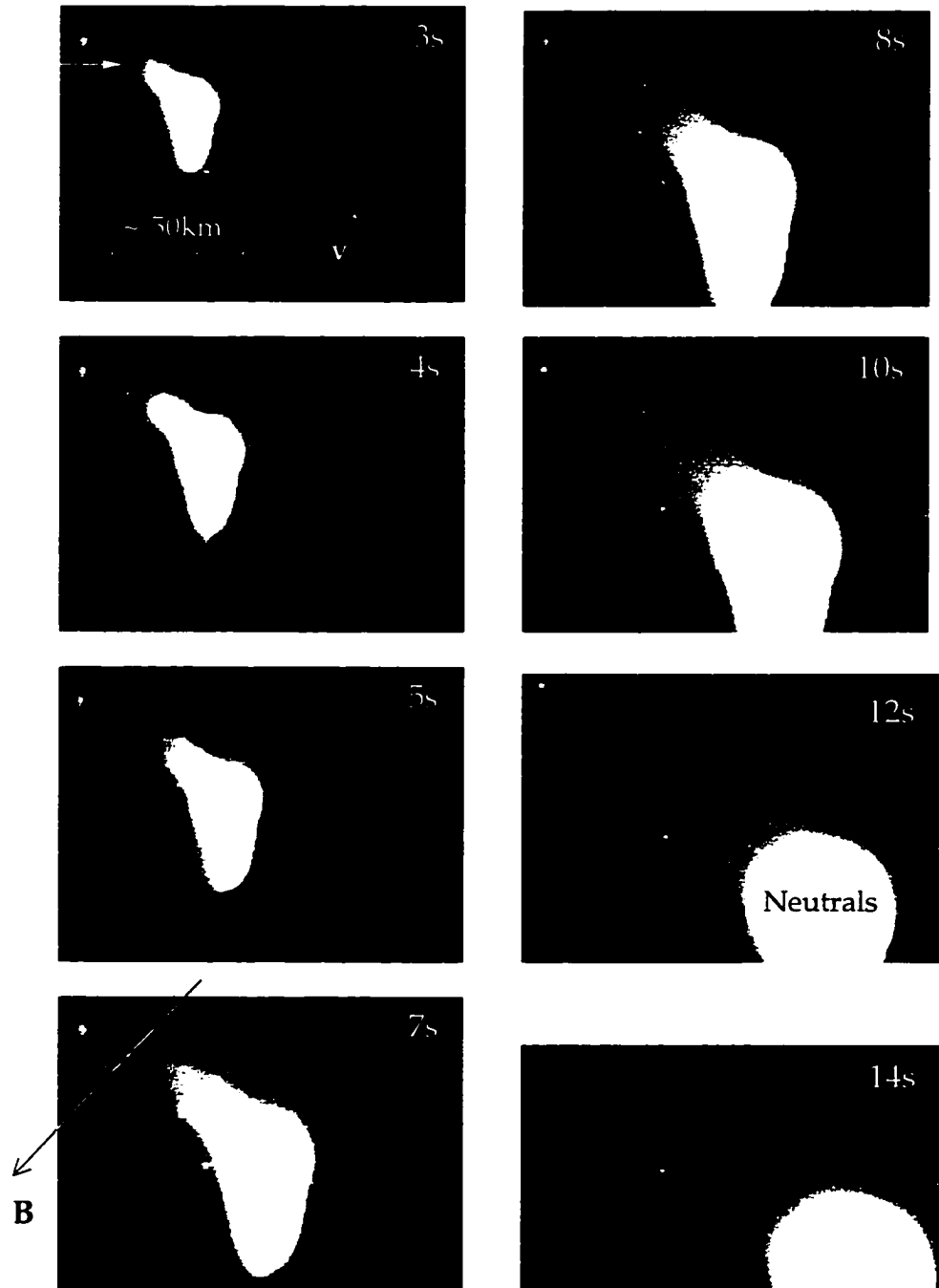


Figure 2.2: G1 observations from Aircraft 127. The release point is indicated with an arrow in the $t = 3s$. The satellite velocity is into the page, down and to the right. The geomagnetic field is into the page, down and to the left.

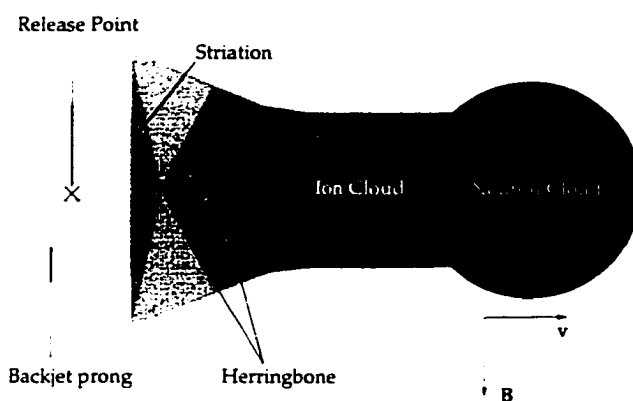


Figure 2.3: G1 cloud morphology. An illustration of the morphological structures observed in the G1 release.

As was the case with G1, a striation is visible along the release edge of the ion cloud. However, due to the brightness of this large release, ion cloud structures are masked by the saturated detector during this time. In addition, this was a double canister release, so the superposition of the two ion clouds may obscure the herringbone structures in the G1 release. Of particular interest, though, is a similar "backjet" of material as seen from Aircraft 127. By comparing with images from Aircraft 131, we see that this backjet is actually a disk of material that is expanding perpendicular to the geomagnetic field at satellite velocity with respect to the release point. The disk is not an artifact of vignetting and was definitively shown by triangulation to coincide with the backjet seen from Aircraft 127. It is important to note that the center of the disk is not at the release point but some 20-40 km downstream. The geometry is illustrated in figure 2.5.

2.2.3 G11A

Finally, samples of the data from the G11A release at 4, 6, 8, and 12 seconds are shown in figure 2.6. This data set confirms the expanding disk seen in the G9 releases, however, the detector was overdriven to 10 seconds, masking ion cloud structures. Nevertheless, the ion cloud from Aircraft 127 appears elongated or striated along the release edge of the cloud in the 8 second frame. By 12.2 seconds the ion cloud nearest to the release point is clearly elongated, and a herringbone structure could be present as well. A definitive identification of ion cloud structures and the "pronged" backjet found in the G1 release are affected by

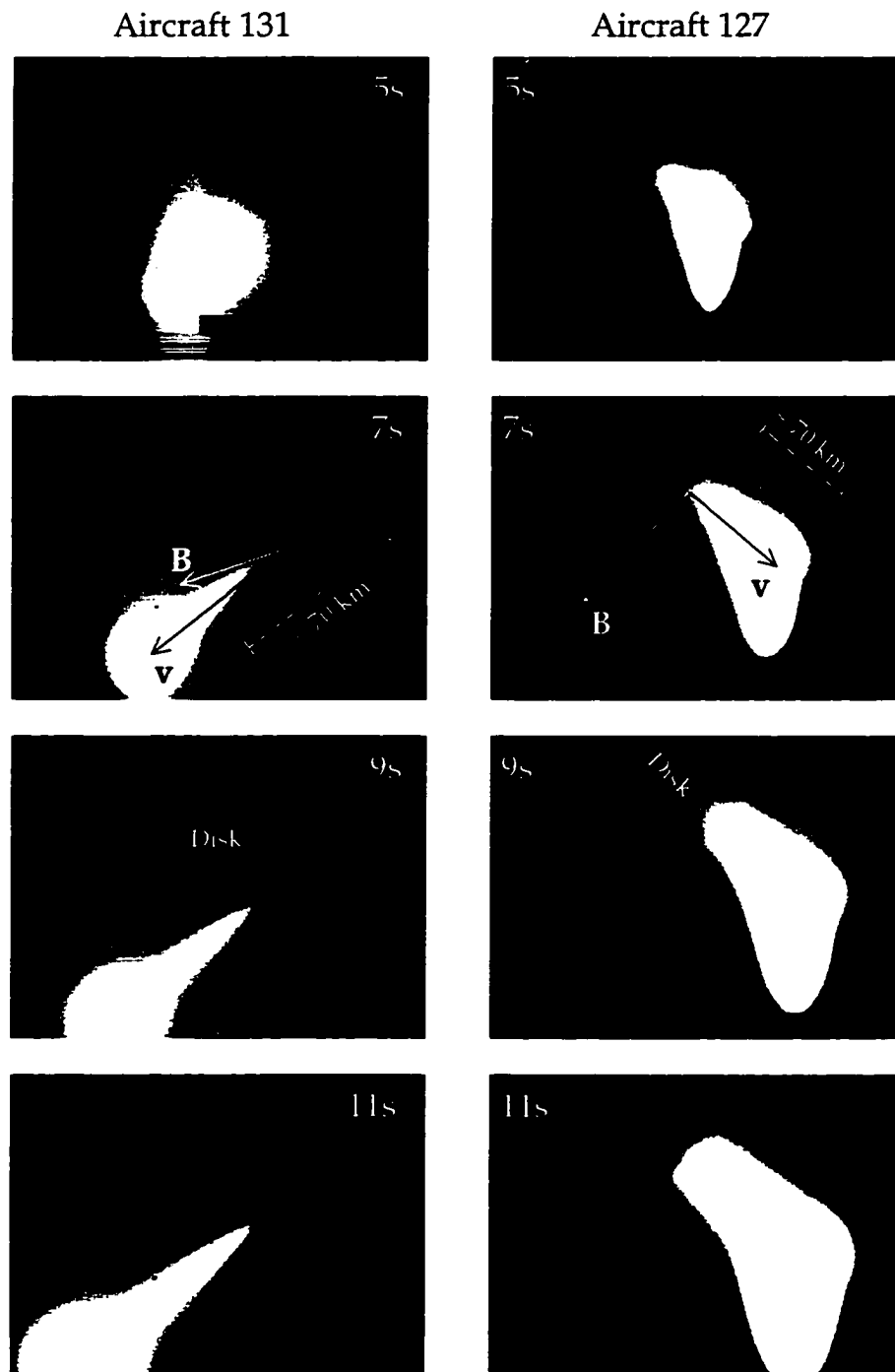


Figure 2.4: G9 observations from Aircraft 131 and Aircraft 127. The release point is at the origin of the directional vectors indicated in the 7s frames.



Figure 2.5: Expanding disk of particles. An illustration of the expanding disk of particles observed in the G9 release.

the image quality and the viewing geometry of the release. These images appear blurred compared to the G1 images and the angle between the look vector and the satellite velocity vector is only 45.2° compared to 64.3° for G1. The ideal angle for viewing these structures would be 90° .

2.3 Image Analysis

A simple visual inspection of the video data reveals many of the qualitative morphological features of the ion cloud, however it is also possible to quantify the analysis by performing a particle inventory. Such an inventory provides information regarding the spatial distribution of particles which is crucial to this analysis.

2.3.1 Vignetting corrections

The video signal from the chemical releases and stars was well above the background noise of the detector so there was no need to integrate a sequence of video frames to enhance the signal. The only correction made to the data were for vignetting effects. Vignetting is a radial decrease in signal from the center of the detector toward the edges. This is due to the diminished light gathering capabilities of the optics off of the optical axis. Figure 2.7 illustrates the vignetting effect and the correction made to "flat-field" the images. The first image is the raw data of a star field. The image was smoothed and a second order

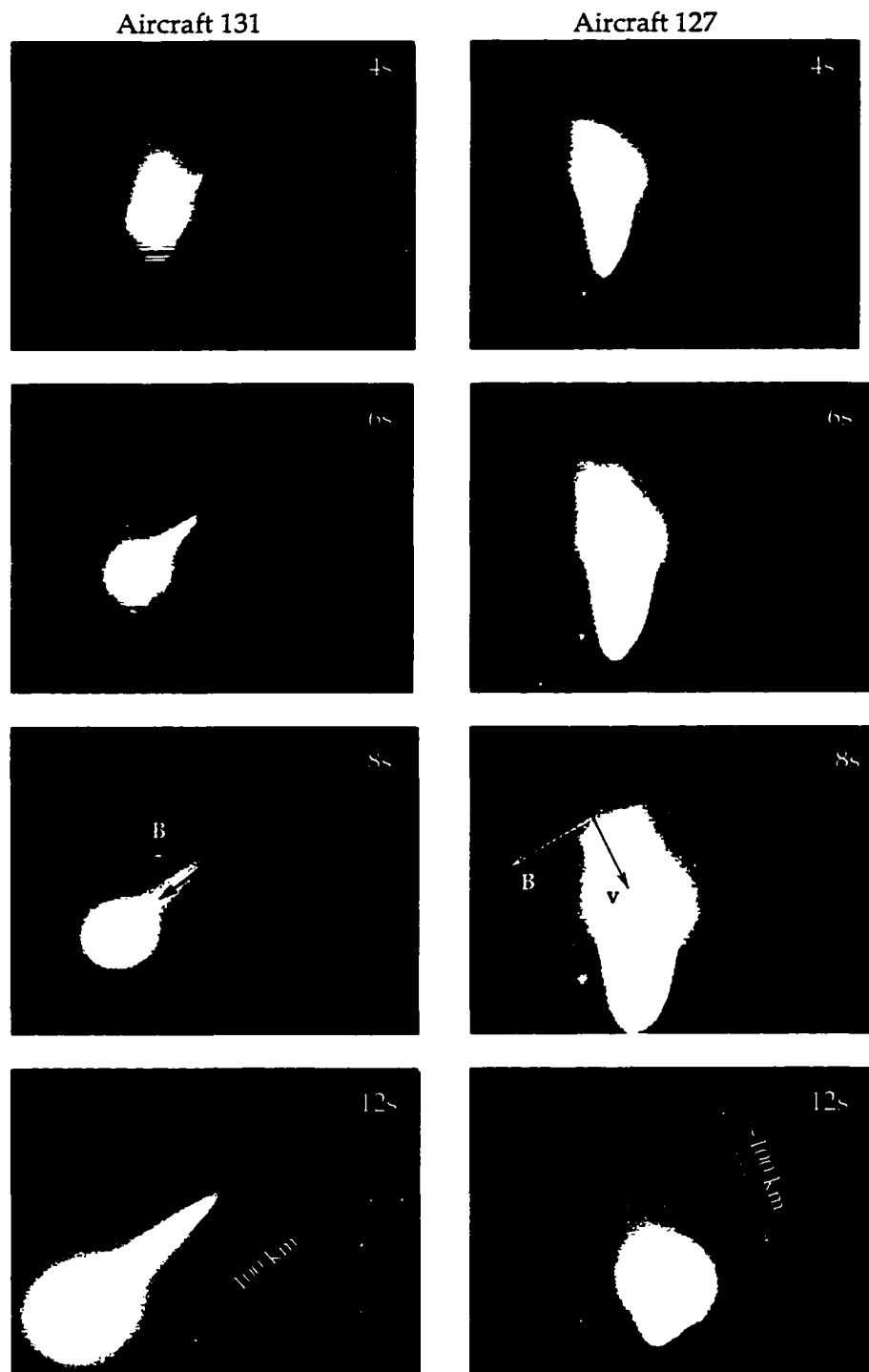


Figure 2.6: G11A observations from Aircraft 131 and Aircraft 127.

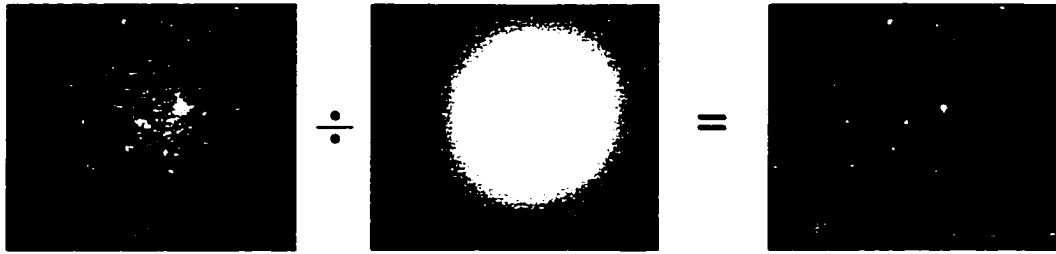


Figure 2.7: Image flat-fielding. The technique for removing vignetting effects. The original image is divided by a normalized vignetting profile giving a flat-field image.

polynomial surface, shown as the second image, was fitted to it. The edges of this surface were normalized to unity so that dividing the original data by the vignetting surface yields a flat-fielded image. Typically the center of the images were a factor of 3 brighter than the edges. The vignetting surfaces were unique to a given camera so we calculated a vignetting surface for each camera and each release.

2.3.2 Image Calibration

The calibration technique uses stars found in the flat-fielded images as absolute references. Given the photon flux from the star folded together with the camera (ICCD) response function, we can correlate the number of counts registered by the CCD detector with a given flux. The Smithsonian Astronomical Observatory catalog provides information regarding star location, spectral type, and visual magnitude, allowing for a positive identification of each star in the image. A library of stellar spectra³ of 161 stars spanning a range of different spectral types was made by *Jacoby et al.* [1984]. Using these representative spectra folded with the ICCD response function, we compared our image stars with those from the *Jacoby* library of the same spectral type. The flux from our stars is related to the flux of the *Jacoby* stars by

$$\frac{f_1}{f_2} = 2.531^{-(m_1 - m_2)} \quad (2.1)$$

where m is the visual magnitude and f is the photon flux measured at the surface of the earth and where subscripts 1 and 2 refer to the image star and the related *Jacoby* star respectively. After performing a background subtraction, the detector counts attributed to

³These spectra were published de-reddened to eliminate extinction due to interstellar gases and dust. We used their algorithm to redden the spectra for comparison with Earth-based observations.

the star are then related to the photon flux assuming a linear proportionality. Typical calibration curves are shown in figure 2.8.

Each image was calibrated independently to account for time varying atmospheric absorption effects and the numerous adjustments made to the detector sensitivity following the release. Calibration uncertainties vary depending on the number of stars available in the image, and on the background signal in the detector. The number of stars within the field of view and the range of visual magnitudes represented by the ensemble is really a matter of chance. Often stars lie behind the release cloud itself which makes the detector counts attributed to the star very sensitive to background subtraction. In general, the G1 and G9 images contained a very small background signal and we feel these calibrations are reliable with uncertainties based on linear regression of 7% and 5% respectively. The G11A calibrations, on the other hand, were hampered by a large background signal and by stars representing a narrow range of visual magnitudes. Thus, the G11A calibrations were somewhat less reliable with an uncertainty of 15%.

2.3.3 Ion Inventories

Given a reasonable image calibration an ion inventory can be performed. Barium emissions occur at several different wavelengths within the range of detector sensitivity. Table 2.2 summarizes the dominant emission lines, λ_i , the associated normalized detector response, $T(\lambda_i)$, and the emission rates, ϵ_i , calculated by *Stenbaek-Nielsen* [1989] with a Doppler correction appropriate to the observing conditions for these experiments. We are assuming that the photon flux and detector counts are linearly related over the full range of detector sensitivity, so the total number of counts expected from the contribution of all emission lines is

$$C = \frac{1}{\alpha} \sum_i T(\lambda_i) \phi_i \quad (2.2)$$

where the summation is over all emission lines, C is detector counts, ϕ_i is the flux, and α is the constant of proportionality determined from the star calibration. For an optically thin cloud of ions emitting at a distance r from the detector, the flux is

$$\phi_i = \frac{N\epsilon_i}{4\pi r^2} \quad (2.3)$$

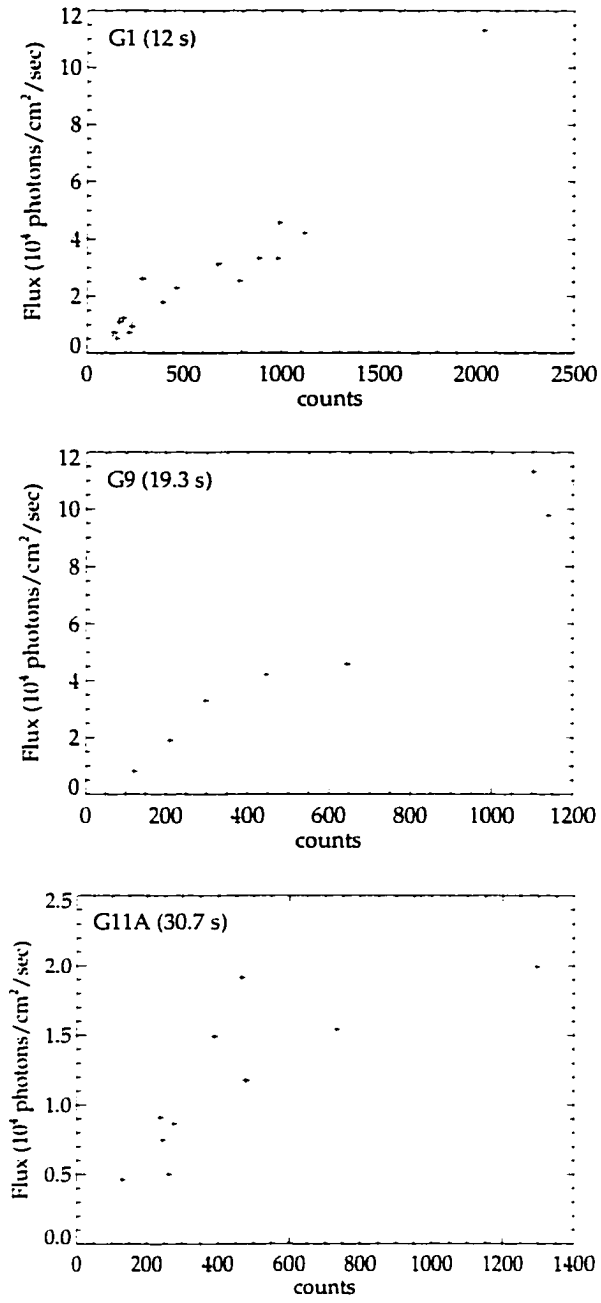


Figure 2.8: Image calibration. Image calibration examples, photon flux ϕ vs. detector counts C . We have assumed a linear relation of the form $\phi = \alpha C$. For the examples shown for G1, G9, and G11A, $\alpha = 45.9 \pm 3.1, 90.7 \pm 5.1,$ and 25.7 ± 3.8 respectively.

λ (nm)	ϵ (photons/sec/ion)	T	ϵT
455.4	1.90	0.59	1.12
493.4	1.01	0.95	0.96
585.4	0.51	0.47	0.24
614.2	0.31	0.28	0.09
649.7	0.09	0.67	0.06
$\Sigma =$			2.47

Table 2.2: Emission rates for a barium cloud in full sunlight. The total emission rate is the sum of contributions from 5 dominant emission lines folded together with the ICCD response (T).

where N is the number of emitting ions. Thus, the total number of ions is given by

$$N = \frac{4\pi r^2 \alpha C}{\sum_i T(\lambda_i) \epsilon_i} \quad (2.4)$$

The value for C is determined by integrating the region of the image containing the ions of interest and subtracting out the background detector noise and contributions from stars. We found that the average of several image values sampled from regions near the ion cloud provided a reasonable background value.

2.3.4 Ion cloud profiles

Using our star calibration technique, we quantified the ion distribution along the satellite path which we shall henceforth refer to as the x direction. Figures 2.9, 2.10, and 2.11 illustrate the image analysis. The images shown represent the samples from the Aircraft 127 data archive where the entire ion cloud is within the field-of-view at the latest possible time, and where the detector is not saturated. These criteria were satisfied at 12.0 s for the G1 release, 19.3 s for G9, and 30.7 s for G11A.

The images were first rotated to vertically align the geomagnetic field as indicated. The intensity scan (solid stepped line) shown below each image was generated by integrating the signal in each column (bin) of the image. Using equation 2.4 thus gives the number of ions in each field-aligned bin. The x axis distance scale applies to the satellite path where $x = 0$ is the release point. Note that the images have been scaled to roughly match the x axis scale. The background stars that appear in the images were mostly removed from

the intensity scan using a median filter which replaces the value of each pixel with the median value of several neighboring points. The presence of the neutral cloud to the right in each image is suggested by the shading. In the case of G1, contributions to the profile include both neutral emissions and detector overdrive which is present in the top right corner of G1 image. The dotted line represents a theoretical profile which assumes that all ions produced are magnetized and therefore remain at the location where they were formed. The implications of the difference between the observed and theoretical profiles relate to the key issue in this thesis and will be discussed in the next chapter.

The release point is indicated (\times) in each image. Note that the edge of the ion cloud is located several km from the release point in each release. These distances for G1, G9, and G11A are 9.6, 17.5, and 7.5 ± 1.0 km respectively. We also note that the ion distribution peaks at nearly 60 km from the release point in the G11A release. Beyond this peak the signal is contaminated by neutral emissions from the nearly stationary neutral cloud (the neutral cloud began slowing after 20 s). The dashed line therefore illustrates a possible continuation of the ion cloud profile since we cannot differentiate between ions and neutrals beyond 80-90 km with unfiltered detectors. Keep in mind that the neutral emission rates are roughly an order of magnitude greater than the ion emission rates, so the signal can be greatly enhanced on the flanks of the neutral cloud. In the case of G1 and G9 we infer that the ion profile peaks just beyond 60 km and 100 km respectively.

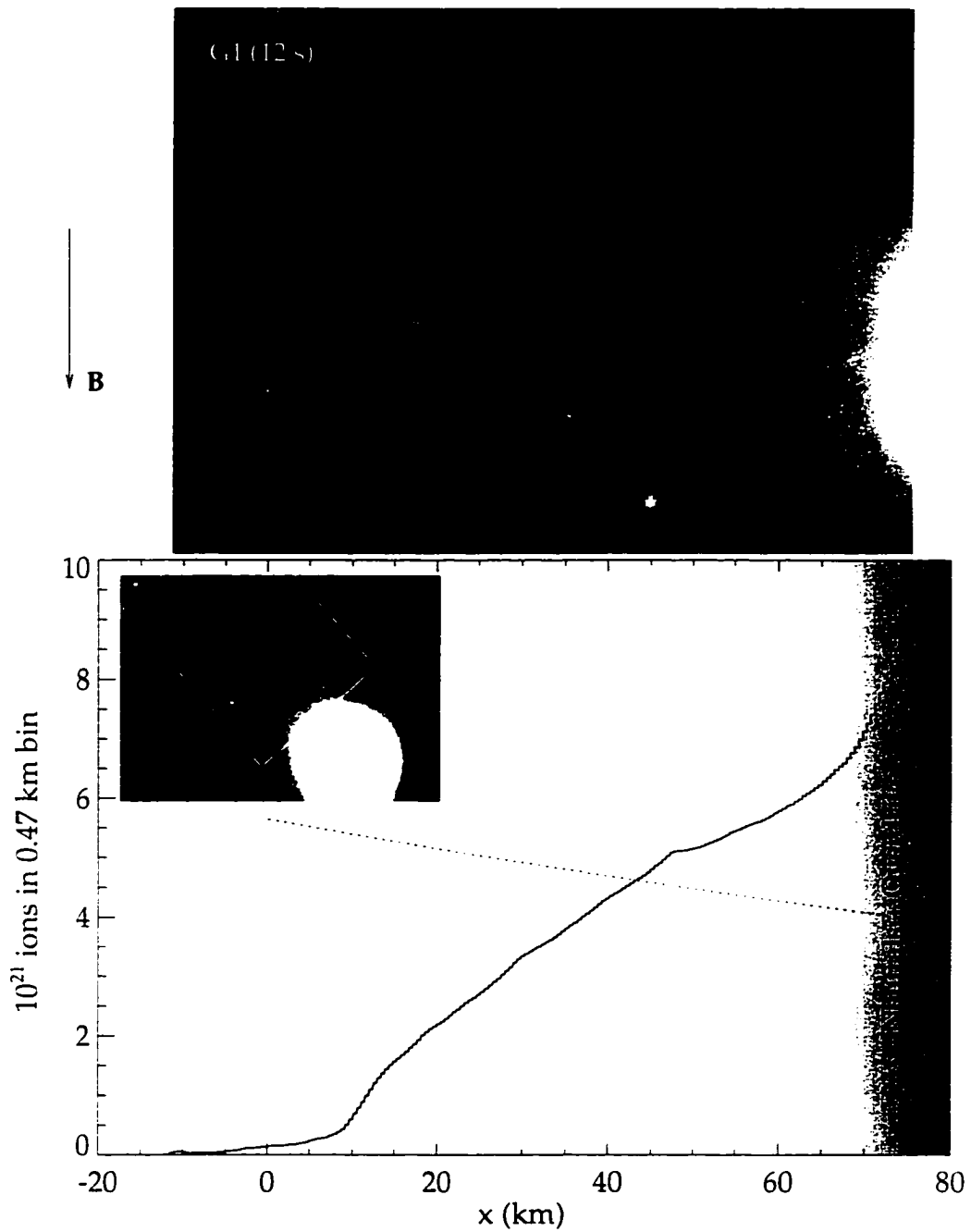


Figure 2.9: G1 ion cloud profile from Aircraft 127 at $t = 12.0$ s. The image was rotated so that the geomagnetic field is vertically aligned and the release point is indicated (\times). The calibrated ion profile (solid stepped line) is the integrated intensity along the magnetic field in a bin of one pixel in width. The dotted line is the expected profile for 100% magnetized ions, and the shaded region represents contamination to the signal from neutral emissions and instrumental effects.

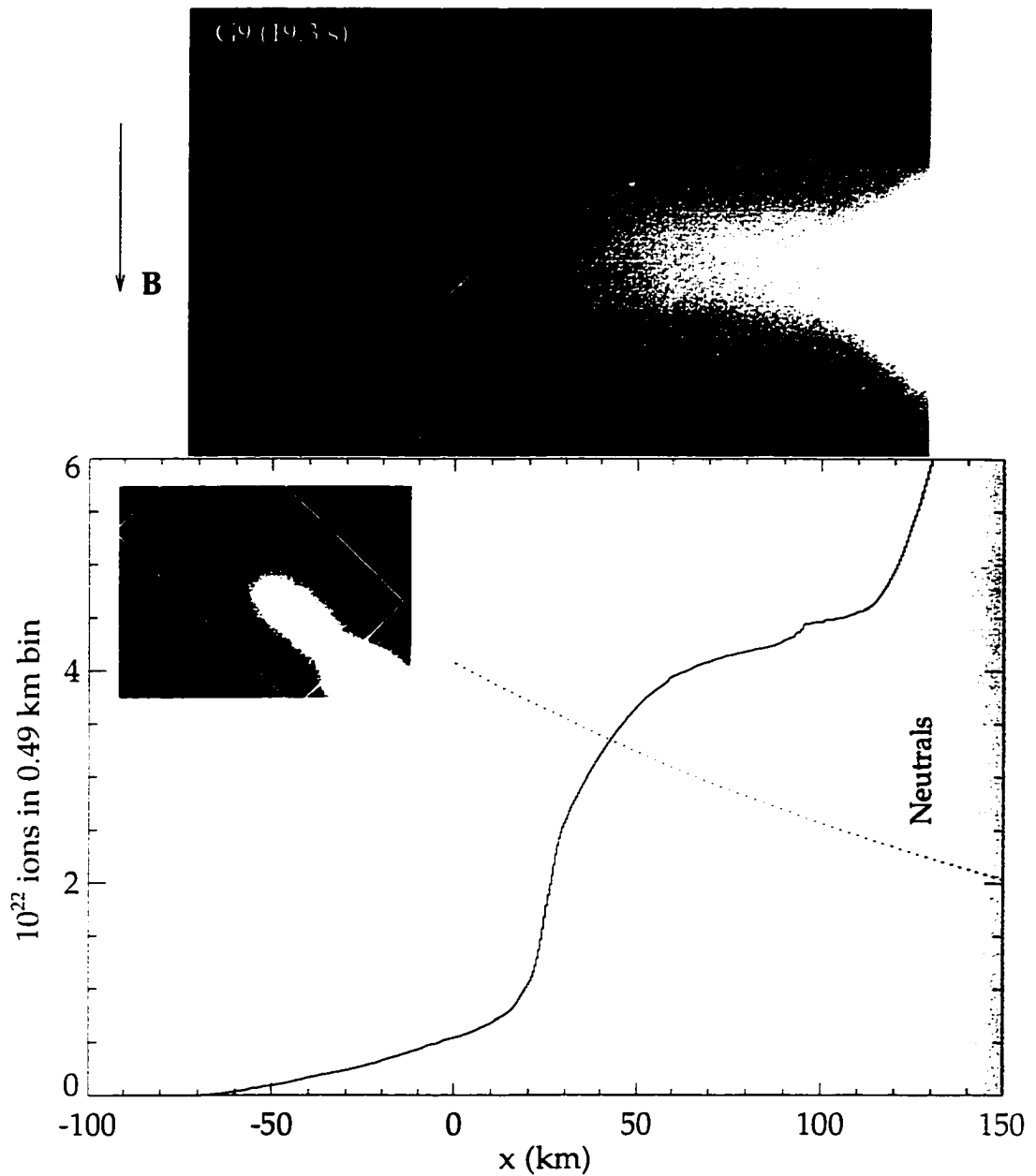


Figure 2.10: G9 ion cloud profile from Aircraft 127 at $t = 19.3$ s. The image was rotated so that the geomagnetic field is vertically aligned and the release point is indicated (\times). The calibrated ion profile (solid stepped line) is the integrated intensity along the magnetic field in a bin of one pixel in width. The dotted line is the expected profile for 100% magnetized ions, and the shaded region represents contamination to the signal from neutral emissions.

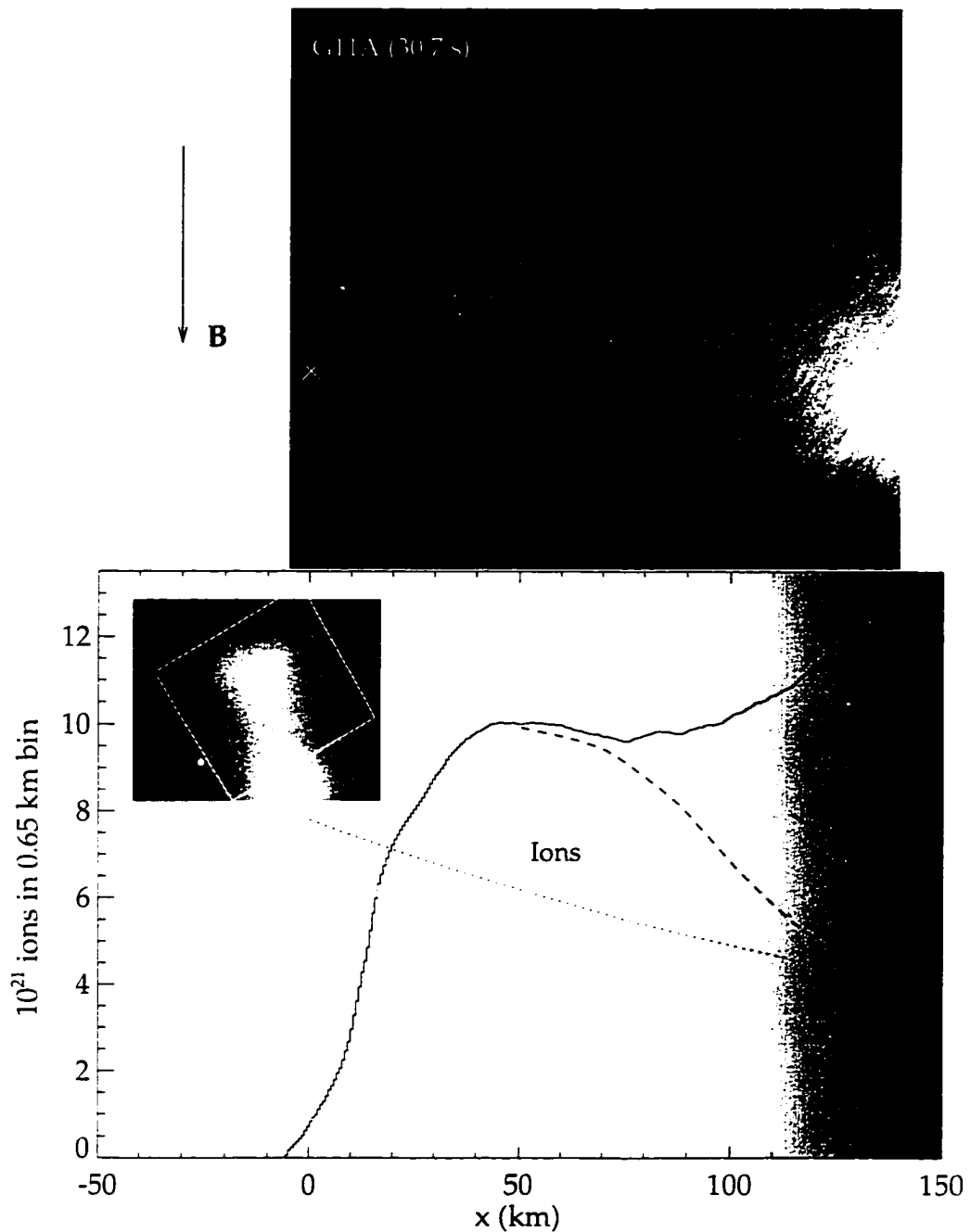


Figure 2.11: G11A ion cloud profile from Aircraft 127 at $t = 30.7$ s. The image was rotated so that the geomagnetic field is vertically aligned and the release point is indicated (\times). The calibrated ion profile (solid stepped line) is the integrated intensity along the magnetic field in a bin of one pixel in width. The dotted line is the expected profile for 100% magnetized ions. The shaded region represents contamination to the signal from neutral emissions and the dashed line illustrates the possible continuation of the ion profile into the region containing neutral emissions.

2.4 Summary

The optical data show three notable features which this thesis attempts to explain. The first is the observation is that the edge of the ion cloud is displaced from the release point by 10 to 20 km and that the ion cloud profile is different from the expected profile for the case where all ions produced are magnetized. Secondly, we observed a striation along the release edge of the ion cloud and structures within the ion cloud itself. The G1 release in particular showed structures that resemble a herringbone. Finally, our third observable was a disk of particles expanding at the satellite velocity perpendicular to the geomagnetic field. This disk first appeared at 2-3 seconds after the release and continued to expand from within the ion cloud for 5-8 seconds after the release. A summary of the observations is given in Table 2.4.

	G1	G9	G11A
Release size	Small	Large	Small
Data Quality	Clear, sharp images. Ion cloud begins to leave field of view at 13 s.	Ion cloud overdriven to 18 s. Image clear and sharp otherwise.	Ion cloud overdriven to 10 s. Image appears blurred. Full view of ion cloud at 30 s.
Ion cloud morphology	Herringbone structure, faint striation along release edge of cloud.	Distinct striation along release edge of cloud.	Fuzzy image, not much structure visible.
Distance from release point to edge of ion cloud, ± 1.0 km.	9.6	17.5	7.5
Time duration of backjet, s	2-4	3-8	2-5
Total number of ions observed in the ion cloud (at time observed).	8×10^{23} (10.3 s)	9×10^{24} , (19.3 s)	1.4×10^{24} (30.7s)
Distance from release point to ion profile peak, (± 5 km)	> 60	> 100	60

Table 2.3: A summary of the observations made of the CRRES G1, G9, and G11A sunlit barium releases.

Chapter 3

Inferred Processes

Figure 3.1 shows various energy parameters for the G1, G9, and G11A releases: the total kinetic and thermal barium release energies, and the ambient magnetic and $\mathbf{v} \times \mathbf{B}$ electric field energies enclosed by the neutral release cloud according to equation 1.3. Initially, the dense ion population can form a high beta plasma. Diamagnetic cavities were observed in the higher-altitude releases [Singer, 1992], but in the releases considered here the magnetic field energy exceeds the kinetic and thermal energy at 1 s and with an ionization rate of 3% per second a diamagnetic cavity cannot be expected beyond 1 s. However, it is clear that the cloud has sufficient energy to propagate cross the field for a significant time, and therefore the analysis will focus on processes associated with the cross-field propagation.

This chapter addresses the role of polarization electric fields in cross field propagation of the ion cloud. It is this so-called "skidding" [Huba et al., 1992b] of the ions that is presumably responsible for the difference between the observed ion cloud profile and the magnetized profiles shown in Figures 2.9, 2.10, and 2.11. We will also show that the polarization electric fields are further related to the ion cloud morphology and the expanding disk composed of what turns out to be neutral barium particles.

3.1 General Model Considerations

In full solar UV light, barium neutrals have been observed to ionize with a time constants of 13 ± 2 s, 17 ± 2 s, 23 ± 2 s [Hallinan, 1988; Hoch and Hallinan, 1993]. Hoch and Hallinan

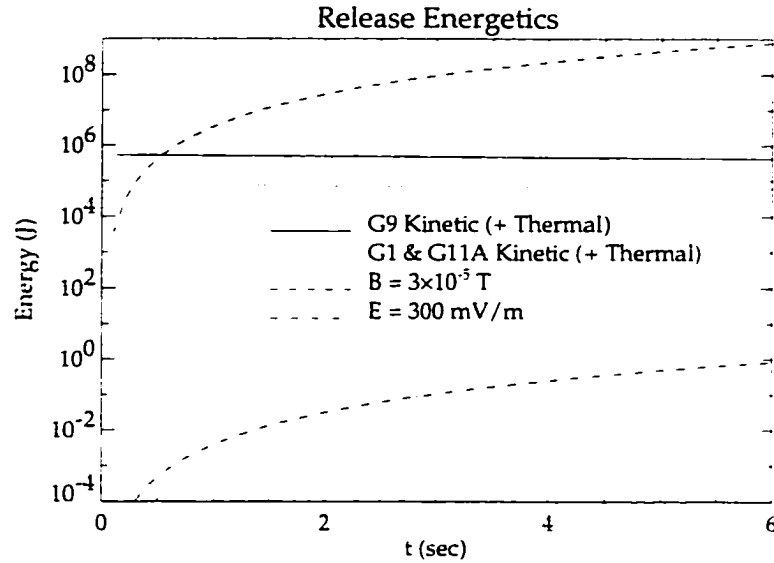


Figure 3.1: Energy parameters for the CRRES releases. The release energy represents the total kinetic energy of the released neutrals (thermal contributions are negligible). The magnetic and electric field energy represents the total ambient magnetic and $\mathbf{v} \times \mathbf{B}$ electric field energy enclosed by the expanding neutral cloud.

[1993] concluded that the variability is due to nonsolar processes since the ultraviolet solar flux does not vary by a factor of 2. *Drapatz* [1972] and *Carlsten* [1975] calculated a photoionization time constant of 28 ± 6 s which is consistent with the picture of nonsolar ionization processes contributing to the net ionization of a barium release cloud. Our analysis of the CRRES data is consistent with a time constant of roughly 23 s. It turns out that our model results are insensitive to the choice of ionization time constant, so we elected to use a value of 23 s for the remainder of the analysis.

The 23 s time constant is valid for an optically thin cloud in radiative equilibrium with the solar radiation. Photoionization requires photons with a wavelength shorter than 326.5 nm. With an ionizing solar photon flux of 4×10^{15} photons/cm²/s [*Banks and Kockarts, 1973*], the 23 s time constant would correspond to an ionization cross section of 10^{-17} cm². The neutral cloud can then be assumed optically thin to the ionizing solar light when the column density decreases below 10^{17} cm⁻². For the large G9 release with 2×10^{25} neutrals expanding isotropically at 1.3 km/s, this column density will be reached in a time of order 20 ms, which is less than the duration of the release process (<200 ms). We therefore can

reasonably assume that *the release is optically thin to solar UV at all times*.

The ionization results from the combination of a number of transitions involving metastable states and the 23 s time constant is for a neutral barium cloud in radiative equilibrium with the solar radiation. This cannot be expected to be the case at release. Model calculations by *Stenbaek-Nielsen* [1989] indicate that equilibrium is reached within 2 s for an initially cold cloud. A reexamination of the calculations has shown that the important metastable-stable states are rapidly populated indicating that significant ionization will start almost immediately after release. A more quantitative evaluation is difficult, but as it turns out our model results do not critically depend on this point, only that there will be significant ionization produced at an early time. Therefore we shall assume the 23 s time constant valid from release.

The release process takes less than 0.2 s (C. S. Stokes, private communication, 1994) corresponding to orbital distance of about 2 km. The skidding distance to the edge of the ion cloud is ~ 10 km or more, corresponding to one or more seconds along the orbit, considerably larger than the distance or time associated with the release process itself. Hence we will also assume that the release is instantaneous. The assumptions of a time-independent 23 s ionization time constant and an instantaneous release simplify modeling calculations considerably.

3.2 Skidding

The observed distribution of ions along the satellite path shown in figures 2.9, 2.10, and 2.11 demonstrates that a significant fraction of the early ion population has propagated across the geomagnetic field in the satellite direction (x direction). This so-called "skidding" [*Huba et al., 1992b*] effect is foremost responsible for the gap between the release point and the edge of the field-aligned ion cloud. This gap is not a geometrical effect due to the motion of the aircraft, nor is it due to general ionospheric convection, which for these releases was less than 100 m/s. As argued above (section 3.1), the release process can be considered instantaneous, and that significant ionization occurs immediately; therefore, this initial skidding distance cannot be attributed to a delay in the onset of ionization.

Beyond the initial skidding distance of ~ 10 or more km, our analysis shows that many

of the ions must continue skidding. The magnetized ion cloud profiles (dotted lines in figures 2.9, 2.10, and 2.11) represent the expected ion profiles for a neutral cloud ionizing with a 23 s time constant. The difference between these profiles, where the expected is greater than the observed, represents an ion population that must be redistributed downstream. *How far do these early ions skid?* Unfortunately, the data cannot answer this question due to limitations in the field of view of the camera combined with "contamination" from neutral emissions. The dashed line in figure 2.11 suggests a possible continuation of the ion profile into the neutral regime, but a definite profile is not possible. Further investigation of skidding processes will require a detailed investigation of the related physics.

Skidding occurs when the ion cloud polarizes and the resulting polarization electric field enables the ions to $\mathbf{E} \times \mathbf{B}$ drift with the neutral cloud. The polarization, essentially, is the formation of charge layers at the edges of the ion cloud due a charge separation between ions and electrons gyrating in different directions, *and the inability of the background plasma to neutralize the space charges*. In the case of ions produced from an expanding neutral barium cloud described by equation 1.3, the initial polarized ion population will maintain the shape of the neutral distribution and $\mathbf{E} \times \mathbf{B}$ drift with the neutral cloud. Subsequent ionization will be added to the skidding ion core which will increase in both radius and density. However, eventually the radius of the core perpendicular to the ambient magnetic field will be limited by the ambient plasma density and all ions produced beyond this radius will be magnetized forming a trail of ions behind the neutral cloud.

The skidding core will continue to move in the release direction but will erode as the outer polarization charge layers are peeled off. The charge required to maintain the $-\mathbf{v}_{sat} \times \mathbf{B} = 300 \text{ mV/m}$ electric field within a spherical core is very small compared to the total number of released particles suggesting that the core is capable of skidding well beyond the early times that are of interest here. Our observations indicate that the core disintegrated relatively fast as suggested by the distance to the peak ion density, and therefore other processes such as coupling to the ionospheric plasma must be included. Some aspects of the coupling have been considered by *Haerendel* [1982], *Brenning et al.* [1991b,a], and *Huba et al.* [1992b], and will be addressed by the hybrid code below. These studies show that the polarization electric fields will decay through current dissipation in the ambient ionosphere, but for the simple model calculations that follow in this chapter we

disregard the coupling effects.

3.2.1 Calculated initial skidding distance

We constructed a simple computer model based on the assumptions and discussion above to estimate the initial skidding distance of the ion cloud (i.e., the distance from the release point to the edge of the ion cloud). The model first estimates the density of ions contained within the neutral cloud as a function of time. The location of the polarization charge layers with respect to the neutral cloud center is then determined by the limiting case where the ion density equals the ambient density. Ions inside the charge layer are added to the polarized core, while ions outside are added to the magnetized ion trail.

From the neutral barium velocity distribution function (1.3), the neutral cloud density as a function of cloud radius, r , and time, t , in the satellite reference frame is given by

$$n_n(r, t) = \frac{N_o}{4\pi r^2 t \alpha} e^{-(r-v_o t)^2 / (v_{th} t)^2} \quad (3.1)$$

where N_o is the total number of released particles, v_o is the radial expansion velocity of the neutral cloud (1.33 km/s), v_{th} is the thermal expansion velocity of the Gaussian profile (0.29 km/s), and $\alpha = v_{th} \sqrt{\pi}$ is the normalization factor. The ion density within the neutral cloud can be obtained from (3.1) by replacing N_o with an expression for the total number of ions, ΔN_i , that are contained within the moving neutral cloud at a given time. To determine ΔN_i , consider first the ionization rate which is given by

$$\frac{dN_i}{dt} = N_o \frac{e^{-t/\tau}}{\tau} \quad (3.2)$$

where τ is the ionization time constant (23 s). For a magnetized ion, the time that the ion spends in the neutral cloud is on average half of the transit time of the neutral cloud, or

$$\Delta t = v_o t / v_{sat} \quad (3.3)$$

where v_{sat} is the satellite velocity (9.6 km/s). So the total number of ions within the neutral cloud created in Δt at time t is

$$\Delta N_i = \frac{N_o e^{-t/\tau} v_o t}{v_{sat} \tau} \quad (3.4)$$

and the ion density within the neutral cloud is

$$n_i(r, t) = \frac{N_0 e^{-t/\tau_{v_0}}}{4\pi r^2 \alpha \tau v_{sat}} e^{-(r-v_0 t)^2 / (v_{sat} t)^2} \quad (3.5)$$

For the model calculation, time is advanced according to 3.3, and the radius of the polarization charge layer from the neutral cloud center is set where n_i equals the ambient plasma density. Equation 3.5 is then numerically integrated at each time step to determine the total number of ions internal and external to the charge layer. Note that the internal ions move with the neutrals because of the polarization electric field and the external ions are magnetized. Therefore, ions internal to the charge layer are added to the core, while ions external to the charge layer are added to the ion trail. The core ions skid for the duration of the calculation without contributing to the ion trail. The free parameters in the model are then the total number of barium neutrals in the release and the ionospheric plasma density.

Numerical values for the three releases investigated are given in Table 2.1. A complexity arises, however, in the case of G9. While the G1 and G11A releases were each from one small canister, the G9 release was a simultaneous release from two large canisters. At the time of release the G9 canisters were about 6 km apart. Because of this separation the two release clouds would not interact before about 2.2 s after release, at which time the neutral clouds have moved about 22 km from the release point, which is farther than the 17.5 km skidding distance observed. For the model calculation we therefore used only half the number of neutrals given in Table 2.1 for the G9 experiment.

Figures 3.2 are the model results (re-sampled to a uniform grid) showing the number of ions left behind the skidding core as a function of distance from the release point. The results are presented for three ionospheric densities: the observed density, a higher and a lower density. The densities used are given in the figures in number/m³. Also shown is the trace that would have resulted if there had been no skidding, that is, all ions trapped in **B**.

The ion trail traces show that initially, when the neutral cloud is very dense, the resulting high ionization rate will create a polarized ion cloud containing essentially all ions produced. This accounts for the initial low number of ions in the trail. The neutral density will decrease as t^{-3} , while the size of the cloud only increases as t , resulting in a

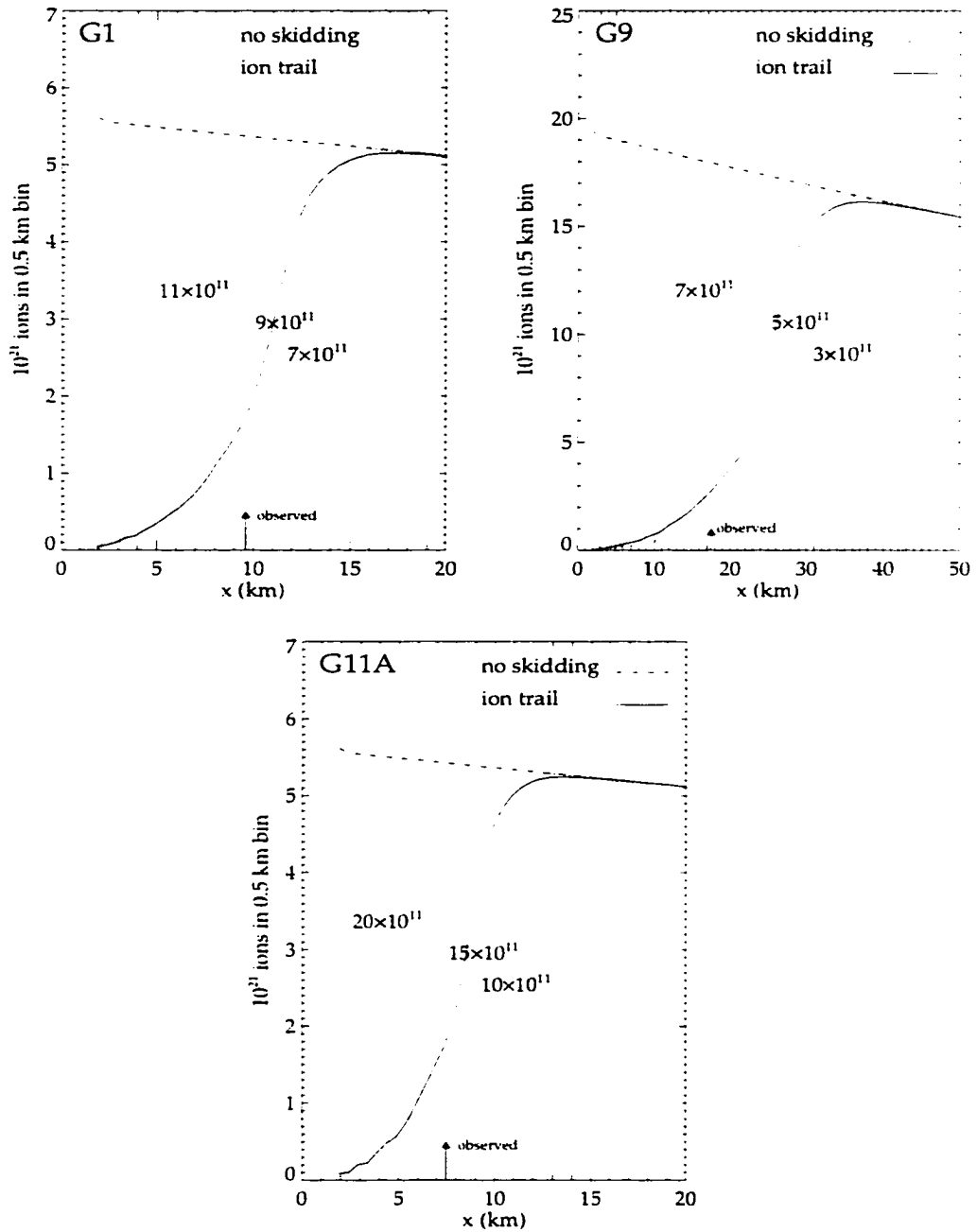


Figure 3.2: Skidding model results for G1, G9, and G11A. Ion trail profiles correspond to the ambient electron densities shown (number/m³). The solid lines correspond to the electron densities measured by LASSI, and the dotted lines illustrate the sensitivity of the results to a higher and a lower electron density. The observed skidding distances are indicated.

decrease in the ion density. As the ion density becomes comparable to the background, a rapidly increasing fraction of the ions produced will be magnetized as demonstrated by the sudden increase in the number of trail ions. Eventually all ions produced will add to the magnetized trail.

The model traces are very similar to the trace from an actual image shown in Figures 2.9, 2.10, and 2.11. The ions in the polarized core would be the difference between the no skidding curve and the ion trail curve. Although not addressed in the model, we would anticipate that ions eroding from the core would cause the ion trail curve (solid line) to raise above the no skidding curve and eventually fall back to the no skidding level as the core is dissipated, providing qualitative agreement with the observations illustrated in Figures 2.9, 2.10, and 2.11.

We also note that the initial skidding distances inferred from the model are in good agreement with the observations of 9.6, 7.5, and 17.5 km for G1, G11A, and G9 (Table 2.4) as indicated in Figure 3.2. The steep inner edge of the barium ion trail is very well reproduced, and the skidding distance appears to be sensitive to the ionospheric plasma density.

3.3 Expanding Neutral Disk

The expanding disk of material, seen as the "backjet" from Aircraft 127 and as a disk from Aircraft 131 (figure 2.4), is neutral barium. Our unfiltered optical data cannot confirm this conclusion, but the 10 km/s expansion velocity perpendicular to \mathbf{B} results in a disk that is much larger than the 430 m barium ion gyroradius. This conclusion is further supported by filtered data at 455.4 nm, the dominant Ba^+ emission line, taken by the Lockheed group (R. Rairden, personal communication, 1994) from aircraft 127. Here we observed that the disk did not appear as Ba^+ until roughly 15-20 s after release. This is consistent with neutral barium photoionizing with a time constant of 23 s. Thus we conclude that the expanding disk is neutral barium.

We made an estimate of the disk's neutral population by performing an inventory on the backjet. Assuming that the backjet represented a fraction of a circular disk, we extrapolated the inventory to a full disk. Because of the delayed onset of the backjet the

extrapolation was based on the assumption that the disk was centered 20-30 km (depending on the size of the release) downstream from the release point. Using a neutral emission rate that is an order of magnitude greater than the ion emission rate, we calculate that the G1, G9, and G11A disks contained a total of 8×10^{21} , 1×10^{23} , and 1.8×10^{22} neutrals atoms or 0.3%, 0.7%, and 0.7% of the released material respectively. The uncertainties associated with these neutral inventories stem from the image calibrations, the neutral emission rates, assumptions with regard to the extent of the disk, and background subtraction (especially in the case of G11A). These values should therefore be considered as an order of magnitude estimate.

The neutrals in the disk cannot come directly from the canister evacuation. They must be the result of some process acting after the release. One possible process that could be responsible for this disk is charge exchange between barium ions and neutrals. *Liou et al. [1996]* and *Hampton [1996]* have examined the process in connection with an evaluation of the CIV experiments and find a weakly velocity dependent charge exchange cross section of $1 \times 10^{-14} \text{ cm}^2$ which is roughly an order of magnitude larger than the barium-barium collision cross section. Since the releases were essentially perpendicular to \mathbf{B} , the magnetized ions are held by the magnetic field while the neutrals stream past. This situation clearly favors charge exchange, and because there is no momentum exchange and the ions have essentially no velocity parallel to \mathbf{B} , the charge exchange neutrals will form a disk perpendicular to \mathbf{B} .

3.3.1 Calculated Neutral Disk Inventory

A quantitative assessment of the efficiency of the Ba-Ba⁺ charge exchange process can be made using the model derived for the skidding calculations. Charge exchange will only involve the ions outside the skidding core. These ions are assumed frozen into the background magnetic field and thus will gyrate around \mathbf{B} with the release velocity while the neutrals stream past. Hence this counterstreaming between neutrals and ions will result in a high probability for charge exchange.

The skidding model provides the ion and neutral densities and the radius of the skid-

ding core as functions of time. In general, the net charge exchange rate is given by

$$p(t) = 4\pi \int f_i(r, v_i, t) f_n(r, v_n, t) |v_i - v_n| \sigma(|v_i - v_n|) r^2 dr d^3 v_i d^3 v_n \quad (3.6)$$

where $f_i(r, v, t)$ and $f_n(r, v, t)$ are the ion and neutral distribution functions, v_i and v_n are ion and neutral velocities, and $\sigma(|v_i - v_n|)$ is the charge exchange cross section. For a neutral particle moving past a magnetized ion the relative speed averaged over one gyroperiod is $v_r = 4v_{sat}/\pi$. We will assume therefore that the ion population is stationary and that the neutral population has velocity v_r . In this case, the distribution functions now take the form $n(r, t)\delta(v)$. Also, since the Ba-Ba⁺ charge exchange cross section is weakly velocity dependent, we will treat σ as a constant. With these simplifications, the charge exchange rate integrated over the nonskidding part of the cloud is

$$p(t) = 4\pi v_r \sigma \int_{r_p}^{\infty} n_i(r, t) n_n(r, t) r^2 dr \quad (3.7)$$

where r_p is the radius of the polarization charge layer. To estimate to the total number of charge exchanges, $p(t)$ can be multiplied by the interaction time of the ion and neutral populations. We assumed the average interaction time to be the transit time of the Gaussian distribution at full width, or $2v_{th}t/v_{sat}$.

Figure 3.3 shows the charge exchange rate as function of time for the releases. The peak production is seen to be at 1 s for the small releases and 2.5 s for the large. Also, the process is limited to the early phase of the release. This is in good agreement with the appearance of the neutral disk in the video. Again, the calculation for the G9 release, which consisted of two canisters 6 km apart, is for one canister only. However, in this case the clouds begin to interact during peak production, and thus the single canister model will lead to an underestimate. The amount of neutral barium produced in the model and the fraction of released barium vapor for the G1, G9, and G11A releases are 8.5×10^{21} (0.33%), 3.3×10^{22} (0.36%), and 1.2×10^{22} (0.47%). The corresponding observed amounts of neutrals in the disk for G1, G9, and G11A were 8×10^{21} , 1×10^{23} , and 1.8×10^{22} . The observed and calculated values are in good agreement especially since the G9 calculation would be an underestimate.

The charge exchange process favors ions moving nearly perpendicularly to **B**. These ions will spend the most time within the denser part of the neutral cloud and hence are

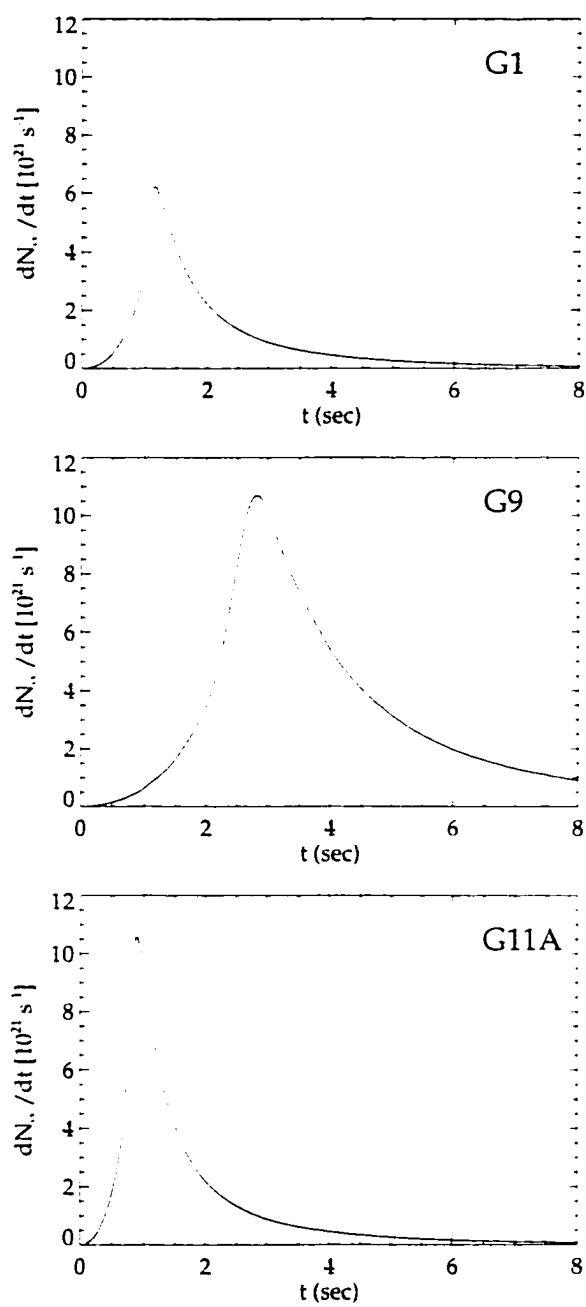


Figure 3.3: Calculated charge exchange rates versus time.

most likely to charge exchange. Therefore the produced neutrals would have velocities primarily perpendicular to \mathbf{B} , and the resulting neutral cloud should, as observed, appear as a disk perpendicular to \mathbf{B} and centered a few tens of kilometers from the release.

The charge exchange process only affects ions produced within the first few seconds after release, and with an ionization rate of 3% per second it is a significant fraction of the early time ions that are affected. Additionally, most of the early time ionization is inside the polarized core and therefore not subjected to charge exchange. Therefore, the importance of barium ion neutral charge exchange process will be highly dependent on the actual release geometry.

3.4 Ion Cloud Morphology

Our model of the skidding ion core is consistent with the observed initial skidding distance and the formation of the neutral disk. The observed ion cloud structures are presumably also related to the evolution of the core. However, this simple model can only describe the initial formation of the core and cannot address issues regarding the evolution of the core after about 1 second. In particular, we cannot address the herringbone structure with this model, so further discussion will follow with the hybrid code simulation. The observations do indicate, though, the presence of parallel electric fields. The ion cloud shows parallel elongation for 2-3 seconds after the release particularly at the striated release edge of the cloud. Despite the effects of highly mobile electrons along the field line, parallel electric fields are present and have been measured in the CRIT I experiment by *Brenning et al.* [1991a]. In this section we will consider the effects of a parallel electric field on the ion cloud morphology.

3.4.1 Polarization Electric Field Model

To evaluate the effects of parallel electric fields on the G1 ion cloud development, a three-dimensional particle simulation model was developed using the general model considerations described above. The computer model follows a large number ($\sim 10^5$) of particles in the geomagnetic field under the influence of an imposed polarization electric field. Each neutral Ba particle was initialized with the satellite velocity of 9.6 km/s plus an appro-

appropriate cloud expansion velocity so that the velocity distribution of the particle ensemble satisfied 1.3. These particles were then ionized according to a Monte Carlo algorithm using a 23 s time constant.

The imposed polarization electric field is assumed to be that of a polarized sphere. In a vacuum model of the release the field outside the polarization charge layers is dipolar. One consequence of this is that the electric field will have a component parallel to \mathbf{B} . The \mathbf{E} field inside the polarized cloud will result in an electrostatic potential across the ion cloud, and closure of the potential contours implies a parallel electric field in the vicinity of the ion cloud. Clearly, the ionospheric response to the potential drop along \mathbf{B} will quickly limit the parallel fields, but for the sake of simplicity we are neglecting this response in order to model the effects of parallel fields on the ion cloud morphology.

In Cartesian coordinates with x along the orbit, y along $-\mathbf{v} \times \mathbf{B}$, and z along \mathbf{B} , the electric field inside the sphere in the satellite frame of reference is

$$\mathbf{E}(x, y, z) = \left(0, \frac{-Q}{3\pi\epsilon_0 R^2}, 0 \right) \quad (3.8)$$

where Q is the polarization charge on the sphere and R is the radius of the expanding cloud. The skidding electric field is $-\mathbf{v} \times \mathbf{B}/B^2$, which for the three releases is about 300 mV/m. Outside the sphere the electric field is dipolar:

$$\mathbf{E}_{out}(x, y, z) = \frac{p}{4\pi\epsilon_0} \left(\frac{3xy}{r^5}, \frac{3y^2}{r^5} - \frac{1}{r^3}, \frac{3yz}{r^5} \right) \quad (3.9)$$

where the dipole moment $p = 4QR/3$ and $r = \sqrt{x^2 + y^2 + z^2}$. Hence the electric field is determined everywhere given the radius R of the polarized core.

Note that the electric field configuration described by 3.8 and 3.9 requires of the order of a gyroperiod (0.3 s) to be established. Therefore a more accurate model would be a rotating dipole which begins in the x direction and rotates to the y direction as described by Brenning et al. [Brenning et al., 1991a]. The rotating dipole has also been verified in the simulation work done by Genoni et al. [1995]. For the present calculations, however, we assume that 3.8 and 3.9 hold from the beginning.

The polarization charge Q controls the magnitude of the electric field. We used the observed skidding distance of 9.6 km for the G1 release as the criterion for setting the value of Q . For the first second the model uses $E_{in} = vB = 300$ mV/m to simulate the skidding.

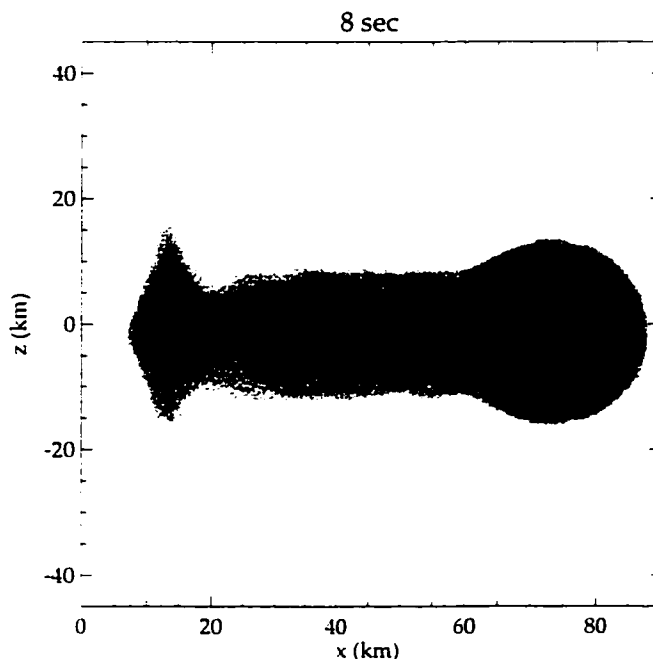


Figure 3.4: Early ion cloud structuring. Simulation results showing the early ion cloud structuring due to an imposed polarization electric field.

The value for Q corresponding to $E_{in} = 300$ mV/m at 1 s is then used to determine the electric fields for the remainder of the simulation.

The results from the simulation at 8 s after release are shown in Figure 3.4. The simulation image shows the results projected onto the xz plane to approximate the viewing geometry of G1 from aircraft 127. The model image is to be compared with the corresponding observed images. Note that the ion cloud shows a distinct striation along the release end of the ion cloud and shows considerable structure extending 20-25 km into the ion cloud. This is in good agreement with the observations.

While the model results are encouraging, it should be noted that the actual physical mechanism for supporting a parallel electric field is yet unknown. As mentioned above, the vacuum model of the release is unrealistic due to the mobility of the electrons along the magnetic field line. *Brenning* [1995] argues that the vacuum model may hold for up to 0.3 s after release, but not for 2-3 seconds as the observations suggest. Other possibilities include plasma instabilities or ambipolar diffusion resulting from CIV electron heating. Further discussion will follow in chapter 6.

3.5 Closure

This preliminary analysis of the G1, G9, and G11A optical data has yielded the following insights into the early ion dynamics of the CRRES releases:

- A dense core of ions is formed during the first few seconds of the release. This core polarizes and propagates across the geomagnetic field (i.e. skids) in the satellite direction for several seconds after the release. The analysis also suggests that the initial skidding distance is a function of the ratio between the barium ion density and the ambient plasma density.
- Charge exchange between barium ions and neutrals is responsible for the neutral disk that expands perpendicular to \mathbf{B} at the satellite velocity of 9.6 km/s. Significant charge exchange does not occur until 1-2 seconds after release when magnetized ions are produced outside of the skidding core. As the cloud expands and ion densities decrease, the number of charge exchanges decreases to essentially zero by 5-8 seconds after release.
- A parallel electric field is responsible for the elongation of the ion cloud near the release point. Parallel fields are an essential feature of a spherical, polarized cloud, but the highly mobile ambient electrons will quickly modify the charge distribution that is responsible for this parallel field. Instead, ambipolar diffusion or plasma instabilities may play an important role in the formation of the parallel electric fields.

Although this preliminary analysis has yielded new insights into the coupling between a partially ionized neutral gas and an ambient plasma, we still lack a quantitative understanding of the processes responsible for the structure, the effects of the release on the ambient environment and the dissipation of the kinetic energy of the barium ions. In particular, important questions still to be addressed include:

- Can the inner edge striation and ion cloud elongation be accounted for by anomalous electron heating?
- Do conditions exist for the generation of the modified two-stream instability?

- How do charge exchange processes alter the ion and neutral distribution functions?
- How rapidly does the barium plasma cloud exchange momentum and energy with the ambient plasma, and how does this propagate away from the ion cloud? That is, how does the skidding core couple to the ambient plasma, and what is its lifetime?

The next chapter introduces the hybrid code simulation that we used to address these questions.

Chapter 4

Hybrid Code

The CRRES chemical releases represent a challenging physical system for numerical simulation. Kinetic processes associated with the barium ions must be addressed, while the momentum coupling of the barium ions to a vast ambient ion population must be included. Ideally, we would use a full electromagnetic code and treat all species as discrete particles. However, the time stepping scheme for an electromagnetic code is limited by the propagation of light. The Courant condition for numerical stability requires that $\Delta t \leq \Delta_{min} / |v|$ where Δ_{min} is the minimum grid spacing and $|v|$ fastest propagation velocity on the space mesh. Moreover, the electromagnetic code contains the electrostatic interaction which requires time stepping to resolve the electron plasma oscillation. Both of these constraints require too small a time step to be feasible.

The hybrid code of the type developed by *Harned* [1982] offers a reasonable solution. The hybrid code assumes quasi-neutrality, and treats the barium ions as fully kinetic particles, and the electrons as a massless fluid. The ambient ionospheric plasma, considered here as composed entirely of oxygen ions, exhibits little kinetic behavior, and thus the computation is greatly simplified by treating this component as an MHD fluid. The inclusion of an ion fluid into the hybrid code was demonstrated by *Swift* [1996] whose algorithms are detailed below.

4.1 Algorithms

The equations of motion for the Ba⁺ ion particles, the O⁺ ion fluid, the massless electron fluid, and the update of the electric and magnetic fields are described in this section. The electric fields are determined algebraically from the electron momentum equation and the magnetic field update follows using Faraday's law. The algorithm is entirely explicit and there is no requirement for the solution of Poisson's equation or any other elliptic equations.

First, the electron momentum equation is

$$m_e \frac{d\mathbf{u}_e}{dt} = -q\mathbf{E}' - q\mathbf{u}_e \times \mathbf{B}' - m_e \nu(\mathbf{u}_e - \mathbf{u}_i) - \frac{1}{n} \nabla P \quad (4.1)$$

Dividing both sides by m_e simplifies the expression for the sake of computational convenience so that the electric fields can be written explicitly as

$$\mathbf{E} = -\mathbf{u}_e \times \mathbf{B} - \nu(\mathbf{u}_e - \mathbf{u}_i) - r \frac{d\mathbf{u}_e}{dt} - \nabla P \quad (4.2)$$

where \mathbf{E} is the electric field in units of O⁺ ion acceleration, \mathbf{B} is the magnetic field in units of O⁺ ion gyro frequency, P is the pressure in units of O⁺ ion velocity squared, ν is the ion-electron collision frequency, r is the electron-to-ion mass ratio, \mathbf{u}_e is the electron flow velocity, and \mathbf{u}_i is the total ion bulk flow velocity, given by

$$\mathbf{u}_i = \frac{n_p}{n} \mathbf{u}_p + \frac{n_f}{n} \mathbf{u}_f \quad (4.3)$$

where the subscripts p and f represent the particle and fluid constituents of the bulk flow.

It should be noted that from here forward, explicit references to barium and oxygen ions will be replaced by references to particle and fluid components respectively. The particle, fluid, and total densities are n_p , n_f , and n . The second term in 4.2 represents the ion-electron frictional dissipation necessary to stabilize the code against a nonlinear interaction between the particles and fields [Swift, 1995, 1996]. As it turns out, this term was for the most part unnecessary for the CRRES simulation. Note that the final term in 4.2 is an optional pressure term that can be used to evaluate the effects of anomalous electron heating. Given that the electron fluid is assumed massless, and hence electron inertial effects are considered insignificant, equation 4.2 simplifies to

$$\mathbf{E} = -\mathbf{u}_e \times \mathbf{B} - \nu(\mathbf{u}_e - \mathbf{u}_i) - \nabla P \quad (4.4)$$

Clearly the electron pressure term requires an additional equation for energy transport for a fully self self-consistent code. However, this pressure term is used without an energy transport equation simply to provide a diagnostic tool for evaluating the effects of anomalous (CIV) electron heating on the ion cloud morphology.

The electron flow speed is evaluated from Ampere's law

$$\mathbf{u}_e = \mathbf{u}_i - \frac{\nabla \times \mathbf{B}_1}{\alpha n} \quad (4.5)$$

where in mks units, $\alpha = \frac{\mu_0 e^2}{m_{O^+}}$ and where m_{O^+} is the ion fluid mass. The value of α is used to scale the simulation particle densities to their appropriate physical values.

Faraday's law is then used to update the first order magnetic fields

$$\frac{\partial \mathbf{B}_1}{\partial t} = -\nabla \times \mathbf{E} \quad (4.6)$$

which upon using 4.4 and 4.5 yields,

$$\frac{\partial \mathbf{B}_1}{\partial t} = -\nabla \times \left[\left(\frac{\nabla \times \mathbf{B}_1}{\alpha n} - \mathbf{u}_i \right) \times \mathbf{B} - v \frac{\nabla \times \mathbf{B}_1}{\alpha n} \right] \quad (4.7)$$

Note that $\mathbf{B} = \mathbf{B}_0 + \mathbf{B}_1$, where \mathbf{B}_0 is the ambient curl free geomagnetic field, and \mathbf{B}_1 is the variable field. With the equation for the magnetic fields written in this form, it can be shown that the first term on the right hand side is responsible for the propagation of the whistler mode, and the second term, together with the particle/fluid equations, propagates the Alfvén modes.

Using 4.3, 4.4, and 4.5, the equation for ion (Ba^+) particle motion is

$$\frac{d\mathbf{v}}{dt} = \mathbf{E}_p + \mathbf{v} \times \mathbf{B} \quad (4.8)$$

where

$$\mathbf{E}_p = \left(\frac{\nabla \times \mathbf{B}_1}{\alpha n} - \mathbf{u}_i \right) \times \mathbf{B} - v \frac{n_f}{n} (\mathbf{u}_f - \mathbf{u}_p) - \nabla P \quad (4.9)$$

Similarly, the ion (O^+) fluid velocity is

$$\frac{\partial \mathbf{u}_f}{\partial t} = \mathbf{E}_f + \frac{n_p}{n} \mathbf{u}_f \times \mathbf{B} - v \frac{n_p}{n} \mathbf{u}_f \quad (4.10)$$

where

$$\mathbf{E}_f = -(\mathbf{u}_f \cdot \nabla) \mathbf{u}_f + \left(\frac{\nabla \times \mathbf{B}}{\alpha n} - \frac{n_p}{n} \mathbf{u}_p \right) \times \mathbf{B} - v \frac{n_p}{n} \mathbf{u}_p - \nabla P \quad (4.11)$$

Note that the expressions for \mathbf{E}_p and \mathbf{E}_f are different than the expression for \mathbf{E} given by 4.4 and 4.5. This ordering of the terms was made for the sake of computational convenience.

Finally, as was mentioned in chapter 3, the barium cloud is basically a low-beta plasma. Figure 3.1, shows that any substantial perturbation to the ambient magnetic field is likely to occur only within the first second. Although we expect diamagnetic effects and magnetic field line compression associated with the skidding core, the ambient fluid is assumed fixed. Ambient density fluctuations due to electrostatic snowplow effects discussed by *Schunk and Szuszczewicz [1991]* will therefore not be present in this simulation. Errors related to the assumption of fluid incompressibility are accounted for in the momentum conservation of the hybrid code.

4.2 Time Stepping Algorithm

Equations 4.4, 4.7, 4.5, 4.8, and 4.10 represent the basis of the simulation. This section describes the subcycle time stepping scheme of *Swift [1996]* and the numerical algorithms that were used to solve this set of equations.

The time stepping scheme uses two time intervals. The barium particles are updated with one time step while the fluid and fields are updated on 10 subcycle time steps. This scheme provides substantial time savings as the number of particles in the simulation increases. Moreover, the subcycle time step is governed by the Courant condition with respect to the whistler mode which is much smaller than the time step that is required for resolving the barium ion gyromotion. Thus, it is not necessary for the particles to follow the fluid and field time stepping. Figure 4.1 illustrates the temporal relationship between the particle, fluid, and field quantities.

For the particle update, the half time step velocities are used to move the particles to the next whole time step. First, we assume that \mathbf{B} and \mathbf{u}_f are given at the whole time step. The update of \mathbf{v}_p from $n-\frac{1}{2}$ to $n+\frac{1}{2}$ requires \mathbf{E}_p at the whole time step. However, \mathbf{E}_p is calculated from \mathbf{u}_p which is only given at the half time steps, so the scheme uses a provisional extrapolation of \mathbf{u}_p to the whole time step

$$\mathbf{u}_p^n = 1.5\mathbf{u}_p^{n-\frac{1}{2}} - 0.5\mathbf{u}_p^{n-\frac{3}{2}} \quad (4.12)$$

Now, \mathbf{E}_p can be calculated at the whole time step.

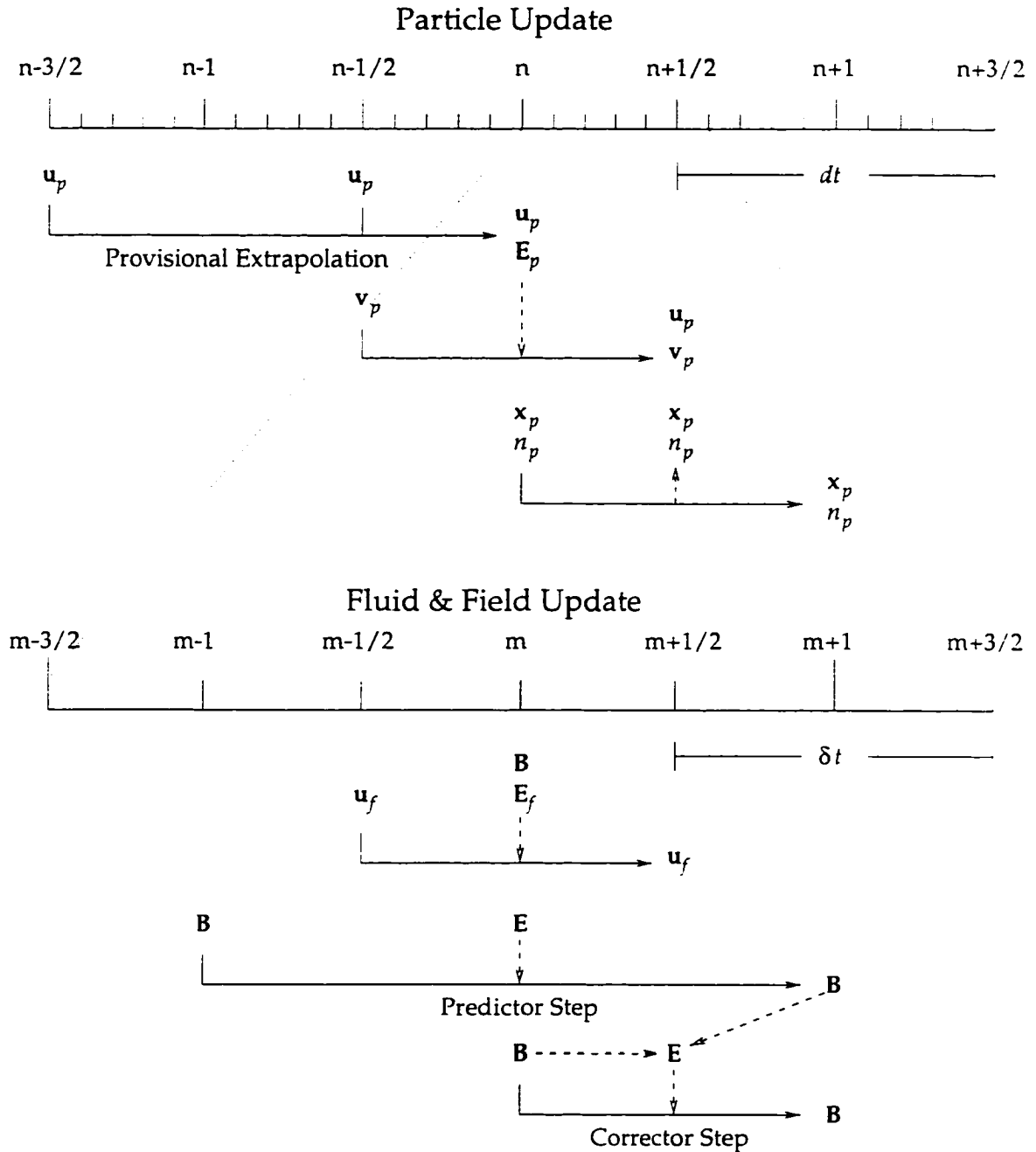


Figure 4.1: The time stepping algorithm. A summary of the time stepping algorithm showing the temporal relationship between particle, fluid, and field variables. The particle positions (densities) at the half time step, $n+1/2$, are used to update the fluid and field quantities (on the subcycle time step) from time level n to $n+1$. The subcycle time step, δt , is $dt/10$.

Next the algorithm uses the substitution of

$$\mathbf{v}^{\pm} = \mathbf{v}^{n \pm \frac{1}{2}} \mp \frac{\Delta t}{2} \mathbf{E}_p^n \quad (4.13)$$

into 4.8. The second order velocity advance is now given by

$$\mathbf{v}^+ = \mathbf{v}^- + \frac{\Delta t}{2} (\mathbf{v}^+ + \mathbf{v}^-) \times \mathbf{B}^n \quad (4.14)$$

and by computing the dot and cross products of 4.14 with \mathbf{B} we find that the explicit expression for \mathbf{v}^+ is

$$\mathbf{v}^+ = \frac{1}{1 + \frac{\mathbf{B}^2 \Delta t^2}{4}} \left[\left(1 - \frac{\mathbf{B}^2 \Delta t^2}{4} \right) \mathbf{v}^- + \Delta t (\mathbf{v}^- \times \mathbf{B}) + \frac{\Delta t}{2} (\mathbf{v}^- \cdot \mathbf{B}) \mathbf{B} \right] \quad (4.15)$$

However, before solving 4.14 for $\mathbf{v}^{n+\frac{1}{2}}$ we use

$$\mathbf{v}^n = \frac{1}{2} (\mathbf{v}^+ + \mathbf{v}^-) \quad (4.16)$$

to calculate an improved \mathbf{u}_p . The procedure is then repeated to obtain a final value for $\mathbf{v}^{n+\frac{1}{2}}$. Given the half time step velocities, the particle positions and densities are updated to the next whole time step ($n+1$).

The fluid and field values are updated on the subcycle time step from time level n to $n+1$ using the particle bulk flow and density at $n+\frac{1}{2}$. It should be noted that *Swift* [1996] found negligible differences between using the half time step values and using the values interpolated to the correct second-order subcycle time step. Thus we used $\mathbf{u}_p^{n+\frac{1}{2}}$ and $n_p^{n+\frac{1}{2}}$ for the duration of the subcycle loop. The ion fluid velocity, \mathbf{u}_f , is updated on the subcycle half time steps using the same procedure as described above for the discrete particle advancement. We first substitute

$$\mathbf{u}_f^{\pm} = \mathbf{u}_f^{m \pm \frac{1}{2}} \mp \frac{\delta t}{2} \mathbf{E}_f^m \quad (4.17)$$

into 4.10. This yields

$$\mathbf{u}_f^+ = \mathbf{u}_f^- + \frac{n_p \delta t}{2n} (\mathbf{u}_f^+ + \mathbf{u}_f^-) \times \mathbf{B}^m - v \frac{n_p \delta t}{2n} (\mathbf{u}_f^+ + \mathbf{u}_f^-) \quad (4.18)$$

Solving explicitly for \mathbf{u}_f^+ gives

$$\mathbf{u}_f^+ = \frac{1}{1 + Q^2 P} \left[(P - Q^2 B^2) \mathbf{u}_f^- + Q(1+P)(\mathbf{u}_f^- \times \mathbf{B}) + Q^2(1+P)(\mathbf{u}_f^- \cdot \mathbf{B}) \mathbf{B} \right] \quad (4.19)$$

where

$$P = \frac{1 - v \frac{n_p \delta t}{2n}}{1 + v \frac{n_p \delta t}{2n}} \quad (4.20)$$

and

$$Q = \frac{\frac{n_p \delta t}{2n}}{1 + v \frac{n_p \delta t}{2n}} \quad (4.21)$$

Substituting this result into 4.17 gives the updated velocity at the half time step. Note that in the regions where the ion particle density vanishes (i.e. outside of the release region), the second and third terms disappear, considerably simplifying 4.19.

The convective term in 4.11 was solved using a Lax-Wendroff scheme [Fletcher, 1991]. Under this scheme, the convective derivative of the form $\partial u / \partial t = -u \partial u / \partial x$ can be numerically represented by

$$u_i^{n+1} = u_i^n - \frac{1}{2} \frac{u \Delta t}{\Delta x} (u_{j+1}^n - u_{j-1}^n) + \frac{1}{2} \left(\frac{u \Delta t}{\Delta x} \right)^2 (u_{j-1}^n - 2u_i^n + u_{j+1}^n) \quad (4.22)$$

The last term on the right hand side is diffusive and is an expression for $\partial^2 u / \partial x^2$ which originates from a second-order representation for the term $\partial u / \partial t$ from a Taylor series expansion. Our numerical algorithm for $(\mathbf{u}_f \cdot \nabla) \mathbf{u}_f$ is thus represented by the second and third terms in 4.22. We added an adjustable coefficient for the diffusive term to ensure numerical stability, but in general found this to be unnecessary. Since \mathbf{E}_f is required at the whole subcycle time step, a provisional extrapolation of \mathbf{u}_f was made to the whole time step, and as was the case with the particle update, we improved the extrapolated value using u_f^- and repeated the calculation. Also, an upwind differencing scheme was used, but this scheme was overly diffusive so we elected not to use it.

Finally the magnetic field update uses a leapfrog-trapezoidal, or predictor-corrector technique [Zalesak, 1979]. The predictor step applied to Faraday's law (4.6) is

$$\tilde{\mathbf{B}}^{m+1} = \mathbf{B}^{m-1} - 2\delta t (\nabla \times \mathbf{E})^m \quad (4.23)$$

where \mathbf{E}^m is evaluated using $\mathbf{u}_f^m = \frac{1}{2} \left(\mathbf{u}_f^{m-\frac{1}{2}} + \mathbf{u}_f^{m+\frac{1}{2}} \right)$. The corrector step is

$$\mathbf{B}^{m+1} = \mathbf{B}^m - \delta t (\nabla \times \mathbf{E})^{m+\frac{1}{2}} \quad (4.24)$$

where the value of $\mathbf{E}^{m+\frac{1}{2}}$ is evaluated with $\frac{1}{2}(\tilde{\mathbf{B}}^{m+1} + \mathbf{B}^m)$

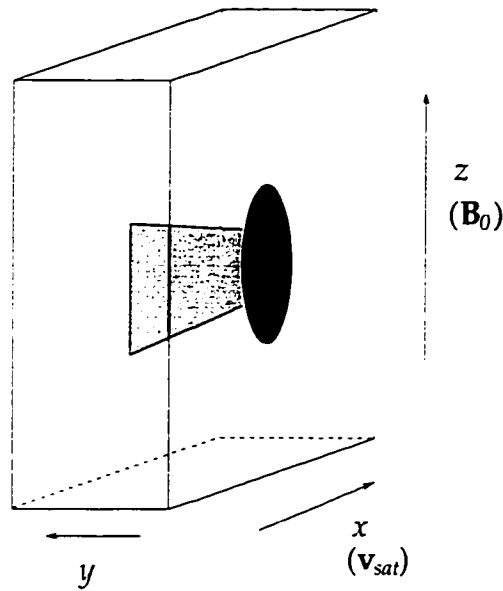


Figure 4.2: An illustration of the simulation coordinate system. The satellite velocity is in the x direction and the geomagnetic field is in the z direction

4.3 Simulation Coordinates and Grid Structure

The CRRES simulation coordinate system is illustrated in figure 4.2. The neutral cloud moves along the satellite orbit which is defined as the x direction. The ambient geomagnetic field is in the z direction, and the y direction completes the right-handed coordinate system. This Cartesian system represents a simplification to the inherently curvilinear geometry of the earth's dipole magnetic field; however, in the localized region of space occupied by the release cloud, geomagnetic curvature and gradients are negligible and the magnetic field can thus be considered constant. Beyond the release region the exact magnetic field topology is assumed to be of little importance as we are interested simply in the momentum coupling of the cloud to an arbitrary volume of ambient plasma. Boundary conditions at the conducting E-regions above (southern conjugate point) and below the cloud are clearly important and will be addressed in the next section.

To accommodate the large volume of ambient plasma, a non-uniform grid in the z direction is used. In the release region, the grid cell dimensions are one barium ion gyroradius as is necessary to resolve the ion gyromotion. Away from the release region, the grid

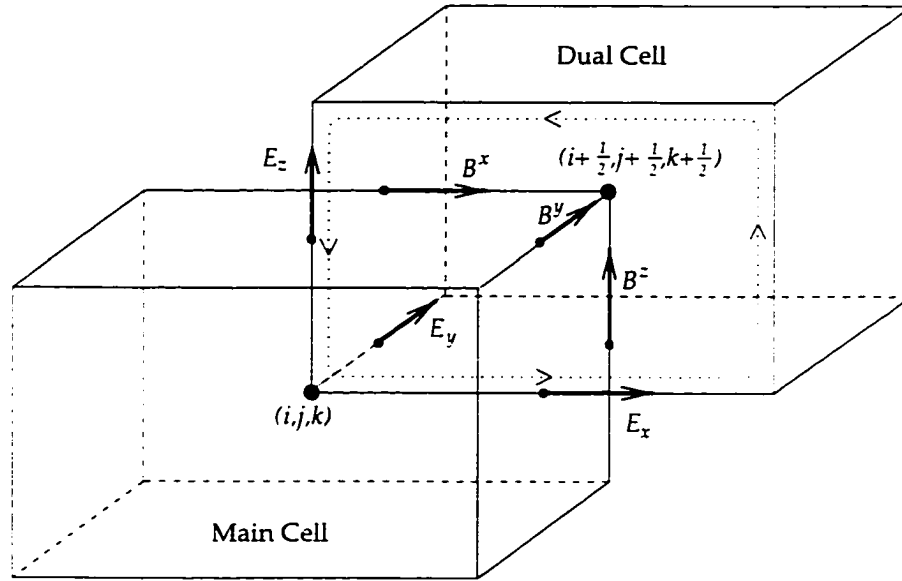


Figure 4.3: The coordinate cell. The coordinate cell showing the relationship between the main and dual cells, and the components of the electric and magnetic fields. The dotted line illustrates the line integral used for the advancement of B^y .

spacing is increased. The technique for performing vector operations on this non-uniform grid follows the procedure outlined by *Swift* [1996] for curvilinear coordinates.

The technique is illustrated in figure 4.3 which shows the orthogonal main grid cell and its partner, the *dual* cell. The center of the main cell is at the grid point (i, j, k) , and the center of the dual cell is at the main cell corner, $(i + \frac{1}{2}, j + \frac{1}{2}, k + \frac{1}{2})$. Note that on an irregular grid, the dual cell center and the geometric center of the dual cell will not necessarily coincide. The electric field components are defined on the main cell faces, or *contravariant* positions, and the magnetic field components are defined on the main cell edges (dual cell faces), or *covariant* positions. Under this convention, all other vector quantities are given at the contravariant positions.

The magnetic field advancement applies Stokes' theorem to Faraday's law

$$\int \frac{\partial \mathbf{B}}{\partial t} \cdot d\mathbf{A} = \oint \mathbf{E} \cdot d\mathbf{l} \quad (4.25)$$

Numerically, 4.25 applied to the point $(i + \frac{1}{2}, j, k + \frac{1}{2})$ as shown in figure 4.3 on the dual cell

face gives

$$\begin{aligned} \left[\frac{(B^y)^{n+1} - (B^y)^n}{\Delta t} \Delta x \Delta z \right]_{i+\frac{1}{2}, j, k+\frac{1}{2}} &= \left(E_x^{n+\frac{1}{2}} \Delta x \right)_{i+\frac{1}{2}, j, k} - \left(E_x^{n+\frac{1}{2}} \Delta x \right)_{i+\frac{1}{2}, j, k+1} \\ &+ \left(E_z^{n+\frac{1}{2}} \Delta z \right)_{i+1, j, k+\frac{1}{2}} - \left(E_z^{n+\frac{1}{2}} \Delta z \right)_{i, j, k+\frac{1}{2}} \end{aligned} \quad (4.26)$$

All curl operations follow this convention. Note, however, that in the case of Ampere's law, the curl operation is done on the main cell faces instead.

The formation of scalar and vector products require that the components of both vectors be located at the same point in space. This is particularly important in the case of the cross product, $(\nabla \times \mathbf{B}) \times \mathbf{B}$, which involves both covariant and contravariant vectors. The quantities are first interpolated to the main cell center where the vector operations are performed, and the results are interpolated back to the contravariant positions. All interpolations are linear.

The particle update uses a standard particle-in-cell (PIC) algorithm where the field and fluid quantities that are interpolated to the position of each particle using PIC weighting [Potter, 1977]. Likewise, the particle density, which is specified at the main cell center, is interpolated to the contravariant positions for the field and fluid updates. This method is illustrated in figure 4.4. The particle is located at the point P , and the eight nearest grid points are indicated. For example, the normalized weight for the quantity located at grid point 6 is $(x_1 y_1 z_1) / (\Delta x \Delta y \Delta z)$ where Δx , Δy , and Δz are the grid dimensions. In short, the weighting volume for each grid point is the subvolume in the opposite corner of the cell.

As a final point, the grid leaves the divergence of the magnetic field at the dual cell center divergenceless provided that the initial magnetic field configuration is divergenceless. This can be shown by applying the divergence theorem to 4.25, which over one grid cell is

$$\int_{cell} \frac{\partial}{\partial t} (\nabla \cdot \mathbf{B}) dV = \sum_{cell \text{ faces}} \int \frac{\partial \mathbf{B}}{\partial t} \cdot d\mathbf{A} = \sum_{cell \text{ faces}} \oint \mathbf{E} \cdot d\mathbf{l} \quad (4.27)$$

Note that the sum of the line integrals exactly cancel leaving the magnetic field divergenceless for all subsequent time steps.

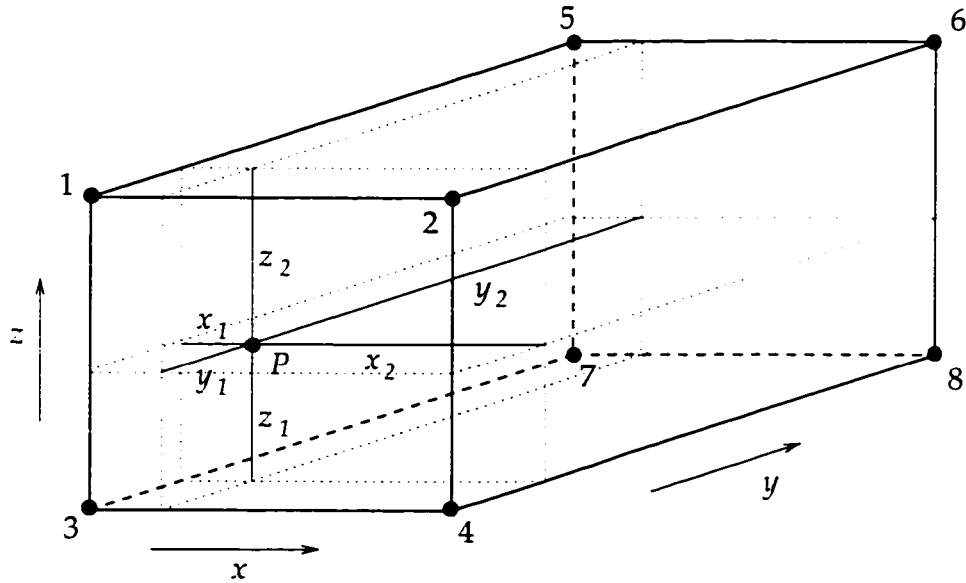


Figure 4.4: PIC weighting. An illustration of the particle-in-cell (PIC) weighing algorithm for interpolating fluid and field quantities to the particle positions and particle densities to the grid positions. The normalized weight for each grid point is the subvolume of the opposite corner of the cell divided by the cell volume.

4.4 Boundary Conditions

The simulation boundaries lie on dual cell faces, so we must specify the normal component of \mathbf{B} (\mathbf{B}_\perp) and the tangential components of \mathbf{E} (\mathbf{E}_\parallel) on the dual cell boundary face. Once \mathbf{E}_\parallel has been determined, Faraday's law gives \mathbf{B}_\parallel which in turn provides \mathbf{E}_\perp through Ampere's law. The normal component of \mathbf{B} is determined by requiring that the divergence of \mathbf{B} at the dual cell center just inside the boundary remain zero. This is the simplest of the two boundary conditions and applies to all boundaries. The tangential components of \mathbf{E} on the other hand can be specified in a number of ways. The easiest condition is for that of a conducting (reflecting) boundary where $\mathbf{E}_\parallel = 0$. We used this condition to simulate the conducting E-regions above¹ and below the release region. For the side boundaries perpendicular to \mathbf{B}_0 , we used $\partial_\perp \mathbf{E}_\parallel = 0$ to specify \mathbf{E}_\parallel on the boundary. This condition en-

¹The top boundary represents the conjugate E-region in the southern hemisphere. The Alfvén transit time to the conjugate point and back is on the order of several seconds, or certainly much longer than the time of this simulation. Although the proximity of this boundary to the simulation particles was unphysical (symmetric with the lower boundary), the Alfvén waves did not interact with this boundary during the simulations.

sured that the normal component of the fluid flow was continuous across the boundary and therefore is termed an *outflow* boundary condition [Swift, 1996]. Another option is to specify $\partial_{\perp} \mathbf{B}_{\parallel} = 0$ on the boundary in which case \mathbf{E}_{\parallel} is determined from Ampere's law; however, this specification tended to make the boundary rigid and reflecting (i.e. $\mathbf{E}_{\parallel} = 0$) rather than continuous as desired for an outflow boundary. The particles were confined to the central region of the simulation domain and thus never crossed the boundaries. Hence, particle boundary conditions were not necessary.

4.5 Energy and Momentum Conservation

Expressions for energy and momentum conservation for this hybrid code are derived in Appendix A and B. The result for energy conservation is

$$\frac{d}{dt} \left(\mathcal{E} + \frac{1}{\alpha} \int B_1^2 d^3x \right) = \int \frac{\mathbf{E} \times \mathbf{B}}{\alpha} \cdot d\mathbf{A} \quad (4.28)$$

This expression says that the time rate of change of particle and fluid kinetic energy, \mathcal{E} , and volume integral of magnetic field energy density is equal to the poynting flux at the boundary surfaces. Note that the electric field does not contribute to the energy conservation. We also account for ion fluid fluxes through the boundary surfaces, assuming no discrete particle fluxes through the boundaries.

The expression for momentum conservation is

$$\sum_{k=1}^{N_i} m_p \frac{d\mathbf{v}_k}{dt} + m_f n_f \int \frac{\partial \mathbf{u}_f}{\partial t} d^3x = \oint_S \vec{\mathbf{T}} \cdot d\mathbf{a} - m_f n_f \int (\nabla \cdot \mathbf{u}_f) \mathbf{u}_f d^3x \quad (4.29)$$

where the stress tensor, $\vec{\mathbf{T}}$, is given as

$$T_{ij} \equiv \frac{m_f}{\alpha} \left(B_i B_j - \frac{1}{2} \delta_{ij} B^2 \right) - m_f n_f u_{f_i} u_{f_j} \quad (4.30)$$

In 4.29, the total change in momentum of the system is equal to the stresses at the boundaries plus the second term on the right hand side which is the error that is introduced from our assumption that the ambient plasma density is fixed and thus incompressible. It turns out that this error is indeed small; however, a subroutine was added to solve the ion fluid continuity equation should it be needed.

Chapter 5

Simulation Results

5.1 Introduction

The results of five separate runs of the hybrid code are presented in this chapter. Results from a 2.6 s G9-type simulation provide the basis of the presentation, while four smaller 1.2 s G1-type runs illustrate the sensitivity of the code to the variation of several parameters. These parameters include barium ion density, ambient O^+ density, charge exchange and collisional processes, and electron temperature. The parameters for these five simulations are summarized in simulation units in table 5.1. All values presented here will be given in simulation units as discussed in the previous chapter.

Note that the initial magnetic field and ambient plasma density are constant over the entire simulation domain. We are only concerned with the momentum transfer from the particles to the ambient fluid medium, so the exact details of the variation of the ambient parameters away from the particle cloud are assumed to be of little importance to the simulation results. Furthermore, the physical extent of the simulation domain is limited to a region of the ionosphere where only the ambient plasma density varies significantly, and as will be shown below, variations to the ambient plasma density do not significantly affect the results.

The conducting boundaries at $z = 0$ and $z = nz$ were placed sufficiently far from the release region so that the Alfvén mode never reached the boundaries. If the momentum-carrying Alfvén wave should reach the boundaries, then the resulting magnetic tension

from the reflected wave would tend to further decelerate the skidding ion cloud. The irregular grid in the z direction facilitated the distant placement of these boundaries without adding an excessive number of grid points. In the release region the grid was uniform with a sufficient number of grid points to resolve the barium ion gyration, while the grid spacing along z was linearly increased from the minimum dz to the maximum dz shown in Table 5.1.

The ionization of the barium particles was initiated at 0.2 seconds, corresponding to the canister evacuation time. The ionization process used a Monte Carlo algorithm with a time constant of 23 s. We used this time constant for all five runs based on the observational evidence supporting this value. It turns out, regardless, that the results were insensitive to changes in the time constant within observational uncertainties. For the large G9 simulation, 500,000 particles were used, and 100,000 particles were used for the small G1 simulations. This ensured that at least 10 particles were present in each grid cell throughout the volume occupied by the particles.

5.2 G9 Release

Projections of the barium ion cloud in the xy (perpendicular) and xz ($v_{sat}B$) planes are shown in figure 5.1 at 0.2 s intervals. The color bar provides a relative intensity scale for the color scheme used. First, we note the formation of the dense skidding core. In the xy plane this core is a structure of roughly 2-3 km in diameter as expected from the preliminary calculations of Chapter 3. An asymmetry is also present where the core has drifted in the direction of the ion gyromotion. The xz plane projections show that the core has expanded along the magnetic field into a cylindrical structure as would be expected from the initial velocity distribution of the neutral cloud.

5.2.1 Skidding

Figure 5.1 shows that the core begins to lag behind the neutral cloud starting at 1.0 s. Note that the neutral cloud is coincident with the leading edge of the ion cloud. By the end of the simulation the core is only ~ 16 km from the release point while the center of the neutral cloud is roughly 25 km from the release point. Figure 5.2 shows the distribution of

	#1	#2	#3	#4	#5
Release size, N_0	1.8×10^{25}	2.6×10^{24}	2.6×10^{24}	2.6×10^{24}	2.6×10^{24}
Particle array size	500,000	100,000	100,000	100,000	100,000
Time step, Δt (s)	0.004	0.004	0.002	0.004	0.004
Number of time steps	600	250	500	250	250
Subcycle time step, δt (s)	0.0004	0.0004	0.0002	0.0004	0.0004
B_0 (T, s^{-1})			$3.0 \times 10^{-5}, 179.8$		
$v_{sat} B_0$ (km/s ²)			1726.1		
n_e (km ⁻³)	1.0×10^{21}	1.0×10^{21}	5.0×10^{20}	1.0×10^{21}	1.0×10^{21}
T_e (K)	0	0	0	0	1×10^5
Alfvén speed (km/s)	163.8	163.8	231.6	163.8	163.8
Max whistler mode speed (km/s)	641.3	641.3	1241.9	641.3	641.3
	<i>Grid dimensions</i>				
n_x	93	43	43	43	43
n_y	67	31	31	31	31
n_z	301	151	251	183	183
	<i>Physical extent of grid</i>				
dx (km)	0.4	0.4	0.4	0.4	0.4
dy (km)	0.4	0.4	0.4	0.4	0.4
minimum dz (km)	0.5	0.5	0.5	0.5	0.5
maximum dz (km)	6.5	4.5	4.5	4.5	4.5
x (km)	37.2	17.2	17.2	17.2	17.2
y (km)	26.8	12.4	12.4	12.4	12.4
z (km)	921.0	369.1	539.0	369.1	369.1
	<i>Collisional Processes</i>				
Charge Exchange	No	No	No	Yes	No
Billiard Collisions	No	No	No	Yes	No

Table 5.1: Parameters for the five hybrid code simulation runs of the CRRES releases.

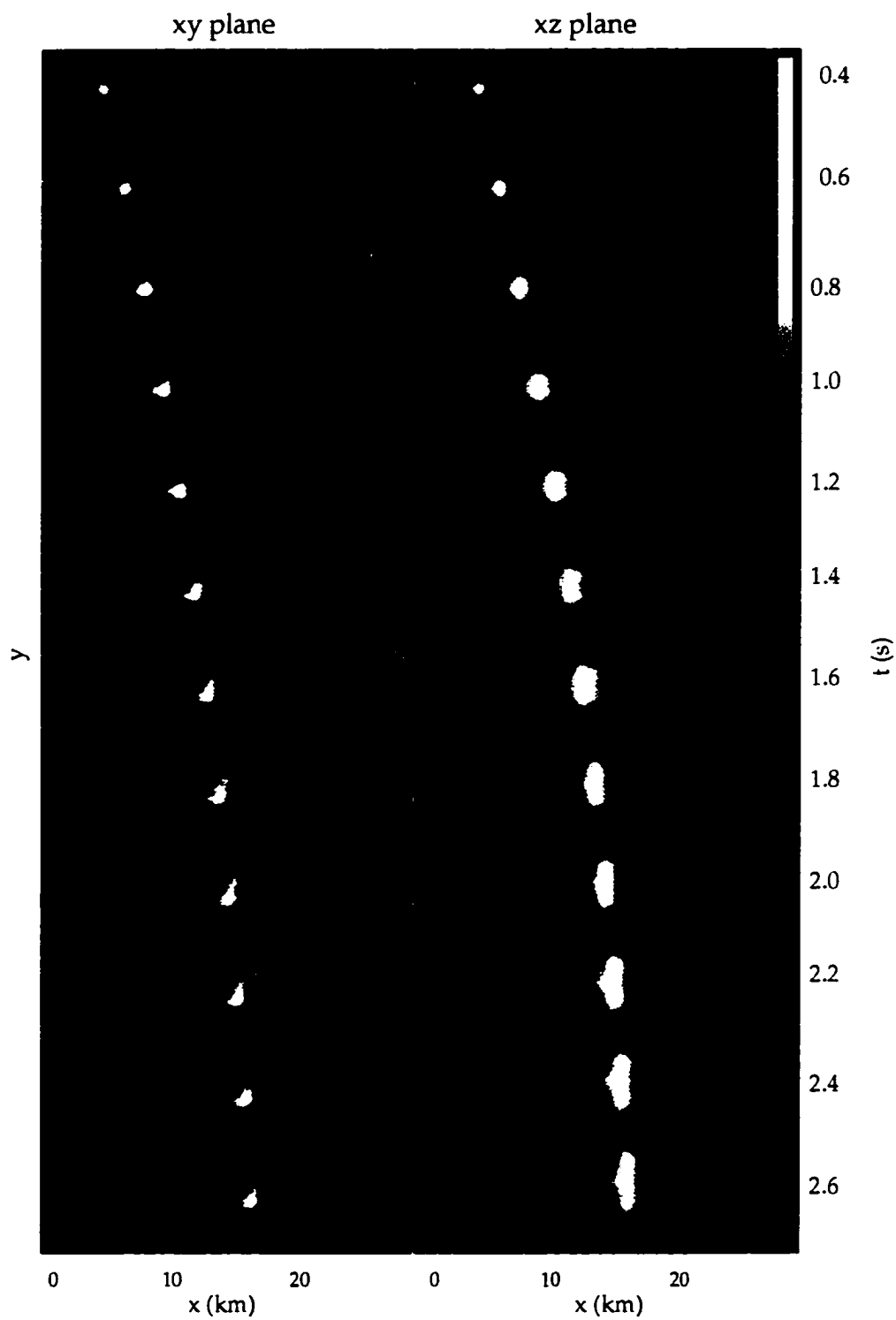


Figure 5.1: Projections of the barium ion densities in the xy and xz planes. The color bar shows the relative integrated column densities on a linear scale.

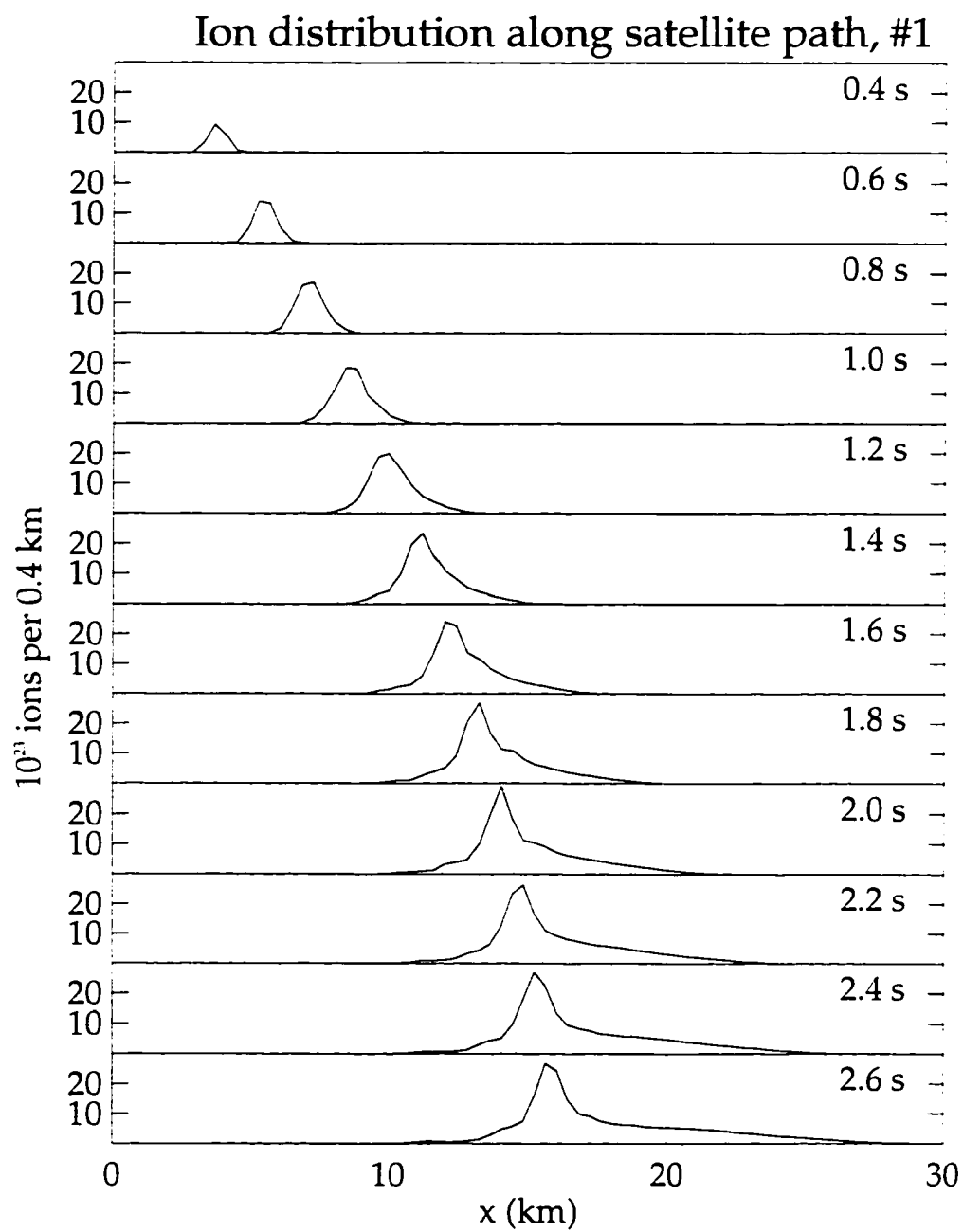


Figure 5.2: G9 ion distribution along the satellite path.

the ions along the satellite track (x axis) at the same 0.2 s intervals. These profiles are for comparison with the observed profiles in figures 2.9, 2.10, and 2.11. The simulation clearly shows that the core should have lost nearly all of its momentum by 2.6 s.

5.2.2 Ion cloud morphology

Figures 5.3, 5.4, and 5.5 illustrate the structures found within the ion cloud at 1.6 s. An asymmetry in the xy plane is evident. Much of the core remains intact; however, high density regions appear lagging behind and below as well as above and ahead of the main core. Cycloid bunching is evident in the xz -plane projections of figure 5.1 as well as the region between $x = 16$ km and $x = 19$ km in figure 5.3. The xz -plane slice in figure 5.4 reveals that the core has split into two parts with a herringbone structure forming from the trailing ions. The three-dimensional composite image shows that the split core appears in a localized region in the y direction.

5.2.3 Field and fluid quantities near the release region

Figures 5.6 through 5.17 show a comparison of the electric fields, first order magnetic fields, fluid flow, and currents in the vicinity of the particle ion cloud. The first frame in each figure is a contour plot of the particle density in the indicated plane. The electric, magnetic, and fluid velocities are illustrated by a representative vector field with magnitude of the longest vector specified to the right of the plot in simulation units (see Table 5.1 for reference values). The last frame shows a contour plot of the parallel currents passing through the xy plane in figures 5.6 to 5.11. In figures 5.12 to 5.17 the currents are shown with a vector field representation. Note that the xy -plane slices were taken from 1-4 grid points above the midplane of the ion cloud for the purpose of showing the parallel currents. The aspect ratio was maintained in these figures so the distance scale on the y and z axis is the same as the x axis.

The electric field as seen in the xy plane is dipolar and decays steadily in accordance with the momentum losses of the ion cloud. The magnetic field shows a circulation pattern that is consistent with the parallel current contours. The currents are filamentary and have an electron flow speed of up to 40 km/s initially. A higher grid resolution produced sub-

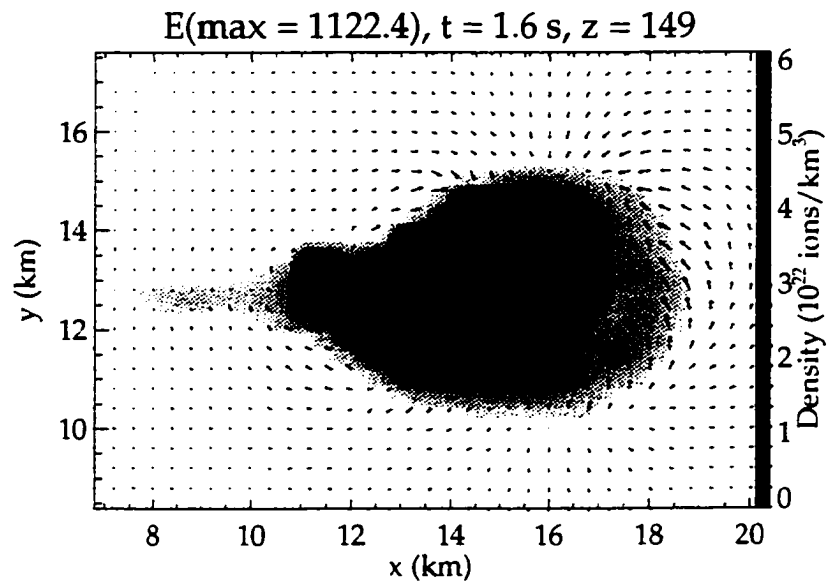


Figure 5.3: Ion cloud in the xy plane with electric field. Ion cloud in the xy plane at $z = 149$ and $t = 1.6$ s. The color scale to the right indicates the ion densities and the electric field vectors are shown.

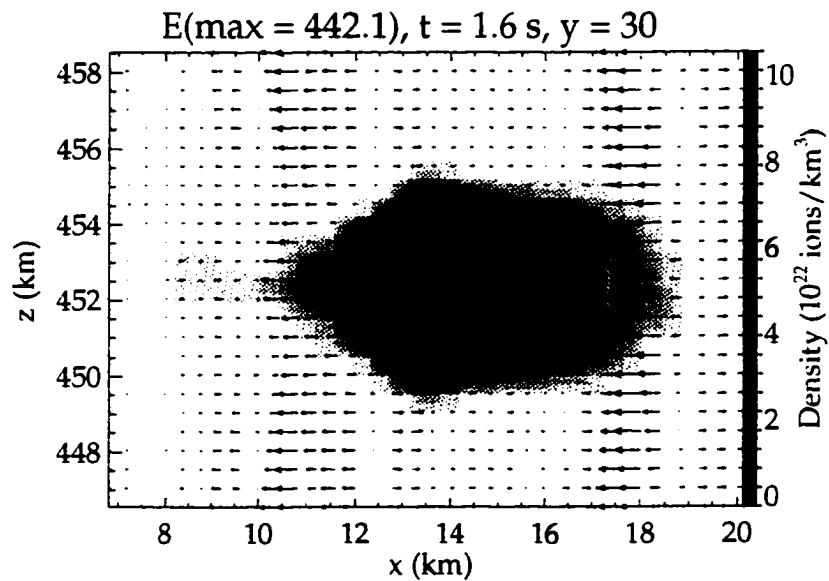


Figure 5.4: Ion cloud in the xz plane with electric field. Ion cloud in the xz plane at $y = 30$ and $t = 1.6$ s. The color scale to the right indicates the ion densities and the electric field vectors are shown.

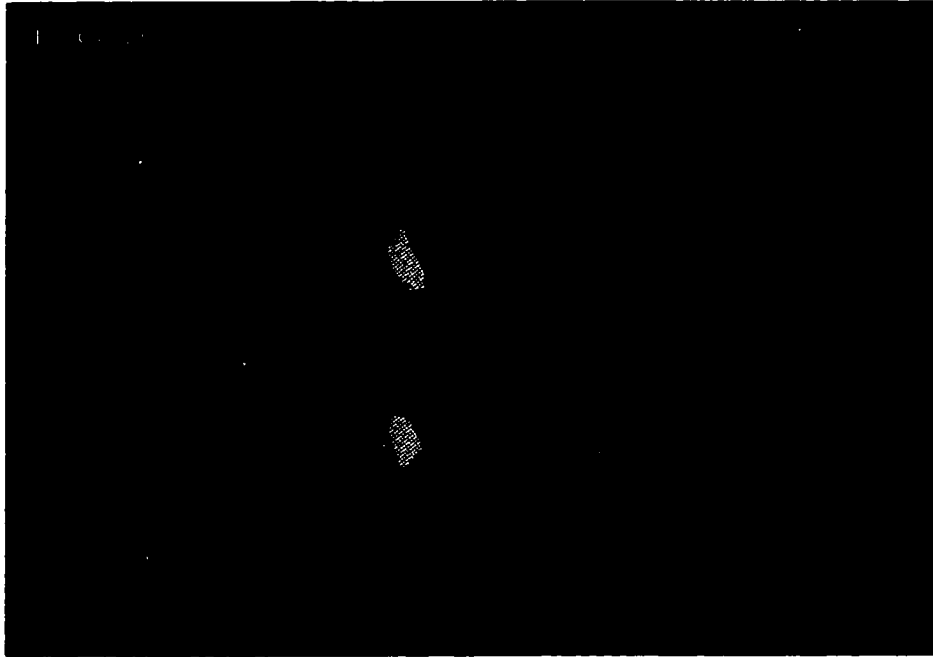


Figure 5.5: Slices of the ion cloud rendered in three-dimensions.

stantially higher electron flow speeds as the resolution of the current filaments increased. Slices taken below the midplane show a reversed magnetic field circulation which is consistent with the frozen-in condition for the particles and magnetic fields. This reversal is seen clearly in the xz plane slices both in the magnetic field and the parallel current flow. Also in the xz plane we see evidence of a diamagnetic cavity in the core region as well as circulation that implies a current flowing in the xy plane and forward of the core. The magnitude of the perpendicular current is roughly equal to the ion flow velocity of 5 to 10 km/s.

5.2.4 Field and fluid quantities away from release region

The particle momentum is carried away from the cloud primarily via Alfvén waves propagating along the magnetic field. The high frequency whistler modes propagate faster but carry very little momentum. Figures 5.18 through 5.23 illustrate the relationship between the field and fluid flow variables associated with this wave propagation at 2.6 s after the release in the midplane of the cloud. The grid has been resampled to a uniform grid for

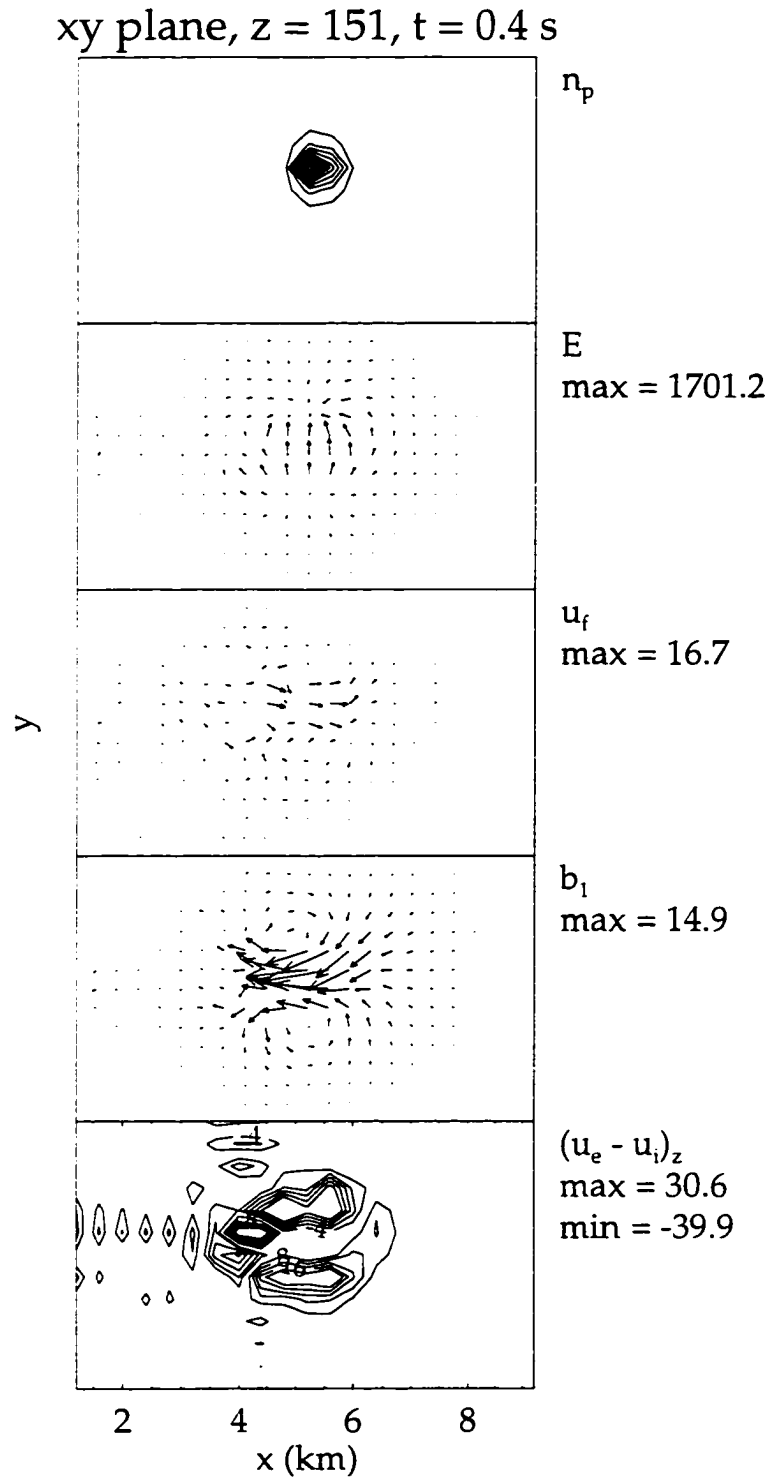


Figure 5.6: Field and fluid quantities in the xy plane at $z = 151$ and $t = 0.4$ s.

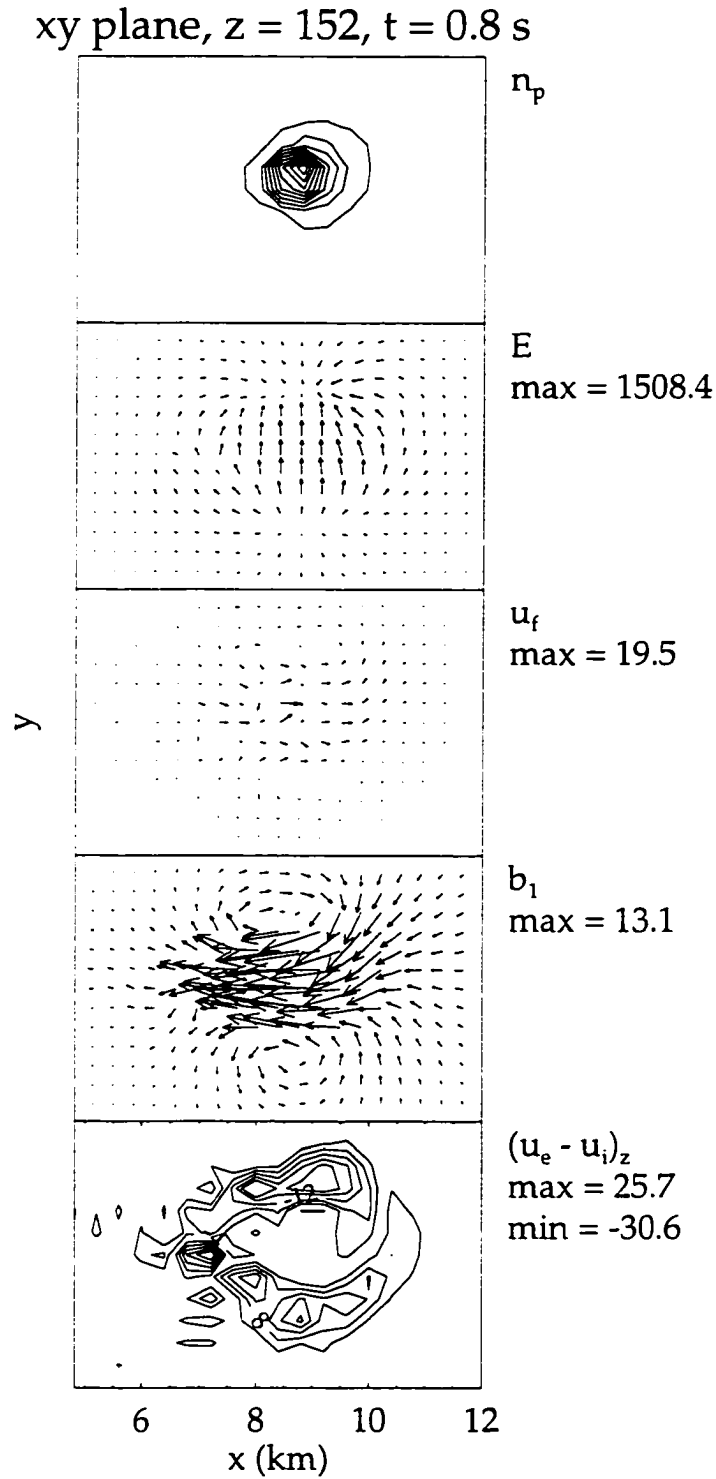


Figure 5.7: Field and fluid quantities in the xy plane at $z = 152$ and $t = 0.8$ s.

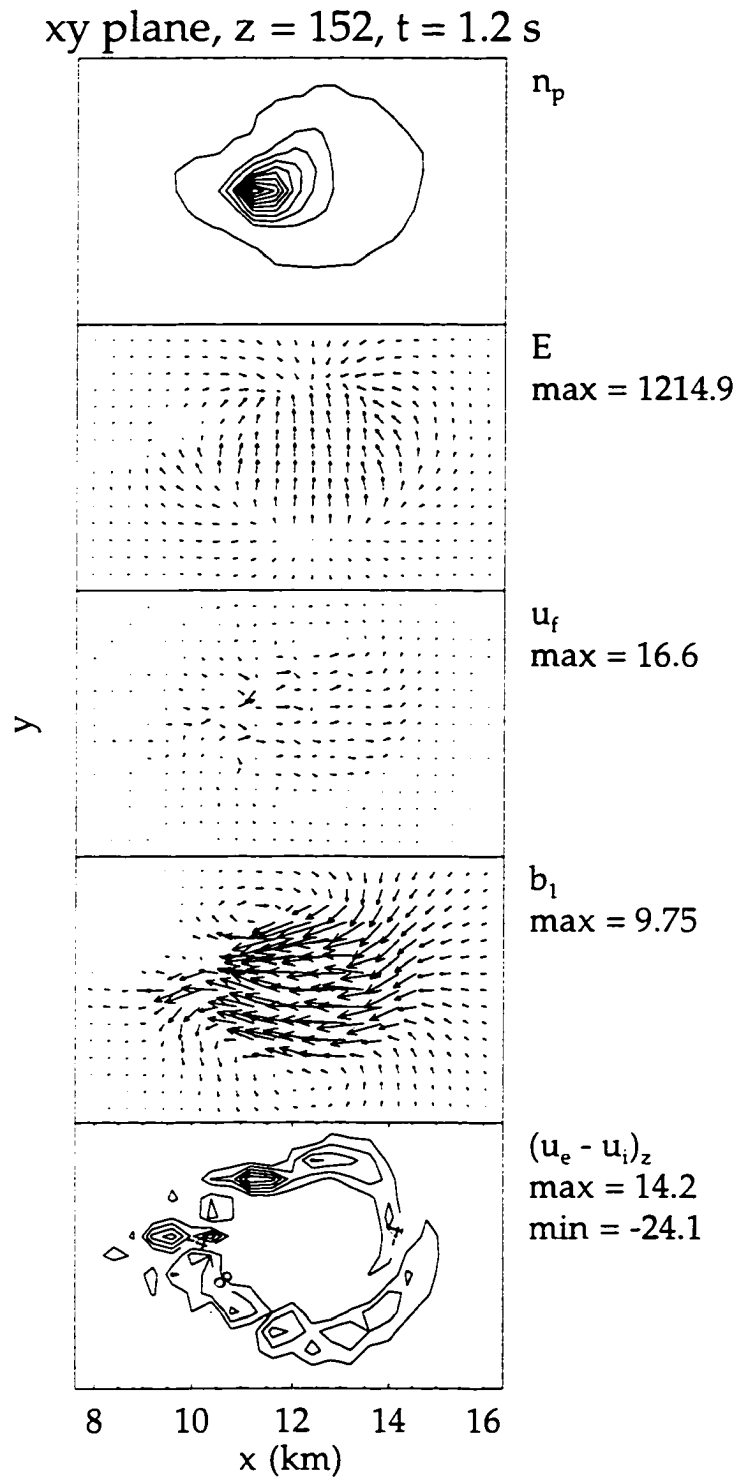


Figure 5.8: Field and fluid quantities in the xy plane at $z = 152$ and $t = 1.2$ s.

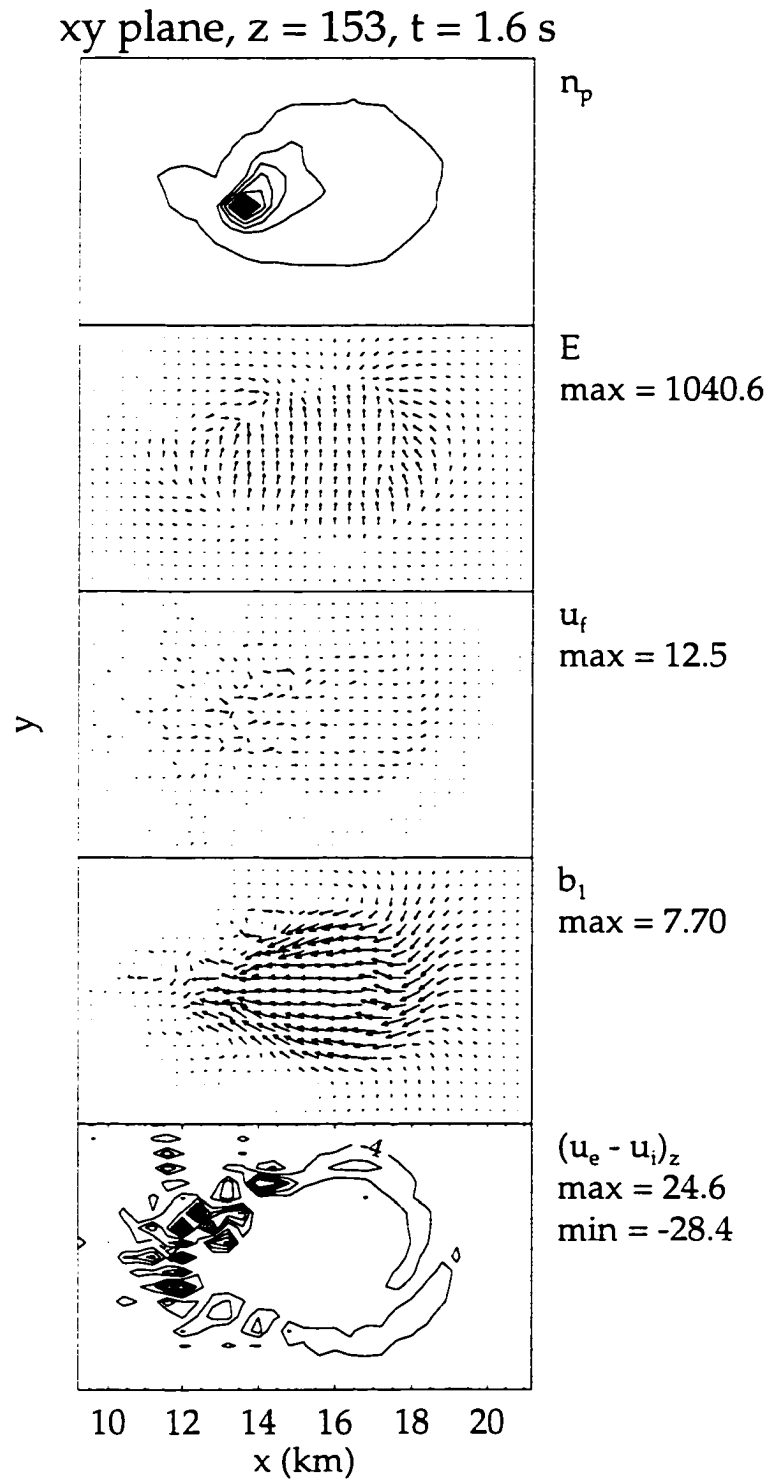


Figure 5.9: Field and fluid quantities in the xy plane at $z = 153$ and $t = 1.6$ s.

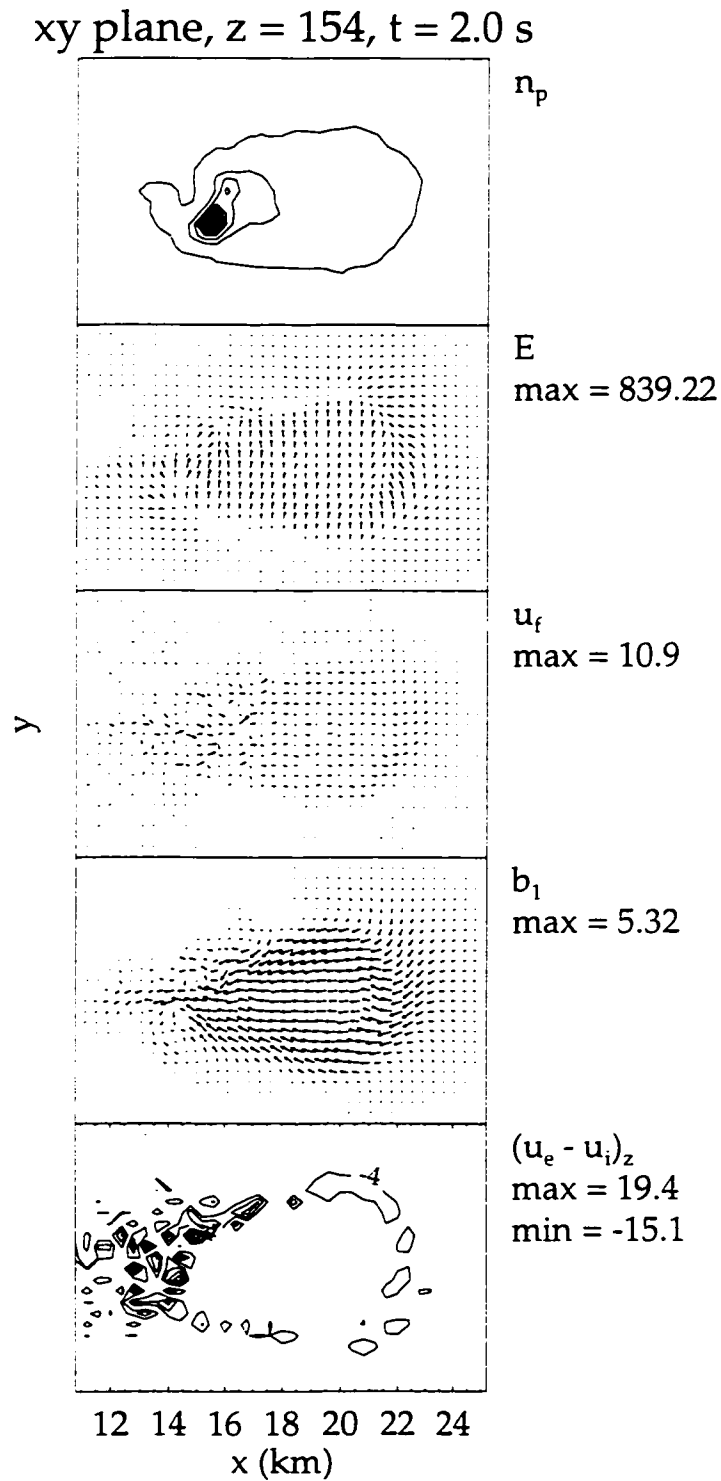


Figure 5.10: Field and fluid quantities in the xy plane at $z = 154$ and $t = 2.0$ s.

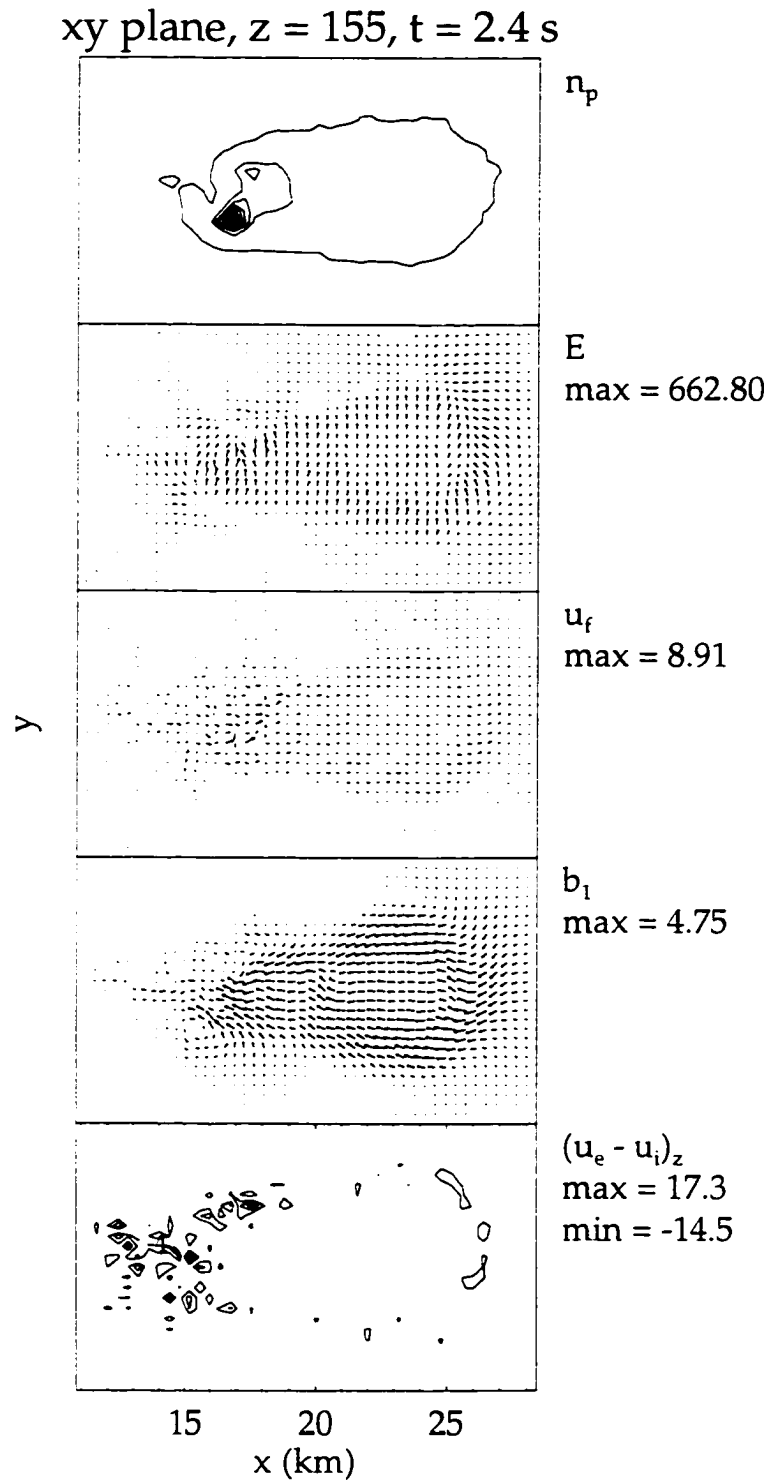


Figure 5.11: Field and fluid quantities in the xy plane at $z = 155$ and $t = 2.4$ s.

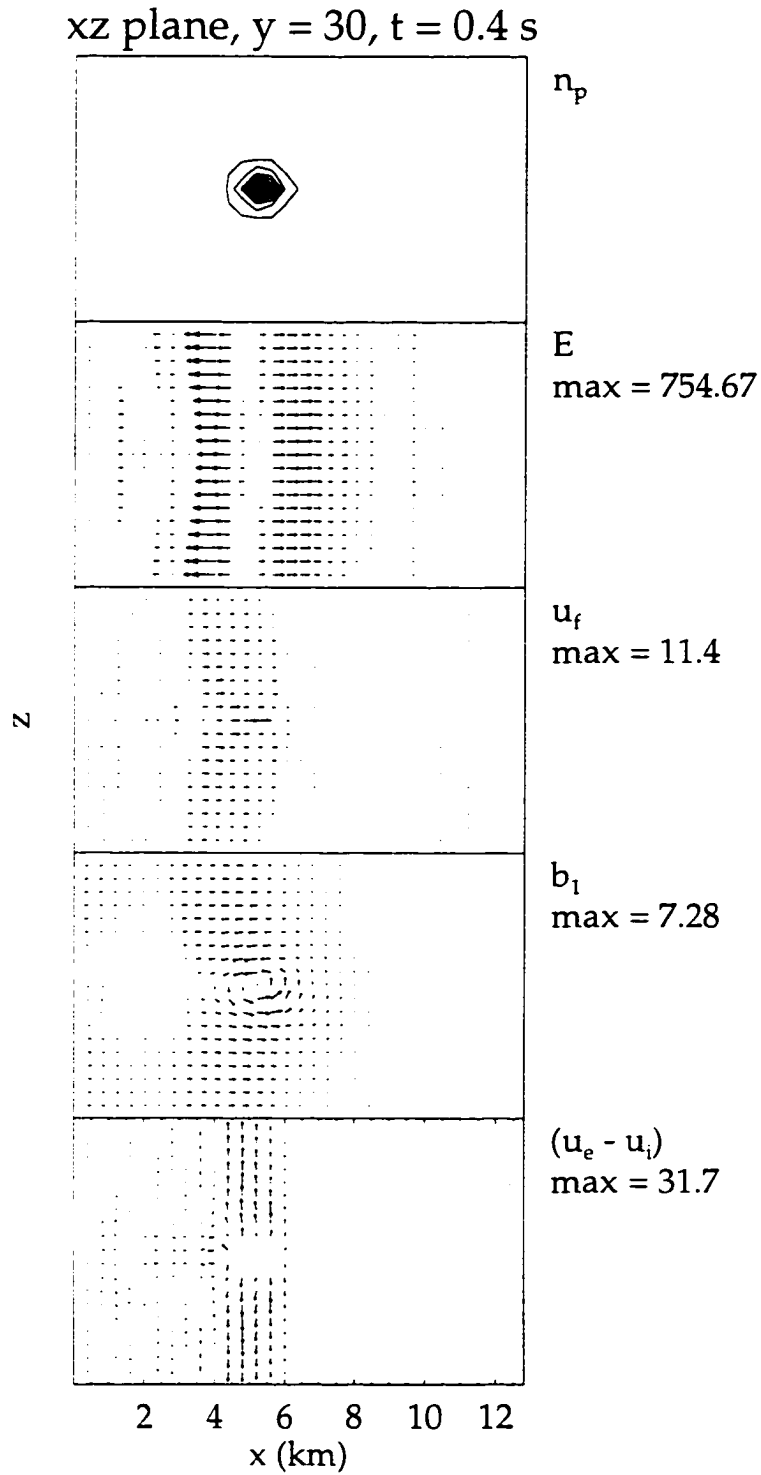


Figure 5.12: Field and fluid quantities in the xz plane at $y = 30$ and $t = 0.4$ s.

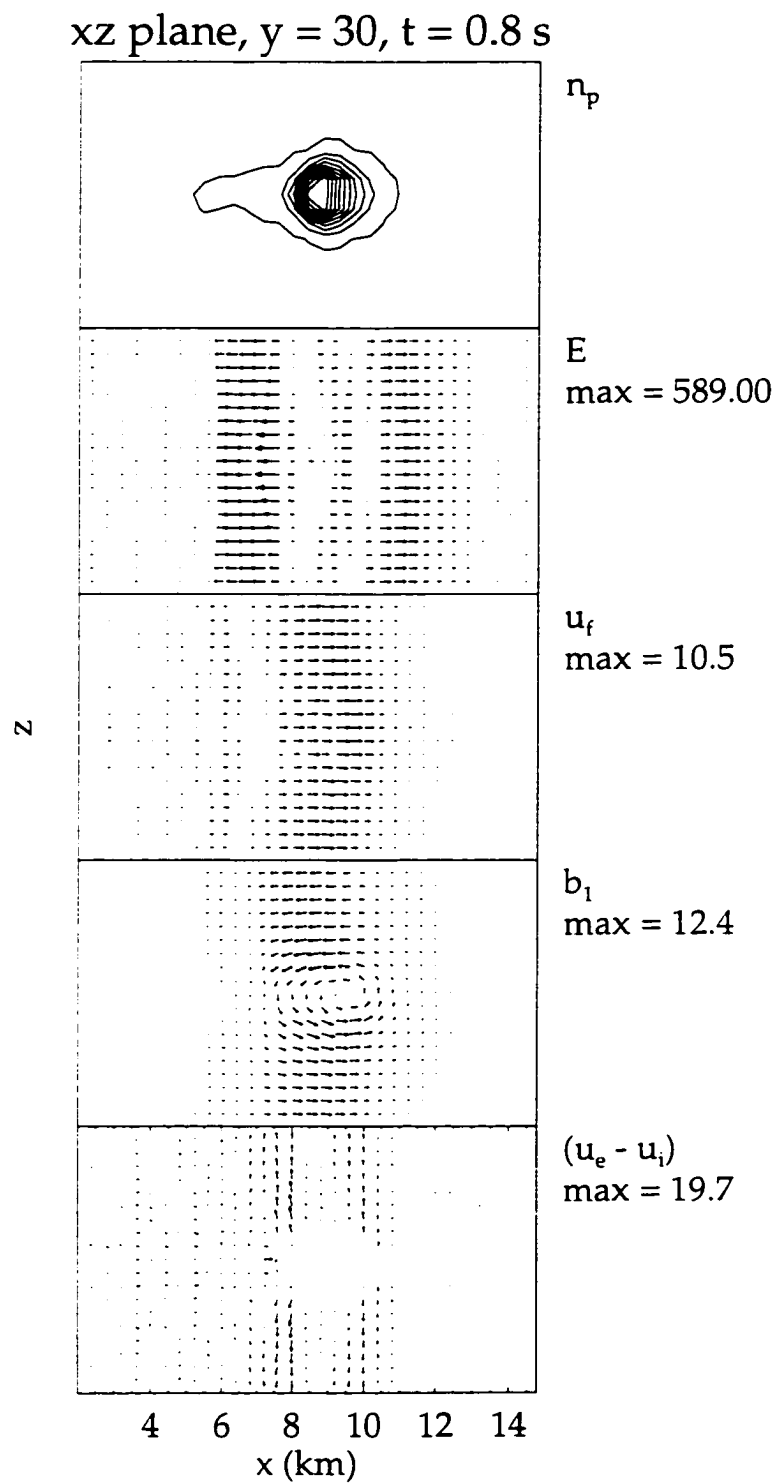


Figure 5.13: Field and fluid quantities in the xz plane at $y = 30$ and $t = 0.8$ s.

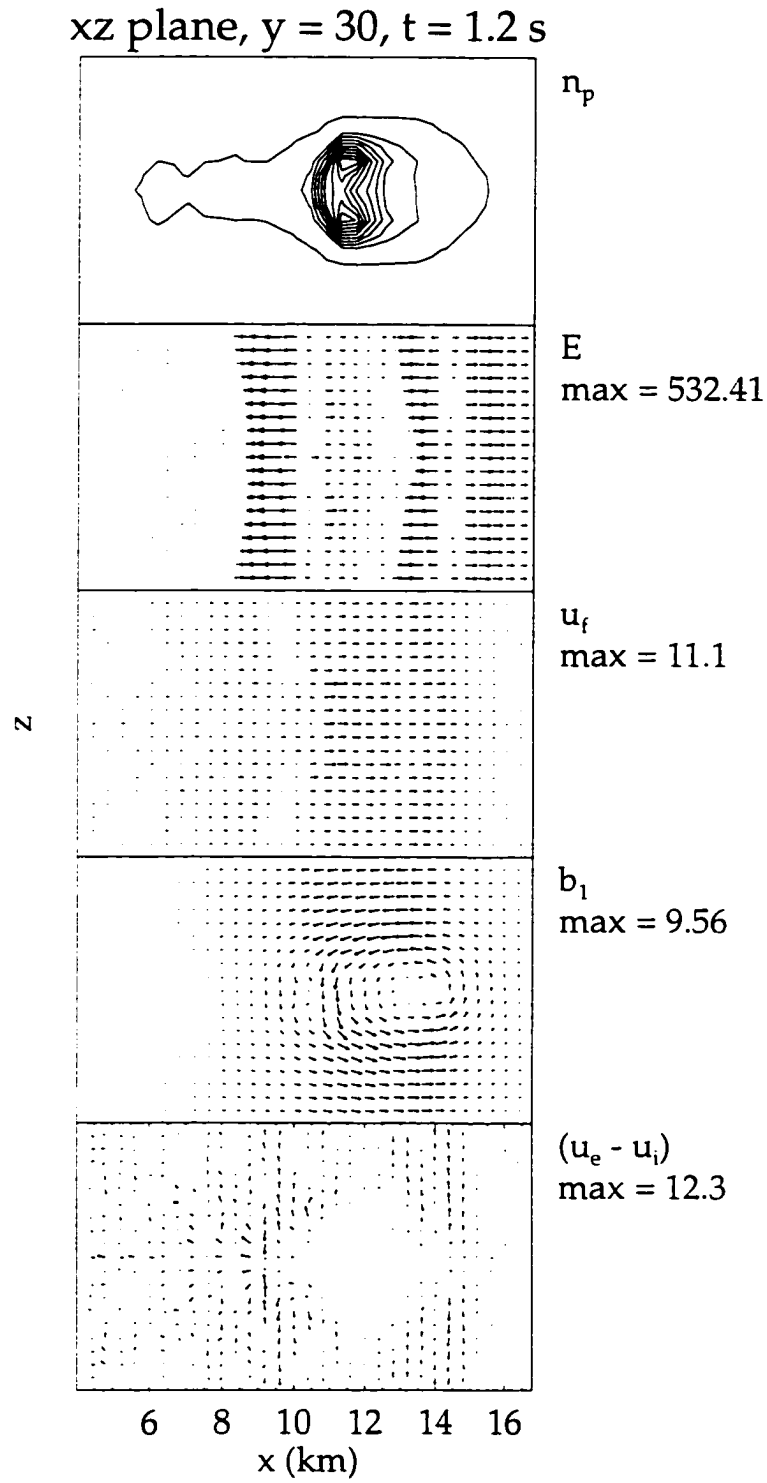


Figure 5.14: Field and fluid quantities in the xz plane at $y = 30$ and $t = 1.2$ s.

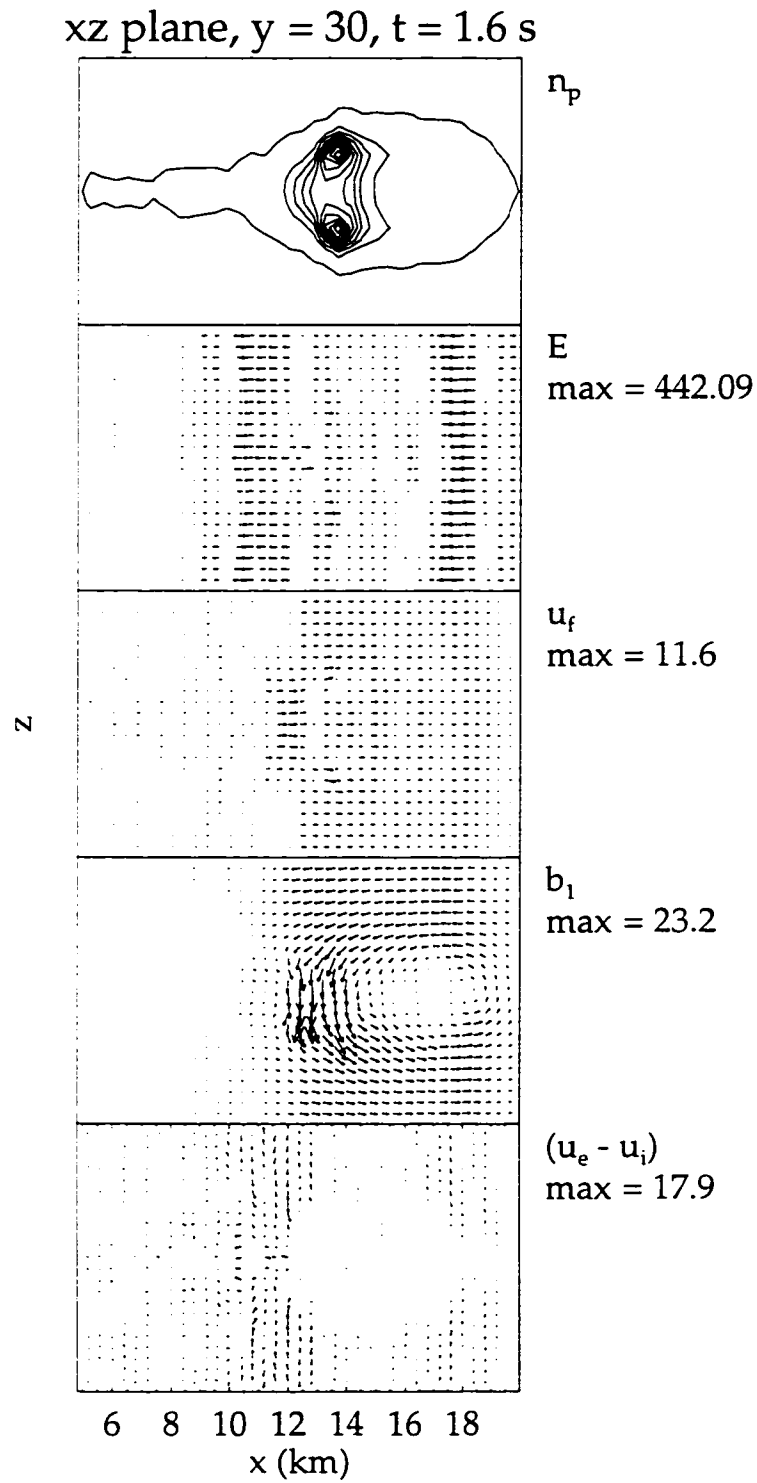


Figure 5.15: Field and fluid quantities in the xz plane at $y = 30$ and $t = 1.6$ s.

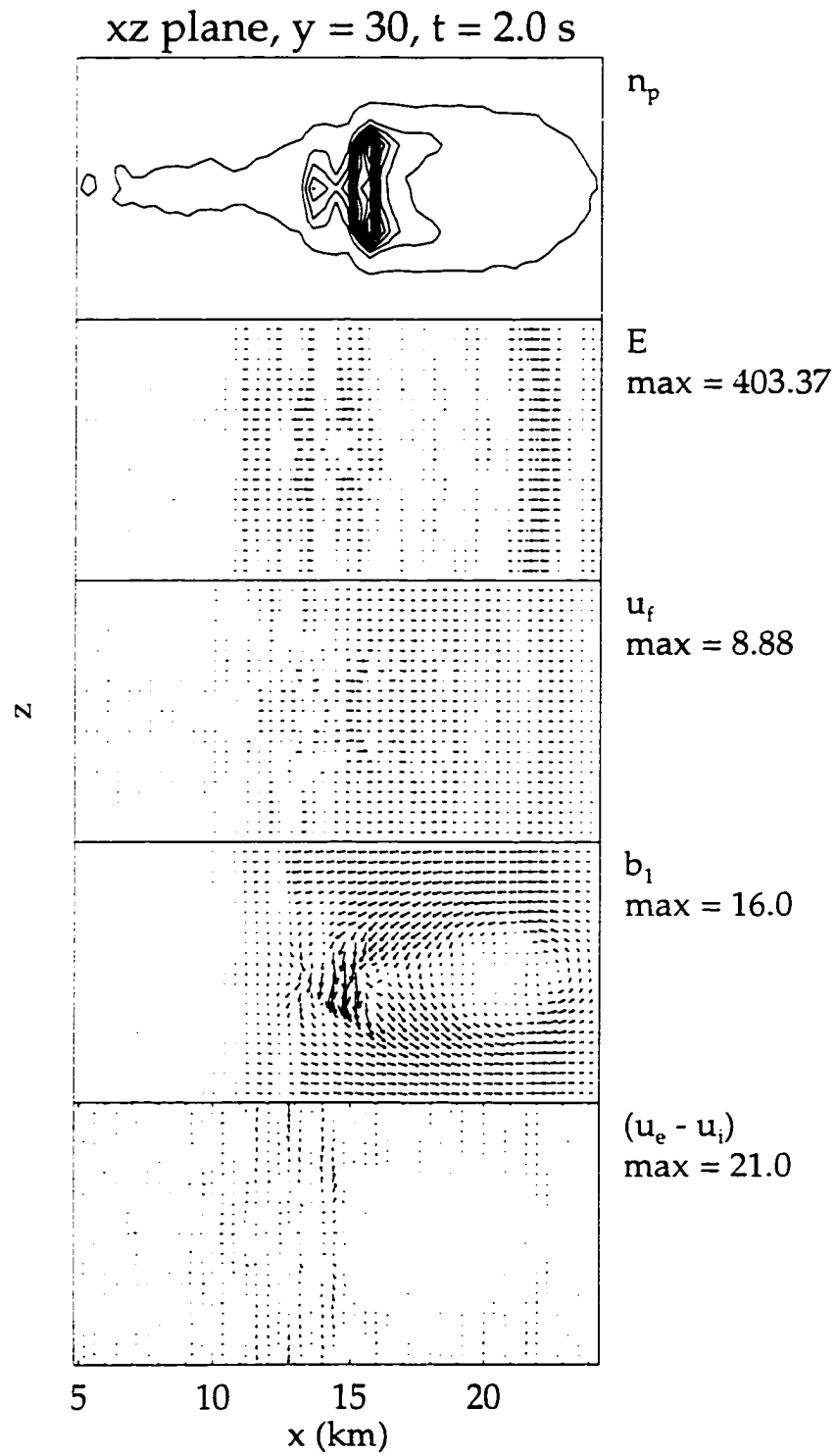


Figure 5.16: Field and fluid quantities in the xz plane at $y = 30$ and $t = 2.0$ s.

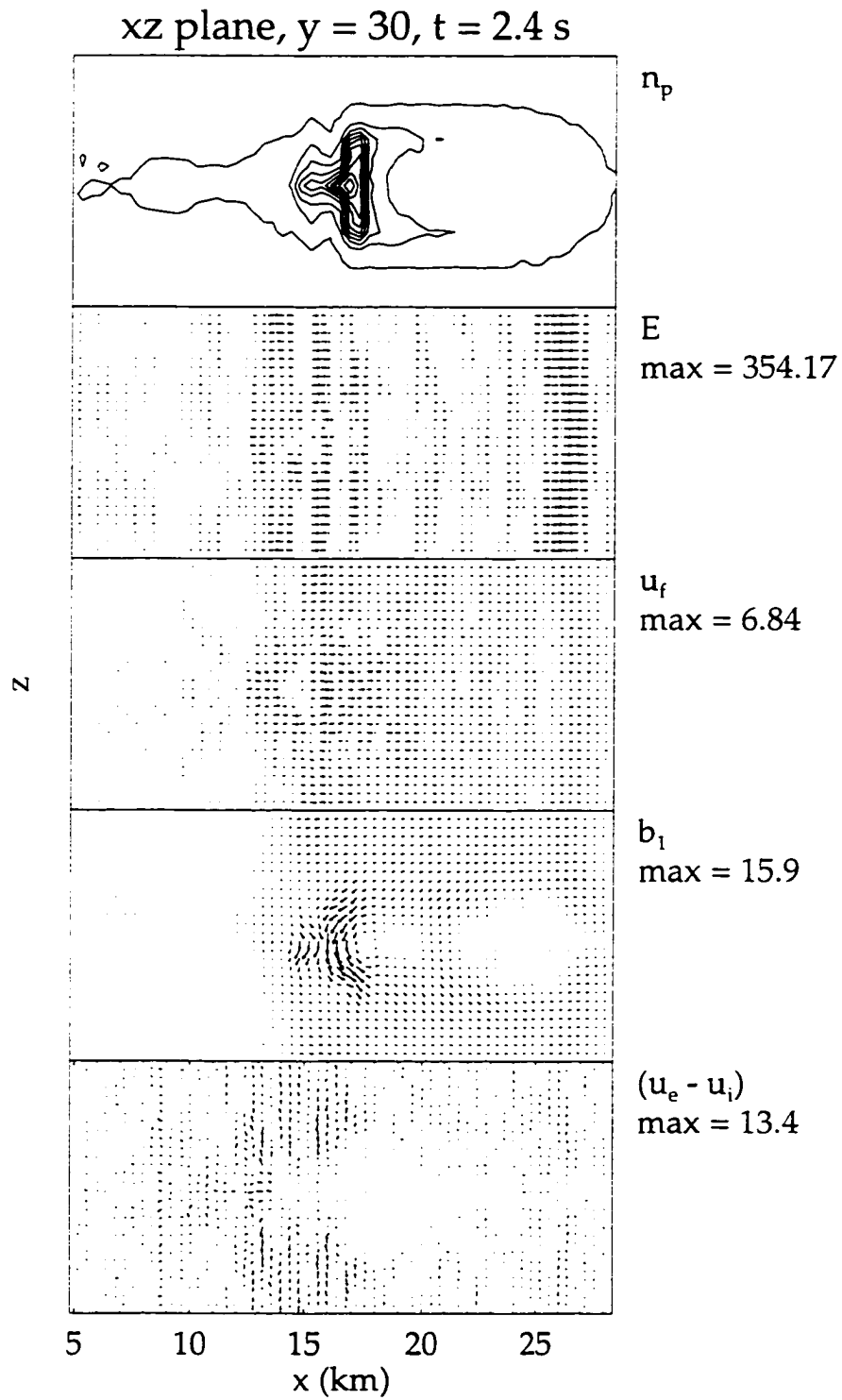


Figure 5.17: Field and fluid quantities in the xz plane at $y = 30$ and $t = 2.4$ s.

all of these figures. Since the ion cloud is moving in the x direction, the wave disturbance along z is a function of time and hence the structure of the perturbation to the ambient medium is called an Alfvén wing [*Wright and Southwood, 1987*]. Furthermore, perpendicular slices throughout the Alfvén wing will reveal the same vector field structures as seen in figures 5.6 through 5.11.

The perturbation magnetic field is asymmetric about the release midplane such that the components of \mathbf{B}_1 of the upward propagating wave have the opposite sign of the downward propagating wave as seen in figures 5.18 and 5.19. This magnetic field configuration carries the parallel currents shown in figure 5.20. This is also consistent with the frozen-in condition for the particles and the magnetic field. Figure 5.21 shows the magnetic field topology where much of the ambient magnetic field has been dragged with the skidding ion core. From this point of view it is clear that skidding of the ion core is limited by a strong magnetic tension force.

The polarization electric field is mapped symmetrically up and down the magnetic field by the Alfvén waves as seen in figures 5.22 and 5.23. Consistent with these electric fields is the ambient fluid flow shown in figures 5.24 and 5.25. Here we see that the y component of the fluid flow changes sign so that the total momentum in the y direction is zero. Thus, $(u_f)_x$ carries the momentum away from the ion cloud and the total momentum of the system is conserved (Appendix B).

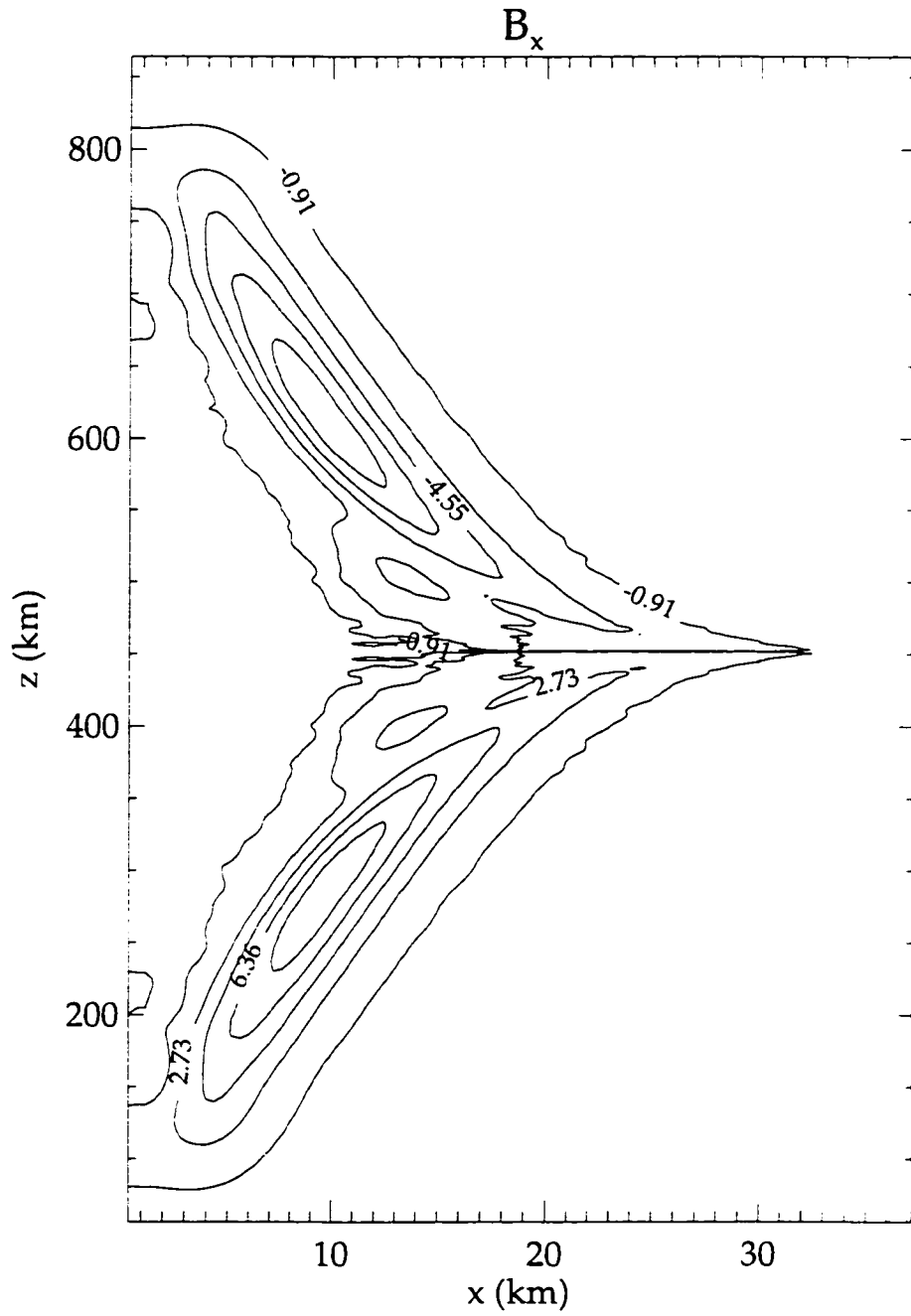


Figure 5.18: B_x contours in the xz plane at $y = 32$ and $t = 2.6$ s.

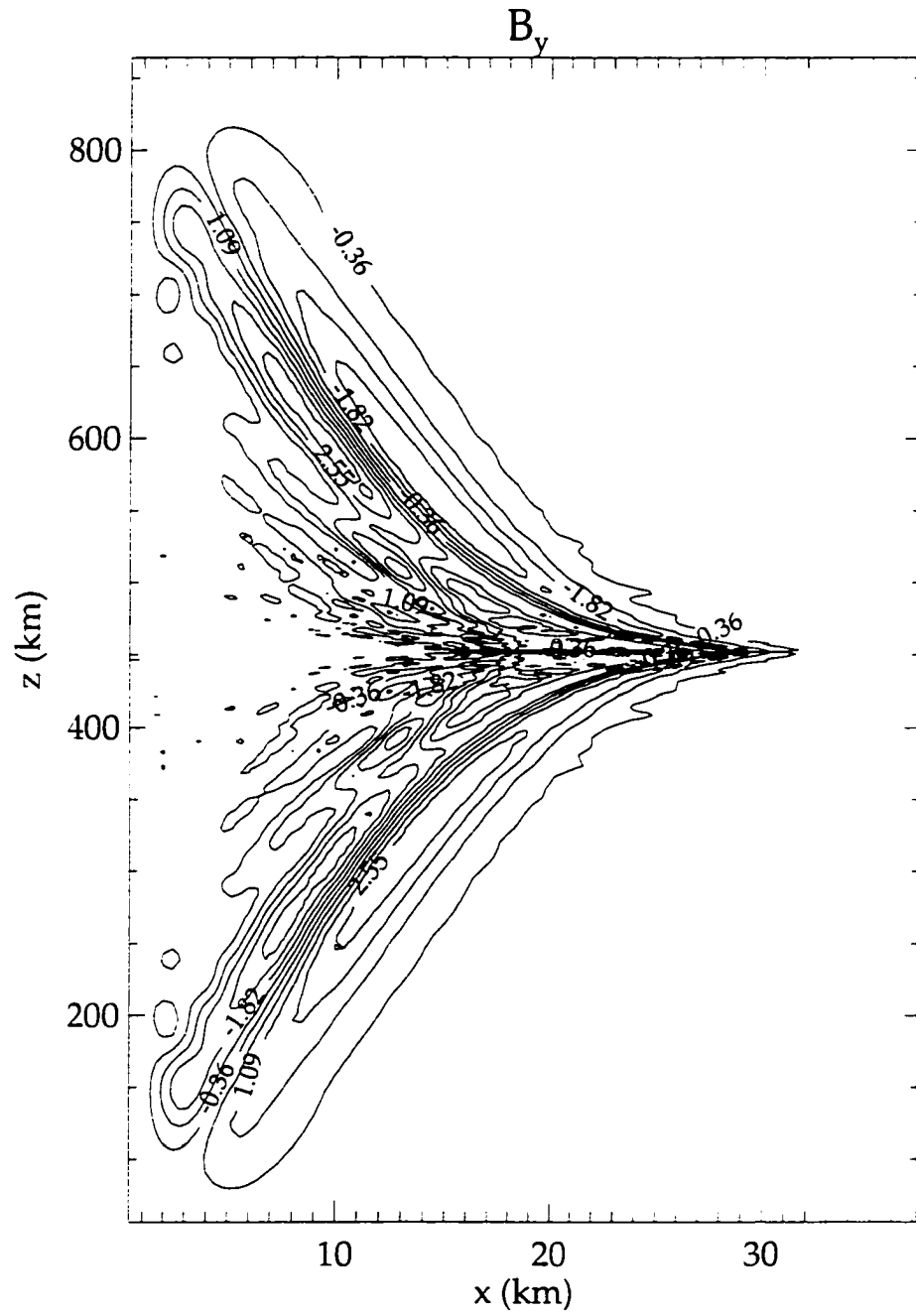


Figure 5.19: B_y contours in the xz plane at $y = 35$ and $t = 2.6$ s.

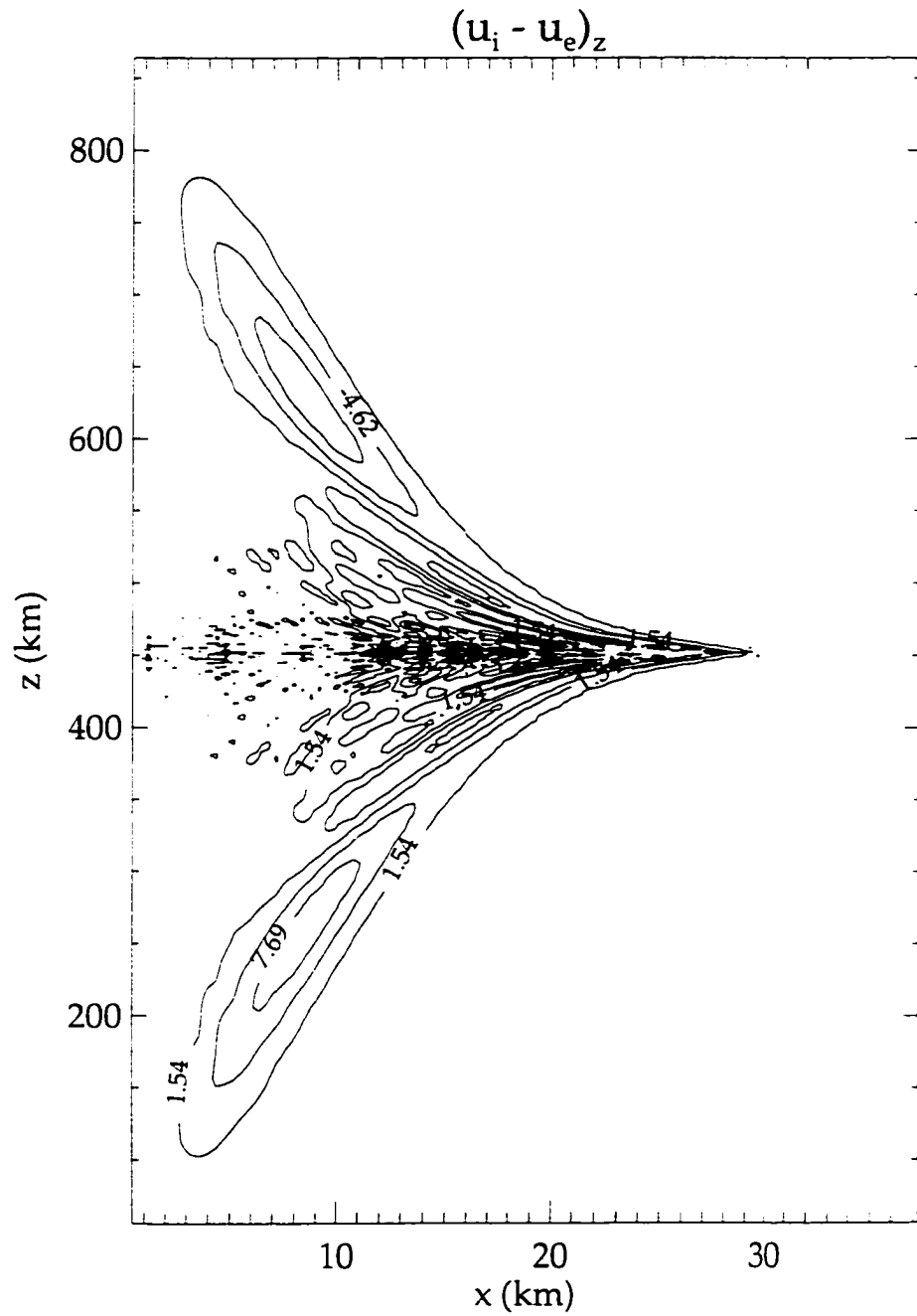


Figure 5.20: $(u_i - u_e)_z$ contours in the xz plane at $y = 32$ and $t = 2.6$ s.

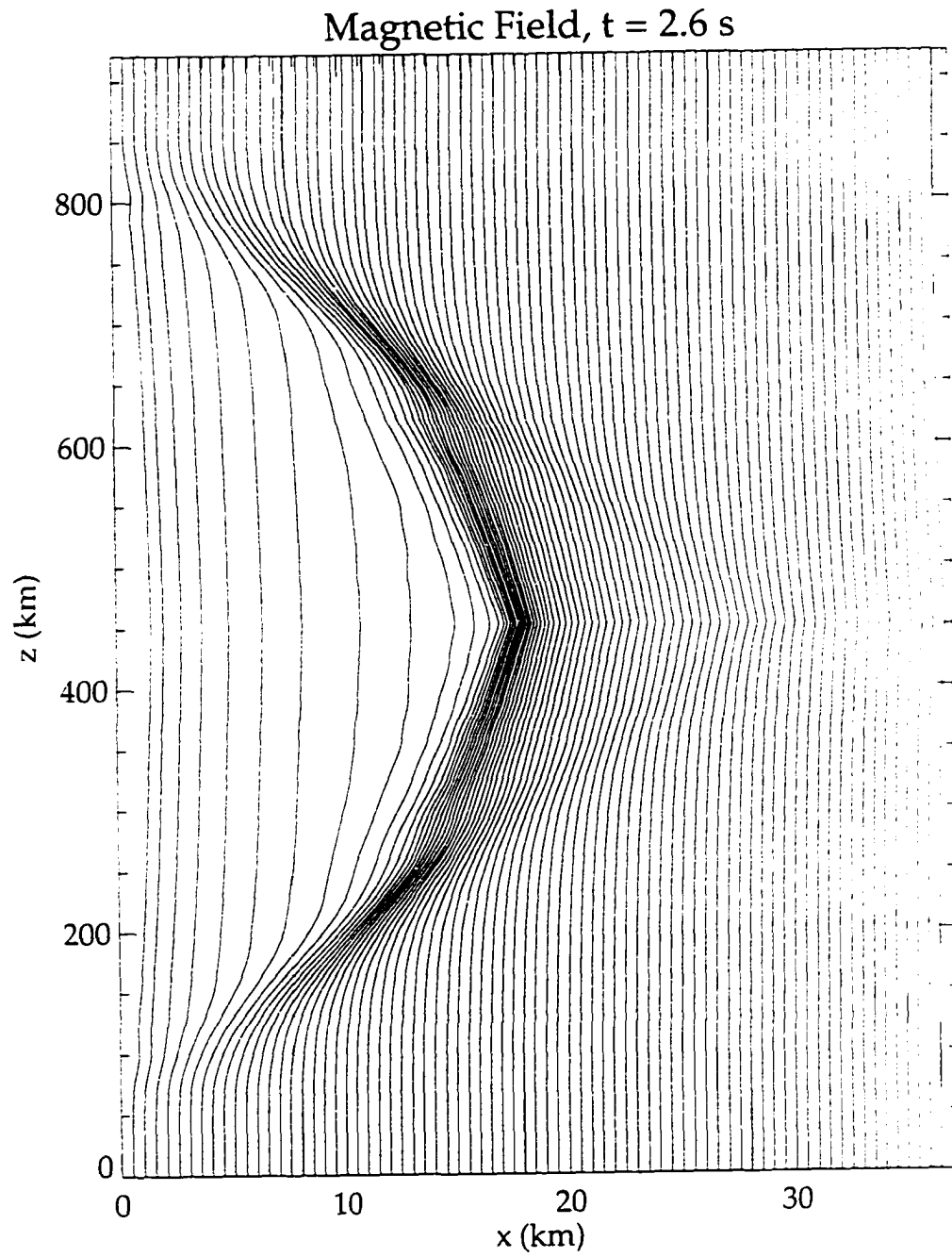


Figure 5.21: Magnetic Field topology in the xz plane at $y = 32$ and $t = 2.6$ s.

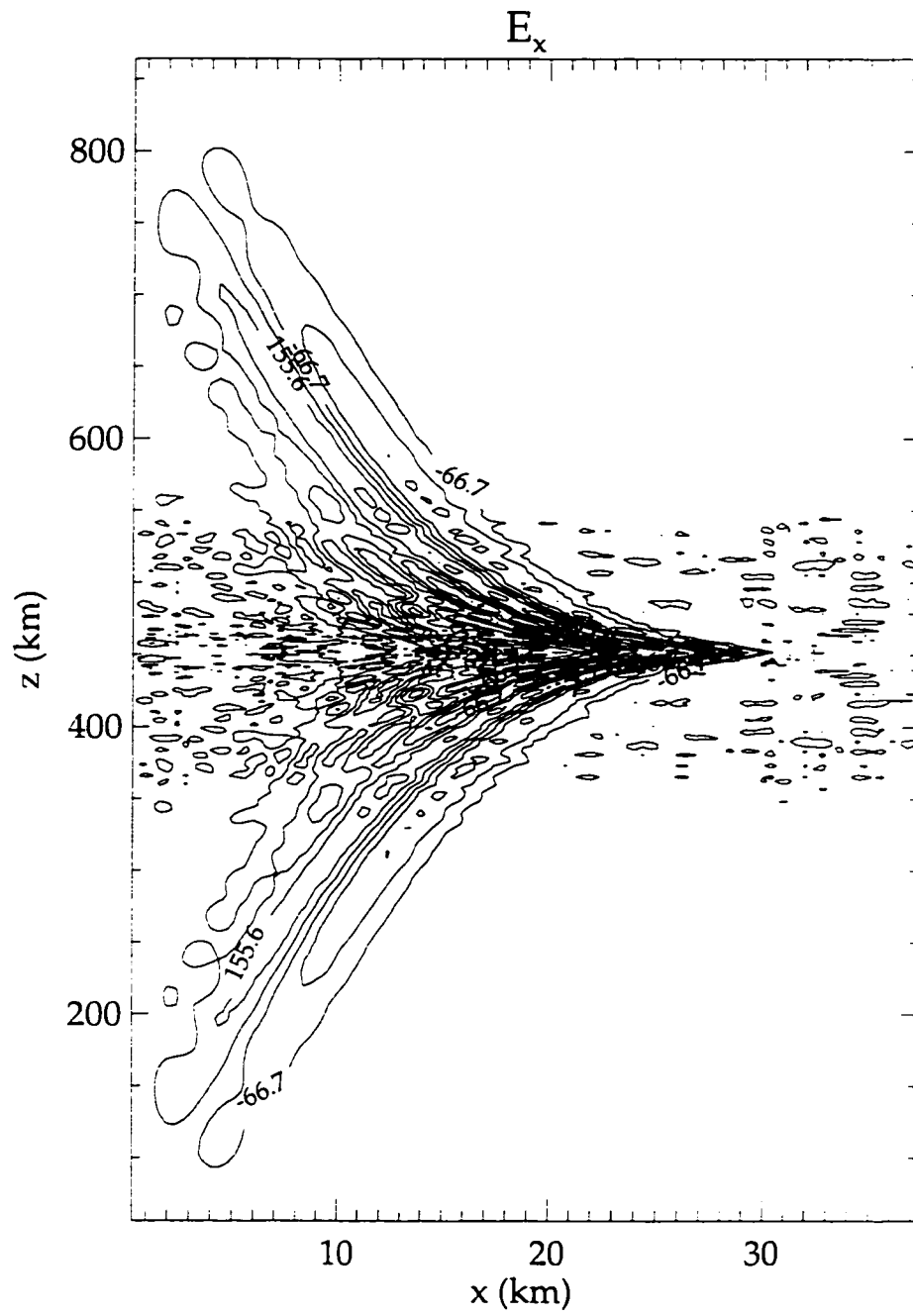


Figure 5.22: E_x contours in the xz plane at $y = 32$ and $t = 2.6$ s.

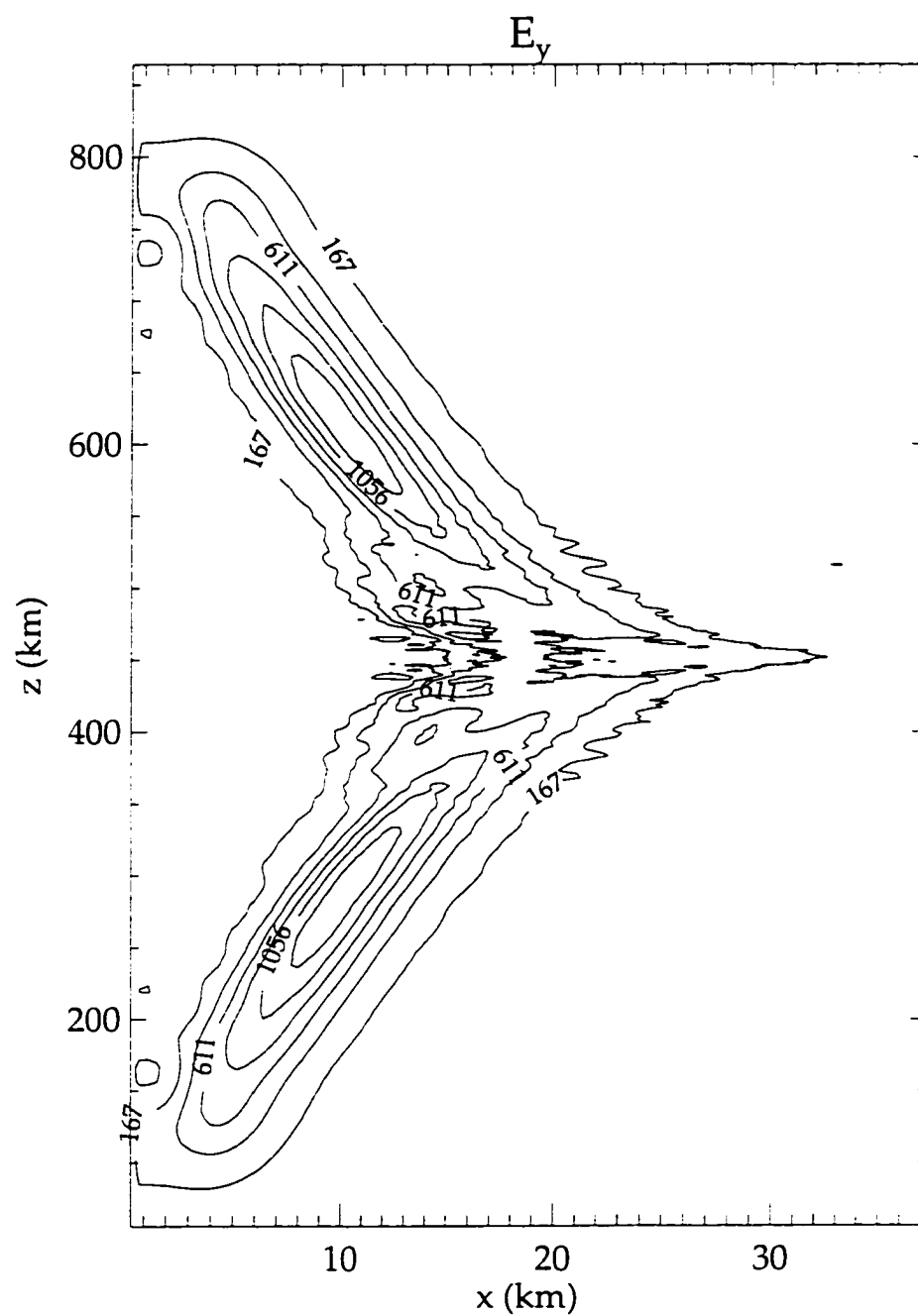


Figure 5.23: E_y contours in the xz plane at $y = 32$ and $t = 2.6$ s.

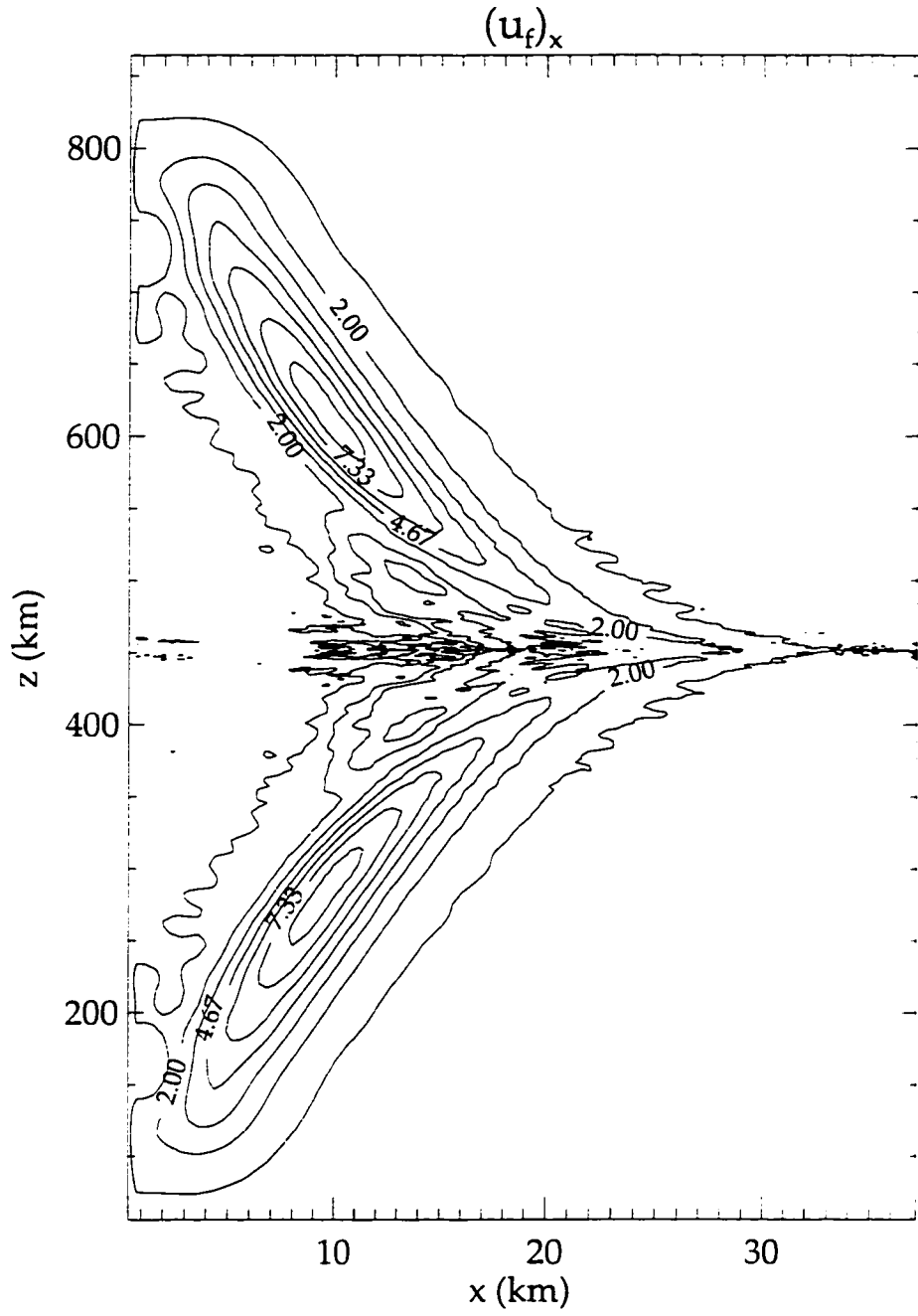


Figure 5.24: $u_{f,x}$ contours in the xz plane at $y = 32$ and $t = 2.6$ s.

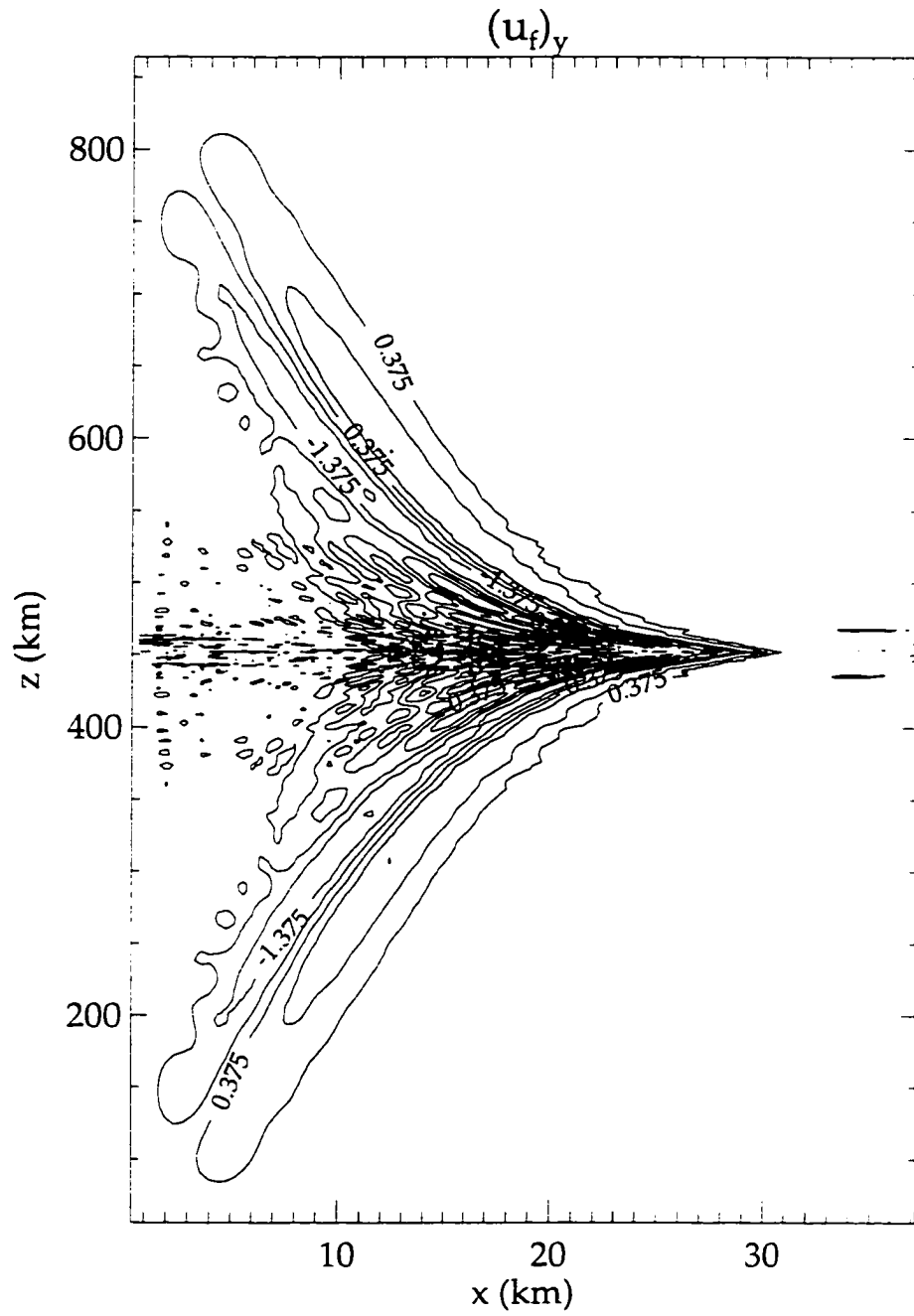


Figure 5.25: u_{f_y} contours in the xz plane at $y = 32$ and $t = 2.6$ s.

5.3 G1 and G11A Releases

Simulation runs #2 to #5 modeled the smaller G1 and G11A releases. The second run was used to compare skidding distances with the large G9 simulation. The third and fourth runs compare the effects of a reduced ambient density and collisional processes on skidding distances, while the fifth run examines the effects of electron pressure on the ion cloud morphology. Again, only the results are presented here. The discussion will follow in Chapter 6.

Small release, #2

Figure 5.26 summarizes the evolution of a small release ion distribution along x . The distance from the release point to the peak core density is only 6 km as compared to roughly 16 km in the large G9 simulation. The same ion cloud structures and field topology was present, but on a smaller scale since the skidding core was quickly stopped.

Sensitivity to a reduced ambient density, #3

The third run used an ambient density of $5 \times 10^{11} \text{ m}^{-3}$. This is a factor of 2 smaller than the previous runs which used $10 \times 10^{11} \text{ m}^{-3}$. The ion cloud profile is summarized in figure 5.27. The peak ion density is at roughly 7 km from the release point.

Charge exchange and collisional processes, #4

The effects of charge exchange and Ba-Ba⁺ collisions on the skidding distance were investigated using a Monte Carlo collision algorithm using the ion densities and the neutral densities given by 1.3. The charge exchange cross section used was $1 \times 10^{-16} \text{ m}^2$ and the Ba-Ba⁺ momentum exchange cross section was $5.9 \times 10^{-17} \text{ m}^2$. For the purpose of obtaining an upper limit estimate of the effects of billiard collisions on the skidding distance we increased the neutral density by a factor of 5. The thermite release mixture consists of 43% barium, 1.7% strontium, 38.2% titanium and 17.1% boron by weight. Recall that only 40% of the barium actually vaporizes leaving a large cloud a barium particulates. Likewise, the titanium-boron mixture also exists in some particulate cloud form. In the limiting case (and

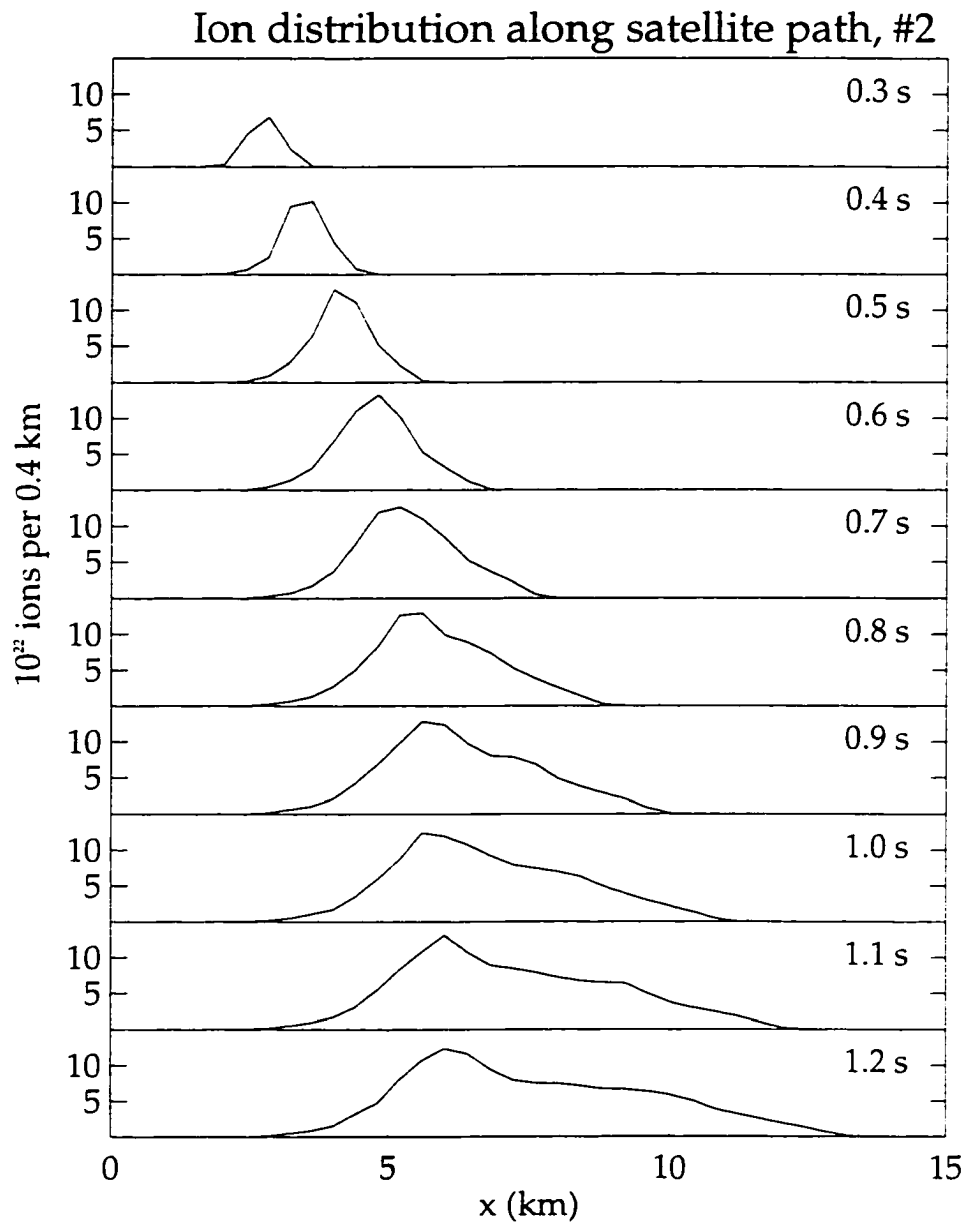


Figure 5.26: Small release ion distribution along the satellite path.

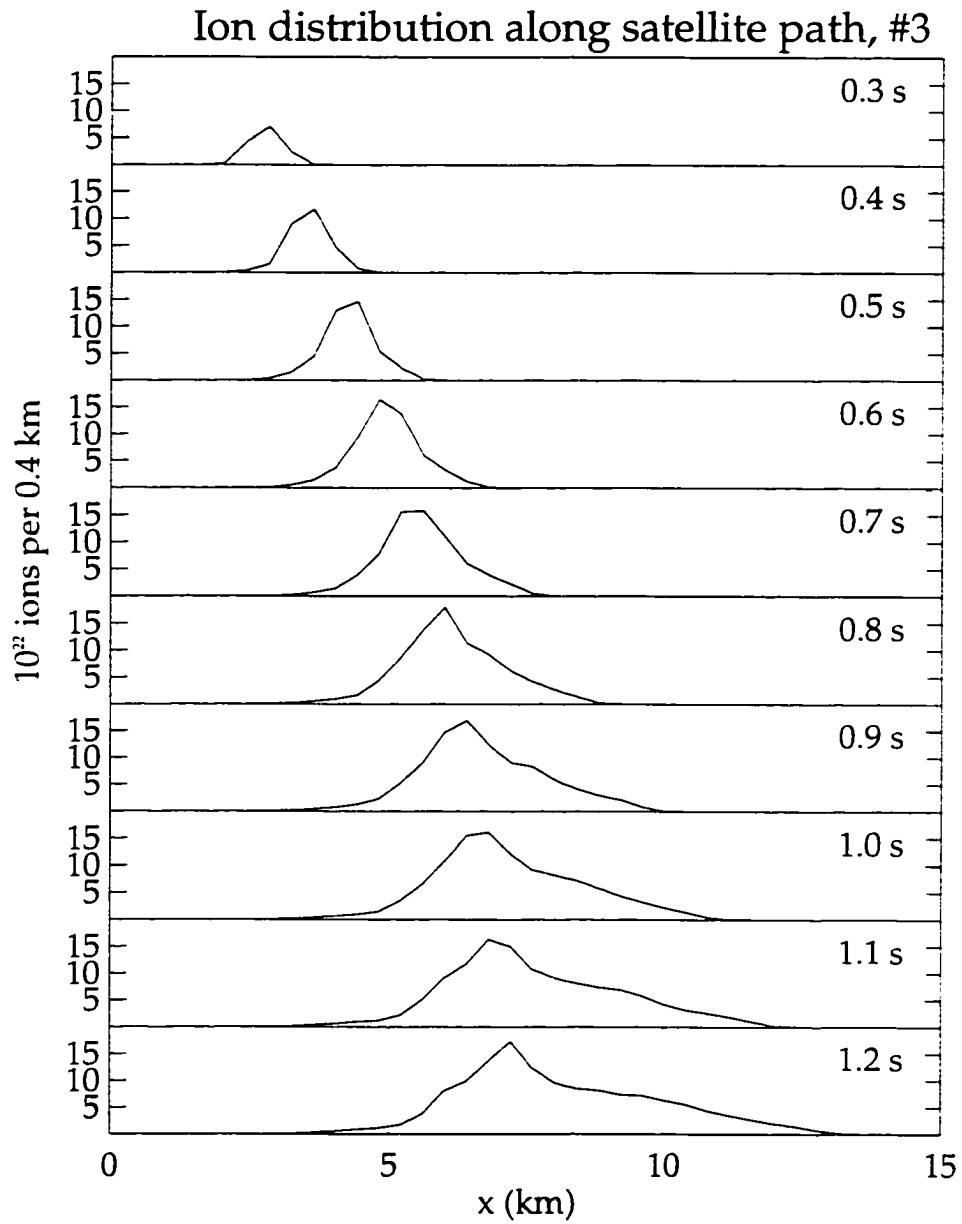


Figure 5.27: Small release ion distribution along the satellite path using $n_e = 5 \times 10^{11} \text{ (m}^{-3}\text{)}$, or half of the ambient density of the run shown in figure 5.26.

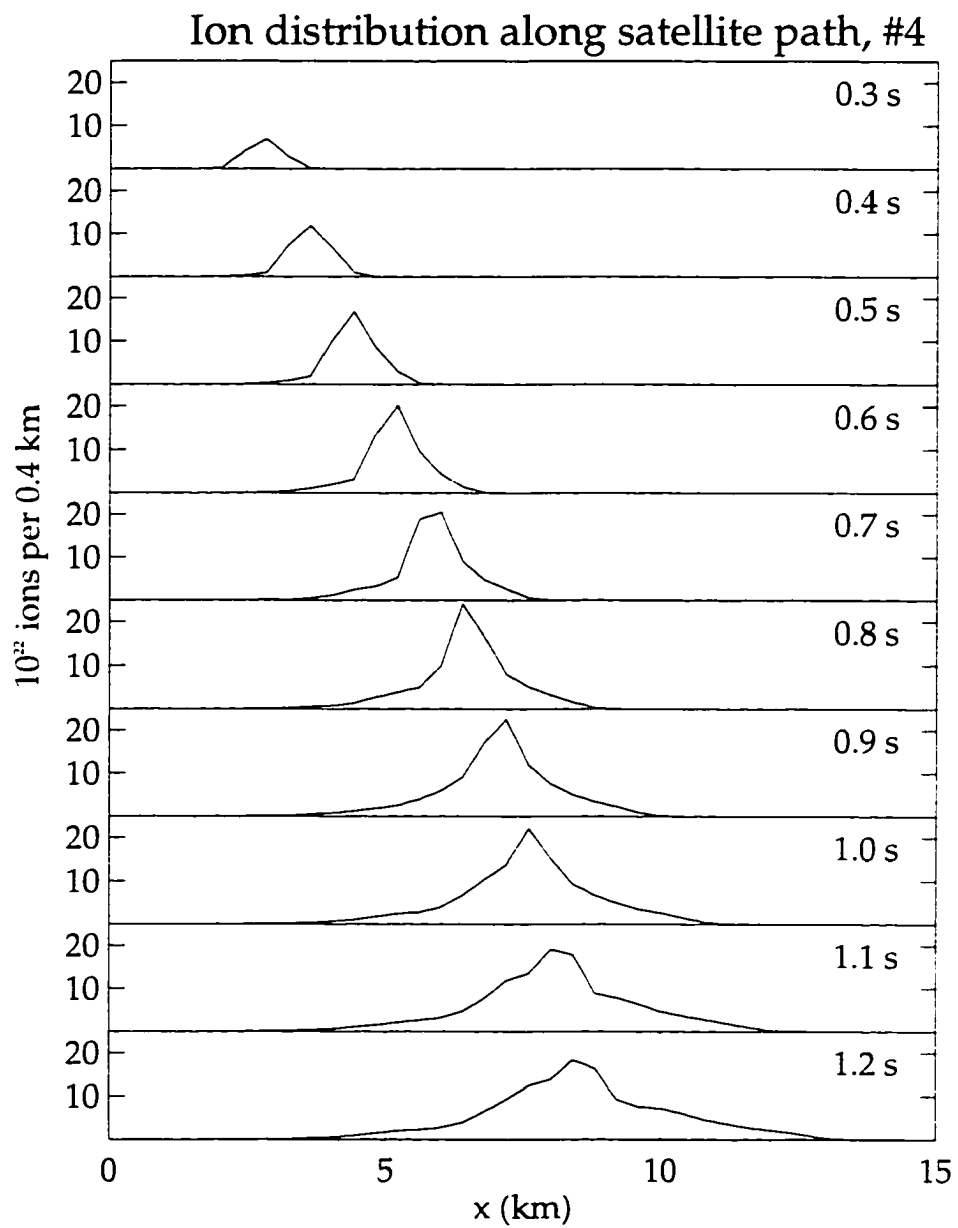


Figure 5.28: Small release ion distribution along the satellite path with Ba-Ba⁺ charge exchange and billiard collisions.

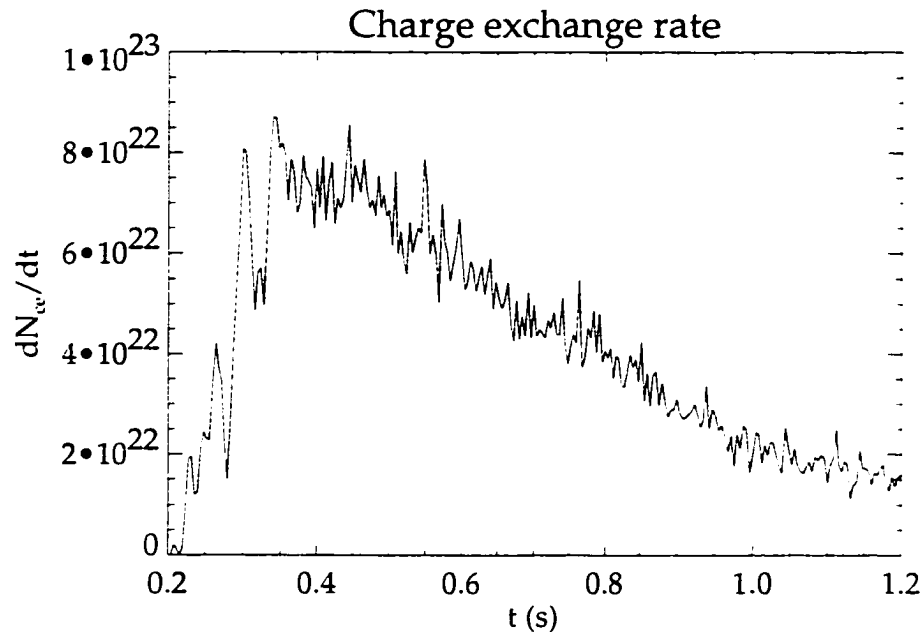


Figure 5.29: Small release charge exchange rates using $1 \times$ neutral densities.

presumably unlikely case) these particulates will have a diameter of a Ba atom. Hence we considered all of the release mass as barium neutrals, or roughly 5 times the actual barium vapor.

Figure 5.28 shows the ion cloud profile for this simulation. Now the distance to the peak ion density is about 8.5 km from the release point. The ion particle energy was boosted by roughly 30% by these charge exchange and collisional interactions. Figures 5.29 and 5.30 show the charge exchange rates and the billiard collision rates respectively. The total number of charge exchange interactions was roughly 1.5% of the released material. The collision rates start at zero and increase to a maximum as the core slows and interacts with the densest part of the neutral cloud.

Electron pressure, #5

The electron pressure term was included to simulate the effects of electron heating on the ion cloud morphology. Heating mechanisms include, in particular, the CIV effect which is driven by counter-streaming ions and electrons in the ion particle cloud. Hence the

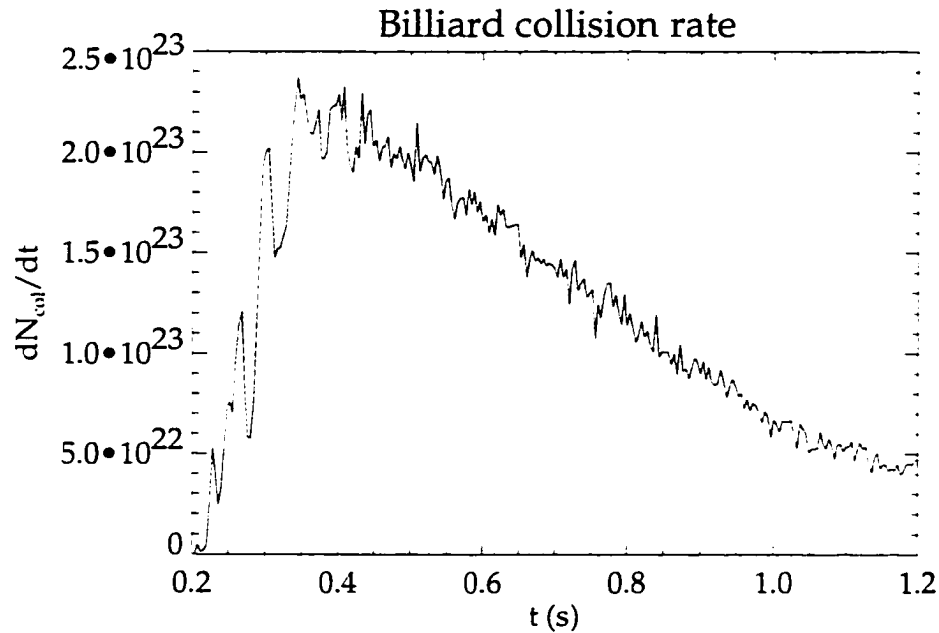


Figure 5.30: Billiard collision rates using $5 \times$ neutral densities.

electron temperatures were elevated only in the vicinity of the ion cloud by weighting the temperature with the ratio of particle density to total density, or $T_e n_p / n$. The pressure gradient arises from contributions from the temperature gradient and the density gradient. We used several different values for T_e , however, only the results for $T_e = 10^5$ K are presented here. For values of 10^4 K or smaller the pressure term had a negligible effect on the ion cloud morphology. Figure 5.31 shows a cross section of the ion cloud in the xz plane at $t = 1.2$ s. The release end of the cloud is elongated along the magnetic field in a manner similar to the observations, but on a smaller spatial scale. The maximum parallel electric field that was generated at $T_e = 10^5$ K was roughly 200 km/s^2 at $t = 0.6$ s. For the sake of comparison, see figure 5.4 and note that the pressure gradient tends to remove the density inhomogeneities in the ion core.

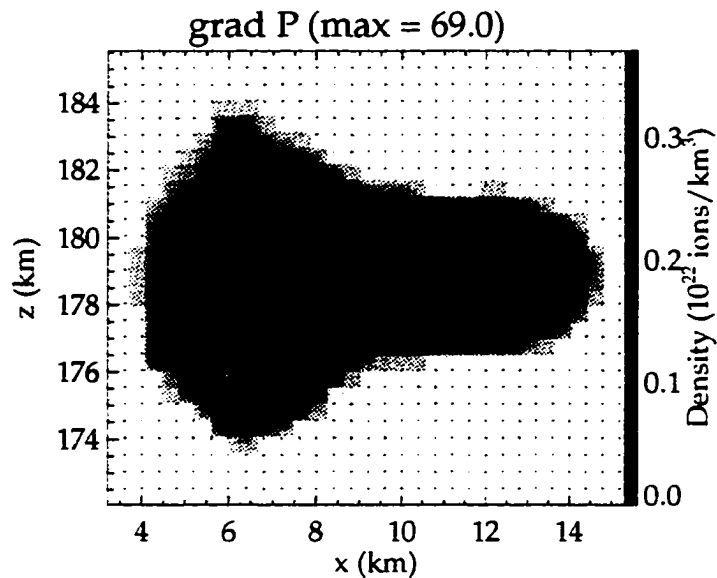


Figure 5.31: Ion cloud in the xz plane at $y = 13$ and $t = 1.2$ s with electron pressure. The electron temperature is 1×10^5 K. Figure 5.3 shows an analogous cross section from the G9 simulation without electron pressure. Notice that the pressure term smooths the density inhomogeneities associated with the core.

5.4 Summary

The main findings of the hybrid code simulation of the CRRES releases are summarized below:

- A skidding ion core forms from the initially dense ion cloud.
- The perpendicular extent of the core is limited to a few kilometers. The core expands freely in the parallel direction forming a cylindrical structure. During this parallel expansion, the core splits into two parts.
- The ions trailing the core begin to form a herringbone structure.
- The skidding distance of the core is limited to roughly 16 km for a large release and 6 km for a small release.

- Reducing the ambient density by a factor of 2 increases the skidding distance of the core from 6 km to 7 km.
- Ba-Ba⁺ charge exchange and billiard collisions extend the skidding distance from 6 km to an upper limit of 8.5 km.
- Electron temperatures exceeding 1×10^5 K are sufficient to elongate the ion cloud and smooth density inhomogeneities along the magnetic field.

Chapter 6

Discussion and Conclusions

The hybrid code simulation of the CRRES releases has added substantial insight into the coupling of an ionizing neutral cloud to an ambient magnetized plasma. Numerical experiments, performed using a variety of release parameters, have demonstrated that many of the observed morphological characteristics of the barium ion clouds are consistent with the formation of a dense skidding ion core. However, the simulated ion cloud profiles show a substantially shorter skidding distance of the ion core than the observations show, thus indicating that one or more key processes are still missing. In this chapter we will attempt to reconcile the differences between the simulated and observed ion cloud profiles and we will show that the skidding core is the basis for the observed ion cloud structures.

6.1 Cloud-Ionosphere Coupling

The hybrid code simulation shows that the ion core should have skidded for distances of 6 km and 16 km for the small and large releases respectively. The skidding distance is defined as the distance from the release point to the peak ion density in the x direction. This differs substantially from the observations which show skidding distances of at least 60 km and 100 km for the small and large releases respectively. This represents a difference of at least one order of magnitude in the case of the small release and at least a factor of ~ 6 for the large release.

In an attempt to reconcile these differences we first examined the sensitivity of the

skidding distance to the ambient plasma density. Figures 5.26 and 5.27 show the results of the numerical experiment where the ambient density was reduced by a factor of two from $10 \times 10^{11} \text{ m}^{-3}$ to $5 \times 10^{11} \text{ m}^{-3}$. This increased the skidding distance from 6 km to ~ 7 km. Since the momentum transfer rate is proportional to the Alfvén speed which increases as $1/\sqrt{n_e}$, one would expect the skidding distance to increase because the total ambient mass that is coupled to the barium cloud via the Alfvén waves decreases. In a physical ionosphere the plasma densities will decrease both up the down the magnetic field line from the release. However, for a typical ionospheric density profile, the Alfvén waves would have to travel at least 200 km (~ 1 s) from the release region before the ambient densities are reduced by one order of magnitude. Already in this transit time there is enough ambient mass to stop the skidding core according the hybrid code simulation results. We therefore conclude that *reductions in ambient density cannot explain the observed skidding distances.*

Conducting boundaries also present a severe restriction to the skidding distance. If the Alfvén waves reflect from a conducting boundary then the resulting increased magnetic tension will further decelerate the ion core. Physically, when the wave is reflected the fluid flow reverses direction but the perturbation magnetic field increases in magnitude. Since the magnetic field is fixed at the boundary surface, the increased perturbed field creates the increased magnetic tension. Alternatively, the conducting boundaries will short out the polarization electric fields and stop the skidding. Figure 5.21 illustrates the distortion of the magnetic field caused by the ion cloud and shows that the simulated barium cloud was isolated from breaking effects of the conducting boundaries. In the actual release scenario we expect that the Alfvén wave will be reflected from the conducting E-region of the ionosphere within the first 2 seconds after release. Furthermore, reflections can be expected if the Alfvén waves propagate into regions of higher density which may have been the case in the CRRES releases. (Recall that the CRRES release occurred at dawn and thus the ionospheric electron density profile is unknown as solar photoionization modified the altitude dependent density profile.) *Therefore, it appears that the core managed the observed skidding distances despite the breaking effects of the conducting E-region and wave reflections due to ambient plasma density gradients.*

According to the hybrid code simulation results, momentum is rapidly transferred from

the barium cloud to the ambient plasma. Before considering plasma processes that may limit the momentum transfer rate, we will first examine sources of momentum from the neutral cloud. As the neutral cloud sweeps past the ions, momentum is added to the ion population via direct billiard collisions and charge exchange interactions. The momentum boost provided by charge exchange occurs indirectly when neutrals with their original momentum are added to the ion population and ions that have already lost momentum are removed to the neutral population. Both interactions were included for the numerical experiment shown in figure 5.28. The neutral densities were increased (5x) to represent the upper limit for billiard interactions with not only barium neutrals, but also the particulate cloud composed of unvaporized barium, boron and titanium. The interaction rates for both processes are shown in figures 5.29 and 5.30. The billiard interactions represented the primary ($\sim 30\%$) momentum boost, but still the overall skidding distance of the core is not significantly affected. It therefore appears that *the momentum coupling must be limited by a physical mechanism that is not included in the hybrid code.*

From considerations of momentum conservation, the fundamental requirement for extended skidding would be a process to damp the Alfvén waves. This would clearly limit the momentum transfer to the ambient plasma. Since the Alfvén waves propagate a parallel current, wave damping is equivalent to a current limiting process which would consequently invoke a magnetic-field-aligned electric field. Figure 6.1 illustrates this idea. The question is, how are the parallel currents limited in a barium release?

The topic of current limiting processes in Alfvén wings has been considered by *Brenning* [1995]. The ion cloud will draw a current in response to the cloud's polarization. The upper limit to this current is the electron saturation current which is simply the thermal electron velocity of the ionosphere, $v_{e,th}$. *Brenning* [1995] argues that if the cloud diameter is sufficiently small (i.e. 0.5 km) then the Alfvén waves generated by the cloud would require currents that exceed the saturation current. As a consequence, some process must necessarily limit the field-aligned drift velocity of the electrons.

The hybrid code simulations showed that the parallel currents are limited to sheath regions at the edges of the ion cloud and are filamentary in structure. We experimented with several grid resolutions and found that the parallel electron flow velocities exceeded the ambient saturation current for cell sizes of 100 m or less. The random thermal electron

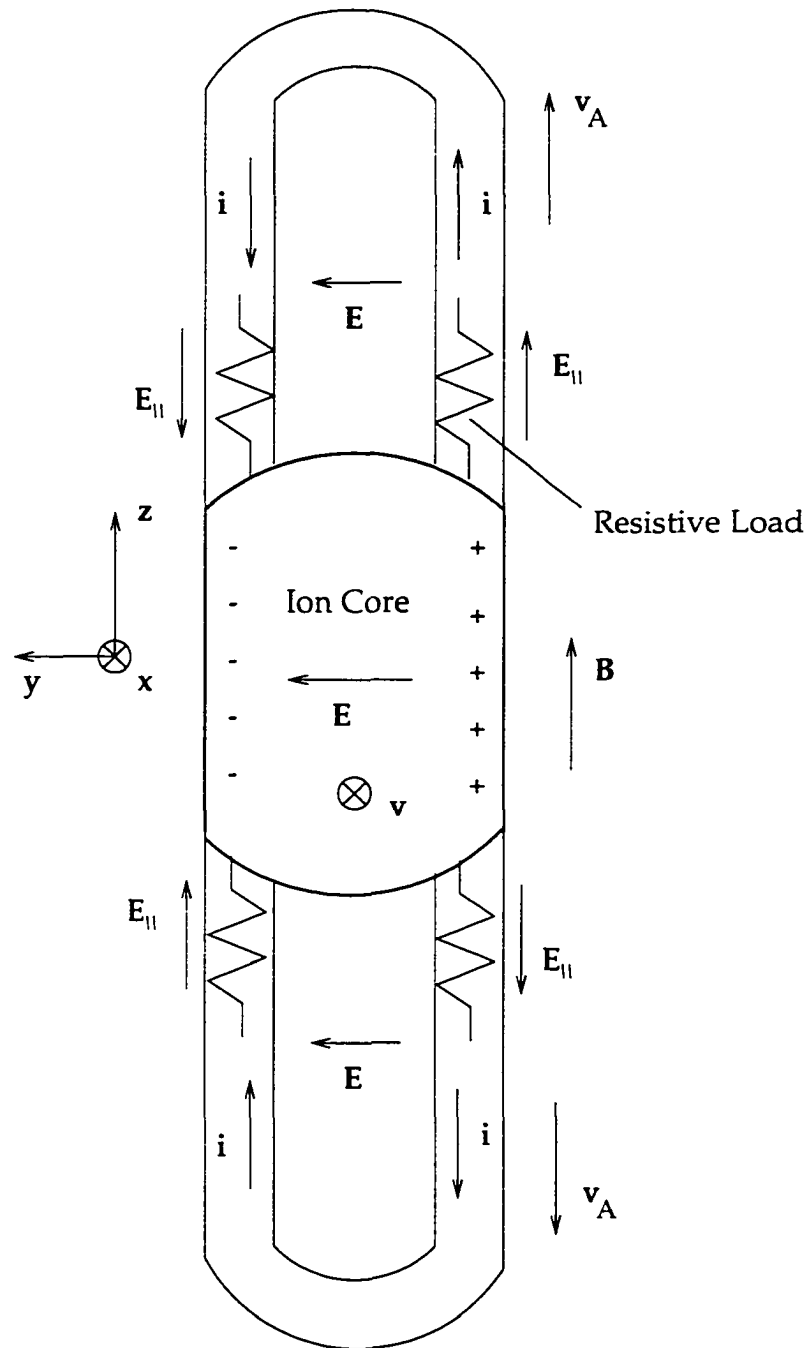


Figure 6.1: Alfvén wave damping. An illustration of the current system that is propagated by the Alfvén wave. The observed skidding of the ion core requires a mechanism to damp the Alfvén wave. This damping mechanism is represented by the resistive load in the current sheaths.

drift velocity, $V_D \sim (\mathbf{u}_i - \mathbf{u}_e)_z$, associated with the saturation current is roughly 180 km/s assuming an ionospheric temperature of 1000 K. Given that the core remains a relatively small spatial structure in the perpendicular direction, it is possible that the current limiting processes described by *Brenning* [1995] could continue for a significant period of time.

Another consequence of the limited perpendicular extent of the core and its associated current filaments are inertial Alfvén waves. When the perpendicular wavelength is smaller than the ion gyroradius ($\rho_i = 500$ m) the ions, unlike the electrons, cannot follow the magnetic line of force. Charge separations result and the wave is then coupled to the electrostatic mode [*Hasegawa and Uberoi*, 1982]. The dispersion relationship for the kinetic Alfvén wave is

$$\omega^2 = k_z^2 V_A^2 \left[1 + k_x^2 \rho_i^2 \left(\frac{3}{4} + \frac{T_e}{T_i} \right) \right] \quad (6.1)$$

where T_e and T_i are the electron and ion temperatures. If the plasma is relatively cold such that $v_{e,th} < V_A$ then electron inertia becomes important and the dispersion relationship for the inertial Alfvén wave is

$$\omega^2 = \frac{k_z^2 V_A^2}{1 + k_x^2 \lambda_e^2} \quad (6.2)$$

where λ_e is the electron inertial length (see Appendix C). As the perpendicular wavelength approaches the electron inertial length then the second term in the denominator becomes important. An expression for the polarization of the inertial wave is

$$\frac{E_z}{E_x} = \frac{c^2 \omega^2}{V_A^2 \omega_{pe}^2} \tan \theta \quad (6.3)$$

which shows that for $\theta > 0$, E_z will always be nonzero. Therefore the Alfvén modes alone can produce the required parallel electric fields that are necessary for current limitation provided that the perpendicular extent of the current filaments approaches the electron inertial length (~ 5 -10 m at release altitude). As the hybrid code simulation suggests, the perpendicular extent of the current filaments approach λ_e and hence inertial Alfvén waves are a likely candidate for the parallel electric fields.

Lysak and Carlson [1981] studied the effect of microscopic turbulence on the inertial Alfvén wave. They found that in the presence of an effective collision frequency term in the equation describing the inertial Alfvén wave, a parallel electric field was generated. In the limiting case, where the effective collision frequency is greater than the Alfvén frequency, the parallel potential drop equaled the perpendicular potential.

Other current limiting mechanisms discussed in the literature include plasma instabilities, double layer formation, and magnetic reconnection which all involve parallel electric fields. The Buneman instability is destabilized if the parallel electron drift velocity, V_D , is larger than the electron thermal speed [Buneman, 1959; Lysak and Carlson, 1981]. Iizuka et al. [1979] and Raadu [1988] claim that in narrow structures, such as the current sheaths found in our simulation, the Buneman instability may lead to the formation of double layer structures which are electrostatic structures contained within a current carrying plasma that sustain a net potential difference. However, Maggs [1976] argues that Buneman and Langmuir instabilities are not likely to occur in narrow channels because these high frequency waves ($\omega \sim \Omega_e$) propagating near the resonance cone angle will have a group velocity perpendicular to the magnetic field. Also, Kindel and Kennel [1971] showed that the current-driven ion cyclotron instability will be excited when $V_D/v_i > 13T_i/T_e$ which generally involve drift velocities lower than $v_{e,th}$. Other plasma instabilities such as the lower-hybrid-drift instability and the ion-acoustic instability can provide the "anomalous resistivity" for generating the parallel electric fields that are necessary for magnetic reconnection [Birk and Otto, 1991]. Figure 5.21 shows that if the barium particles are truly frozen to the magnetic field, then substantial magnetic tension will result if the ion core manages to cross-field propagate over the observed distances. It is possible that magnetic reconnection processes occur which allow the ions to slip across the magnetic field. Figure 6.2 illustrates this process for the barium release where perturbed field lines (bold) reconnect with neighboring unperturbed field lines (Antonious Otto, personal communication, November 1997).

There is an abundance of observational evidence that supports the existence of parallel electric fields in chemical releases. First, the elongation of the ion cloud in the G1 releases shows that the ions were accelerated along the magnetic field line. Further evidence was provided by in situ measurements made by Brenning et al. [1991b] in the CRIT I and CRIT II CIV rocket experiments. CRIT I and II were shaped charge releases, injected at roughly 45° to the magnetic field and directed at the main instrumented payload. The velocities of the vapor beam ranged from 3.5 to 13.0 km/s. Parallel electric fields measured at the main payload ranged from 450 mV/m to 600 mV/m in the CRIT I release. (Recall that for the CRRES releases $v_{sat}B = 300$ mV/m.) Furthermore, Swenson [1992] reports the measurement

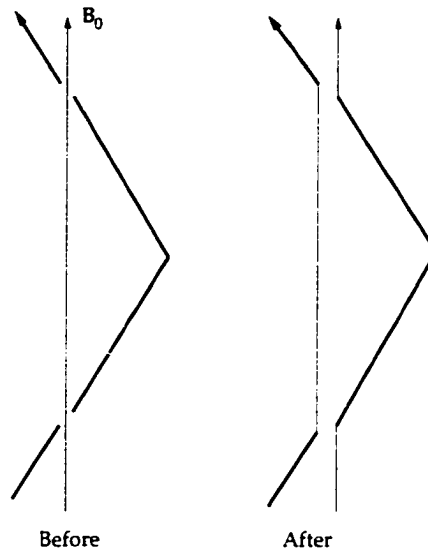


Figure 6.2: Magnetic reconnection. An illustration of the magnetic reconnection process. The x component of the magnetic field is antiparallel in the midplane of the ion cloud and it is across this boundary that reconnection occurs. In this illustration the bent field lines reconnect with their neighboring unperturbed field lines which are external to the ion cloud.

of 100 eV electrons at the CRIT II main payload with energy fluxes exceeding 5×10^{10} keV cm⁻² s⁻¹ ster⁻¹, indicative of the strong electric fields. These measurements were made within the first 0.2 s following the release and the perpendicular electric fields were directed back along the neutral stream. This is consistent with an ionization front at the leading edge of the cloud where the large-gyroradius ions simply outrun the magnetized electrons. *Brenning et al. [1991b]* proposed that these parallel electric fields existed because the barium stream demanded currents that exceeded the ambient thermal electron current as discussed above.

6.2 Neutral Disk

Charge exchange processes probably do not significantly alter the ion velocity distribution. Consistent with observations, the initial analysis of chapter 3 was based on the assumption that the skidding ion core moves with the neutral cloud during the first few seconds of the release. The calculated charge exchange rates agreed with neutral disk inventories

and with the time evolution of the neutral disk as measured by the initial appearance of the backjet. The hybrid code, on the other hand, could not reproduce these results because of the “enhanced” momentum coupling to the ambient plasma. However, we note that the charge exchange rates in figure 5.29 start at a minimum and increase to a maximum as the ion core interacts with the densest part of the neutral cloud. The total yield will therefore be greater in the hybrid code calculation since the core directly interacts with the neutral cloud while the densities are still high. (Recall, the observed neutral disk inventories were roughly 0.3-0.7% of the released material while the hybrid code results showed about 1.5%.) In the actual release, it is unlikely that charge exchanges occurring while the neutral cloud sweeps past the core will have any significant impact on the outcome of the skidding or other cloud structuring processes.

6.3 Ion Cloud Morphology

Although the simulated ion core skidding distances differed from the observations by nearly one order of magnitude, the simulated ion cloud structures are consistent with observation. The observables, shown in figures 2.2, 2.4, and 2.6, include the herringbone structure, the pronged backjet of the neutral disk, and the elongation of the cloud along the magnetic field. The spatial extent of these structures is a function of the lifetime of the skidding core. In the case of the hybrid code simulation the structuring only occurs within the first 2 seconds. Once significant momentum has been transferred away from the core, the release is passive and no further structuring should be expected.

Figures 5.1, 5.3, 5.4, and 5.5 illustrate the simulated ion cloud structures. It appears that the structure of the ion cloud is affected by a combination of processes which include, foremost, cycloid bunching, ion gyromotion, the polarization electric field topology, and parallel electric fields.

Cycloid bunching is a periodic ion density enhancement in the x direction which occurs when an ionizing cloud is streaming perpendicular to a magnetic field [Bernhardt et al., 1993]. The bunching distance is given by $\lambda = 2\pi v_{sat}/\omega_i$ which for these releases is ~ 2.8 km. In the xz projections of the ion cloud (figure 5.1), these bunching structures appear as striations that are separated by roughly 3 km as expected. In the xy plane projections a

group of ions are seen trailing the main ion core again by roughly 3 km. It therefore appears that cycloid bunching is responsible for partitioning the skidding ion core. Depending on the densities of the various core fragments, the respective *potential* skidding distances of these fragments will vary. In addition, figure 5.3 shows structures in the neutral cloud region between 16 and 19 km. This is consistent with the observations of the high altitude (6180 km) G2 release where the cycloid bunching distance was ~ 10 km [Bernhardt et al., 1993]. Note that the small spatial scale of the G1, G9, and G11A cycloid bunching made observation of bunching structures difficult. However, [Milinevsky et al., 1994] reports the observation of ion filaments in the G9 release near the release edge of the ion cloud that are presumably attributed to cycloid bunching. The hybrid code clearly confirms this effect and even though these structures seem observationally insignificant one should keep in mind that the initial structuring of the core may have long term ramifications for the overall ion cloud structure.

Cycloid bunching is a geometric consequence of the ion gyromotion and this gyromotion also contributes directly to the structure of the ion core. Figures 5.1 and 5.3 show resulting asymmetries of the ion core due to the clockwise gyration of the ions. The densest regions tend to drift in the $-y$ direction as the ions become magnetized due to the momentum transfer from the ion core to the ambient plasma. Notice the ions that have been extracted from the densest portion of the core are displaced roughly one gyrodiameter in the $-y$ direction from the midplane of the release cloud. These xy plane asymmetries in turn affect the polarization electric field topology.

Figure 5.1 shows a group of ions above ($+y$ direction) and ahead ($+x$ direction) of the densest portion of the core. This group of ions first appears at 1.2 s and continues to develop until at least 1.6 s staying forward of the main ion core for the remainder of the simulation run. This feature is unexpected as the ion gyromotion would dictate displacements in the $-y$ direction only. The explanation for this feature stems from the polarization electric field topology. The electric field is primarily in the $+y$ direction throughout the ion cloud. However, near the fringes of the cloud the electric field is dipolar. As the ion core is displaced in the $-y$ direction, ions see the dipolar field of the dense ion core and therefore obtain a drift component in the $+y$ direction. Observational evidence of a similar (or perhaps identical) event was obtained from the AMPTE artificial comet experiments

[Valenzuela et al., 1986] where the comet head was observed to displace transverse to the solar wind flow or in the $+y$ direction for our coordinate system. Unfortunately, the CRRES optical data do not provide conclusive evidence for such a displacement because of the combination of a non-ideal viewing geometry along the magnetic field line (xy plane projection) and detector saturation. Further studies of the AMPTE comet using the hybrid code should be conducted.

In the xz plane we see that the ions expand freely along the magnetic field and consequently the core acquires cylindrical symmetry. However, as figures 5.4 and 5.5 clearly show, the core splits into two highly localized parts. To either side of these dense regions ($\pm y$) the core density is uniform along the magnetic field. The pronged backjet of the neutral disk lends observational support to this finding. If these density inhomogeneities along \mathbf{B} did exist then the charge exchange rates would also be elevated in these regions, resulting in a pronged backjet. Keep in mind that we have not yet considered the effects of ambipolar diffusion which would tend to smooth these density gradients along the magnetic field. Figure 5.31 shows that electron temperatures on the order of 10^5 K are sufficient to remove the density gradients. If the elongation of the ion cloud was caused by CIV heated electrons, then we might not see the pronged backjet.

The explanation for the split ion core stems from the neutral particle distribution. Recall that the neutral cloud is a shell-like structure with a Gaussian profile while the core is a cylindrical structure that is confined radially by the magnetic field but that expands freely along \mathbf{B} . Initially the core moves with the neutral population and sweeps up any fresh ions that have been created in its path. The resulting density profile of the ion core can therefore be described qualitatively by projecting the neutral distribution onto the ion core. Figure 6.3 illustrates this projection. The shaded regions show that the number of fresh ions created within the path of the core at any given time is larger at the ends of the core compared to the central region. Furthermore, notice that the near- 90° pitch angle particles will be extracted from the core by the magnetic field since the densities are lower here relative to the rest of the core.

This description of the core's evolution is consistent with the formation of the observed herringbone structures. Namely, ions will be preferentially extracted from the core starting with 90° pitch angles and increasing at a rate that is proportional to the neutral cloud expansion.

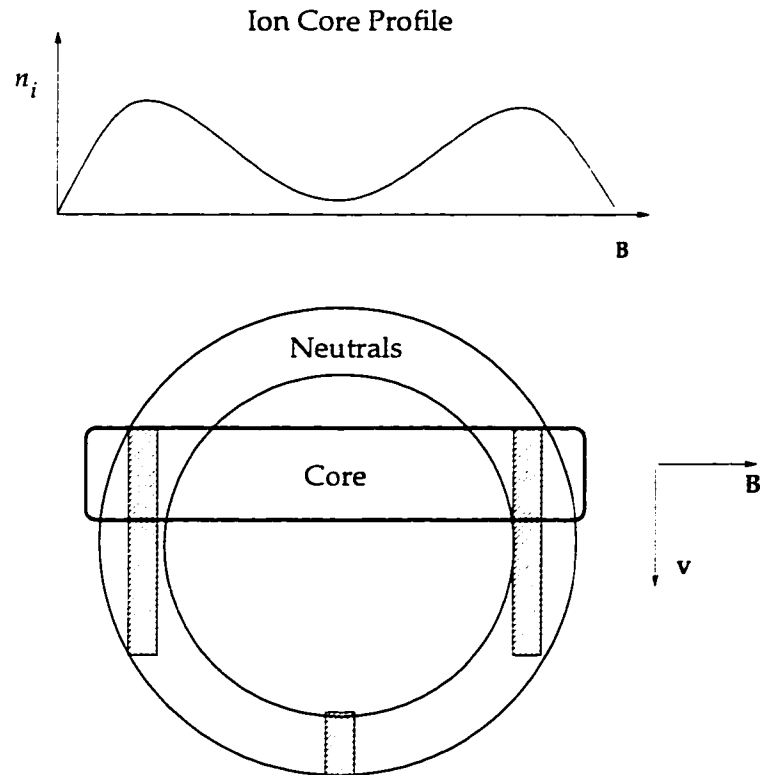


Figure 6.3: An illustration of the mechanism for generating density gradients in the core along the magnetic field. The neutral cloud shell and the cylindrical ion core are labeled. The three shaded regions multiplied by the density of ions produced in the neutral cloud show that a larger number of ions will be added to the skidding core at the ends compared to the center.

Ultimately, however, the density profile of the core along \mathbf{B} will be modified as the core loses momentum and falls back to the rear flanks of the neutral cloud where a larger portion of 90° pitch angle particles will be added to the core. We observed in the G1 release that the processes responsible for the herringbone structure last for roughly 3–4 seconds. From this we infer that the core probably fell behind the neutral cloud at this time.

Another consideration regarding the herringbone structure is the direction of the parallel electric fields. Figure 6.1 indicates that the parallel electric fields are asymmetric about the core. This configuration is consistent with a potential electric field where

$$\oint \mathbf{E} \cdot d\mathbf{l} = 0 \quad (6.4)$$

which requires that the parallel components be equal and opposite in the opposing current filaments. Consequently, ions will be accelerated away from the core on one side and toward the core on the other side. Figure 3.4 illustrates the effect of a potential electric field on the ion cloud morphology. The enhanced density in the $z = 0$ midplane are the result of inward directed parallel fields while the elongation of the ion cloud along z are the result of outward directed parallel fields. This suggests that a potential electric field will further accentuate the herringbone structure by moving ions to the $z = 0$ midplane of the ion cloud.

Finally, questions regarding the observed double herring bone structure remain unresolved. It is possible that the core was fragmented initially via the cycloid bunching process which created two separate core structures with different densities. The low density core would be responsible for the first herringbone and the larger core might be responsible for the second. Insight into this problem would require a model with effective momentum transfer rates that allow for the long term skidding.

6.4 Conclusions

Optical observations of the CRRES chemical releases have revealed several features that provided clues to the coupling between the ion cloud and the ionosphere. These features included cross-field propagation, the formation of a neutral disk due to charge exchange interactions, and ion cloud morphology. Our goal was to understand the physical pro-

cesses associated with these optical features using a three-dimensional hybrid code simulation. Ultimately, we wanted to link optical signatures with the processes associated with the Critical Ionization Velocity effect (CIV). Conclusive evidence for CIV is still lacking; however, new insights into the cloud-ionosphere coupling mechanisms have been uncovered as a result of this study. The main findings of this thesis are summarized below.

Skidding

The hybrid code simulation demonstrated that filamentary current sheaths surrounding the ion cloud are propagated by Alfvén waves. The skidding ion core draws a large current, and hence the current density in these sheaths exceeds the random thermal current of the ionosphere. A possible consequence of the high current density are plasma instabilities that generate parallel electric fields. These parallel electric fields damp the Alfvén wave and thus diminish the transfer of momentum from the skidding ion core to the ionosphere. If the perpendicular extent of the current filaments is limited to electron inertial lengths, then inertial Alfvén waves will propagate a parallel electric field. Numerical experiments with the hybrid code suggest that the perpendicular extent of the current filaments scale with the grid resolution and hence scale lengths comparable with electron inertial lengths are expected.

Neutral Disk

Charge exchange processes play an insignificant role in the evolution of the ion core and the associated cloud structures. However, the double-pronged structure of the disk provided useful diagnostic information regarding the split structure of the skidding core.

Ion Cloud Morphology

Parallel electric fields are responsible for the observed elongation of the ion cloud along the magnetic field line, and the herringbone structures observed in the G1 release are consistent with the evolution of the skidding ion core. Conclusive information regarding the double-herringbone structure is still lacking, although it is possible that fragmentation of the skidding core could have been a contributing factor.

CIV

Although electron energies in excess of 100 eV have been observed in previous release experiments, it is not clear whether electron acceleration is solely responsible for the parallel electric fields. If ambipolar diffusion occurs due to electron heating, then inhomogeneities in the ion core along the magnetic field would be smoothed. But without the split core structure, as found in the hybrid code simulation, a pronged backjet would not be possible. Therefore, the observation of the pronged backjet does not support CIV.

6.4.1 Future extensions of this study

Although solid observational evidence for the CIV effect in the CRRES releases is still lacking, this study has demonstrated the importance of electron inertial effects in limiting the momentum transfer from an ionizing neutral cloud to an ambient plasma. These findings will have direct application to the design of future chemical release experiments. Careful attention must be given to passive release experiments where the release particles are intended to serve as field line tracers. If the initial ion cloud densities are too high, then the perturbing effects of skidding may persist for an unwanted period of time. Perturbing release experiments should be conducted to investigate, specifically, the coupling processes discussed in this thesis. Rather than positioning the diagnostic payload 0.2 s downstream of the release as in the CRIT I and II releases, instrumentation might be placed 1-2 seconds downstream and (hopefully) in the path of the skidding core. At this point the full polarization electric fields would have developed and the measurement of parallel electric fields would verify the current limitation processes suspected in the CRRES releases.

The results of past chemical releases should also be reinvestigated. A hybrid code simulation of the AMPTE release, for example, may provide insight into the unexpected perpendicular displacement of the comet head. Also, the skidding core should be considered in the analysis of previous CIV experiments. If the momentum transfer rates are diminished, then more energy is available in the ion cloud to drive CIV processes.

From the perspective of numerical simulation, the CRRES optical data set provided a unique opportunity for the development of a hybrid code and its application to space plasma simulation. The simulation was used to diagnose the physical processes responsi-

ble for the observations, while the observations served to verify to the code. The importance of electron inertia, as indicated in the conclusions of this study, suggest that extreme caution be exercised with future space plasma simulations. Any simulation of a system where sharp density gradients exist, or where density gradients steepen, should account for electron inertia. Presently it is computationally prohibitive to include electron inertia into a three-dimensional hybrid code simulation of the magnitude of this CRRES chemical release simulation. However, as increasing computational resources permit, the inclusion of electron inertia seems vital.

Finally, the CRRES releases represent a general physical system that can be found in a variety of space physics and astrophysical applications to which the results of this study can be applied. Sharp density gradients, like those associated with the skidding ion core, are commonly found in the ionosphere and on auroral field lines [*Persoon et al.*, 1988]. It is possible that parallel electric fields and filamentary current layers associated with these density gradients could have application to fine-structured auroral arcs (thickness ~ 100 m). Other systems similar to a chemical release include cometary environments, the interaction of Io with the Jovian magnetosphere, and any system where Alfvén's CIV effect is suspected as a source of anomalous ionization.

Appendix A

An energy conservation theorem for the hybrid code

First consider the non-dissipative equation for ion motion for the k th particle [Swift, 1996].

$$m_p \frac{d\mathbf{v}_k}{dt} = q(\mathbf{E}'(\mathbf{x}_k) + \mathbf{v}_k \times \mathbf{B}'(\mathbf{x}_k)) \quad (\text{A.1})$$

where

$$\begin{aligned} \mathbf{E}'(\mathbf{x}_k) &= \int S(\mathbf{x} - \mathbf{x}_k) \mathbf{E}'(\mathbf{x}) d^3x \\ \mathbf{B}'(\mathbf{x}_k) &= \int S(\mathbf{x} - \mathbf{x}_k) \mathbf{B}'(\mathbf{x}) d^3x \end{aligned} \quad (\text{A.2})$$

and where m_p and m_f are the respective masses of the particle and fluid components, and $S(\mathbf{x} - \mathbf{x}_k)$ is the particle shape function. Summing over all particles gives

$$\sum_{k=1}^{N_i} m_p \frac{d\mathbf{v}_k}{dt} = \int q n_p (\mathbf{E}' + \mathbf{u}_p \times \mathbf{B}') d^3x \quad (\text{A.3})$$

where $\sum_{k=1}^{N_i} S(\mathbf{x} - \mathbf{x}_k) = n_p$ and $\sum_{k=1}^{N_i} \mathbf{v}_k S(\mathbf{x} - \mathbf{x}_k) = n_p \mathbf{u}_p$. Or in the simulation units

$$\sum_{k=1}^{N_i} m_p \frac{d\mathbf{v}_k}{dt} = m_p \int n_p \frac{d\mathbf{u}_p}{dt} = m_f \int n_p (\mathbf{E} + \mathbf{u}_p \times \mathbf{B}) d^3x \quad (\text{A.4})$$

where $\mathbf{E} = q\mathbf{E}'/m_f$ and $\mathbf{B} = q\mathbf{B}'/m_f$. Similarly, the analogous expression for the fluid momentum integrated over all space is

$$m_f n_f \int \frac{d\mathbf{u}_f}{dt} d^3x = m_f n_f \int (\mathbf{E} + \mathbf{u}_f \times \mathbf{B}) d^3x \quad (\text{A.5})$$

Next we take the scalar product of A.4 and A.5 with \mathbf{u}_p and \mathbf{u}_f respectively and add the two expressions to get the total energy, \mathcal{E} , of the combined particle/fluid plasma

$$\begin{aligned} \frac{d\mathcal{E}}{dt} &= m_f \int \mathbf{E} \cdot (n_p \mathbf{u}_p + n_f \mathbf{u}_f) d^3x \\ &= m_f \int \mathbf{E} \cdot \left(n \mathbf{u}_e + \frac{\nabla \times \mathbf{B}}{\alpha} \right) d^3x \end{aligned} \quad (\text{A.6})$$

where $\alpha = \frac{\mu_0 e^2}{m_p}$. To zeroth order the electron flow is perpendicular to the electric field so $\mathbf{E} \cdot \mathbf{u}_e = 0$. Now recall that

$$\mathbf{E} \cdot (\nabla \times \mathbf{B}) = \mathbf{B} \cdot (\nabla \times \mathbf{E}) - \nabla \cdot (\mathbf{E} \times \mathbf{B}) \quad (\text{A.7})$$

Using this vector identity together with Faraday's law and the divergence theorem, we can now write the expression for energy conservation as

$$\frac{d}{dt} \left(\mathcal{E} + \frac{1}{\alpha} \int B_1^2 d^3x \right) = \int \frac{\mathbf{E} \times \mathbf{B}}{\alpha} \cdot d\mathbf{A} \quad (\text{A.8})$$

Notice that this expression does not contain any electric field energy density due to the assumption of quasi-neutrality and neglect of the displacement current. The energy conservation for the hybrid code is therefore the particle and fluid kinetic energy and the volume integral of the magnetic field energy density minus the Poynting flux at the boundaries. Figure A.1 shows the energy conservation diagnostic output from the large G9 simulation.

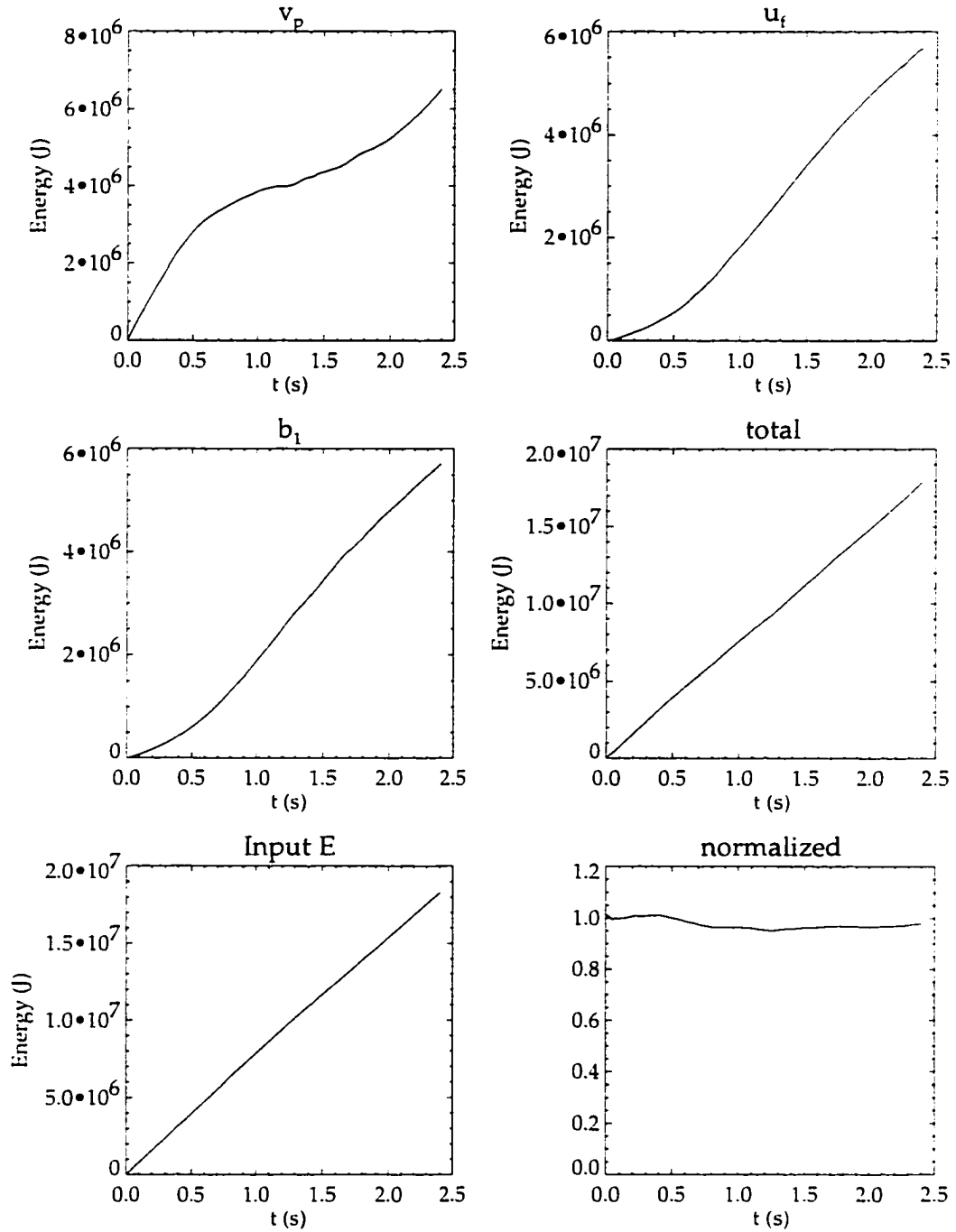


Figure A.1: Energy conservation for the large G9 simulation. The total energy is composed of the particle kinetic energy, fluid flow kinetic energy, and the perturbation magnetic field energy. The normalized energy is the total energy divided by the input particle kinetic energy.

Appendix B

A momentum conservation theorem for the hybrid code

We start with the non-dissipative equation for particle ion motion derived in Appendix A.

In the simulation units

$$\sum_{k=1}^{N_i} m_p \frac{d\mathbf{v}_k}{dt} = m_f \int n_p (\mathbf{E} + \mathbf{u}_p \times \mathbf{B}) d^3x \quad (\text{B.1})$$

where $\mathbf{E} = q\mathbf{E}'/m_f$ and $\mathbf{B} = q\mathbf{B}'/m_f$. Using the electron momentum equation and Ampere's law gives the following expression for the electric field,

$$\mathbf{E} = \left[\frac{\nabla \times \mathbf{B}}{\alpha n} - \left(\frac{n_p}{n} \mathbf{u}_p + \frac{n_f}{n} \mathbf{u}_f \right) \right] \times \mathbf{B} \quad (\text{B.2})$$

So

$$\sum_{k=1}^{N_i} m_p \frac{d\mathbf{v}_k}{dt} = m_f \int n_p \left[\left(\frac{\nabla \times \mathbf{B}}{\alpha n} - \frac{n_p}{n} \mathbf{u}_p - \frac{n_f}{n} \mathbf{u}_f \right) \times \mathbf{B} + \mathbf{u}_p \times \mathbf{B} \right] d^3x \quad (\text{B.3})$$

The analogous expression for the fluid momentum integrated over all space is

$$m_f n_f \int \frac{\partial \mathbf{u}_f}{\partial t} d^3x = m_f n_f \int \left[-\mathbf{u}_f \cdot \nabla \mathbf{u}_f + \left(\frac{\nabla \times \mathbf{B}}{\alpha n} - \frac{n_p}{n} \mathbf{u}_p - \frac{n_f}{n} \mathbf{u}_f \right) \times \mathbf{B} + \mathbf{u}_f \times \mathbf{B} \right] d^3x \quad (\text{B.4})$$

The expression for conservation of total momentum is

$$\begin{aligned}
\sum_{k=1}^{N_i} m_p \frac{d\mathbf{v}_k}{dt} + m_f n_f \int \frac{\partial \mathbf{u}_f}{\partial t} d^3x &= m_f \int \frac{\nabla \times \mathbf{B}}{\alpha} \times \mathbf{B} d^3x \\
&- m_f \int (n_p \mathbf{u}_p + n_f \mathbf{u}_f) \times \mathbf{B} d^3x \\
&+ m_f \int (n_p \mathbf{u}_p + n_f \mathbf{u}_f) \times \mathbf{B} d^3x \\
&- m_f n_f \int (\mathbf{u}_f \cdot \nabla) \mathbf{u}_f d^3x \\
&= m_f \int \frac{\nabla \times \mathbf{B}}{\alpha} \times \mathbf{B} d^3x - m_f n_f \int (\mathbf{u}_f \cdot \nabla) \mathbf{u}_f d^3x
\end{aligned} \tag{B.5}$$

Recall that

$$\begin{aligned}
(\nabla \times \mathbf{B}) \times \mathbf{B} &= (\mathbf{B} \cdot \nabla) \mathbf{B} - \frac{1}{2} \nabla B^2 \\
&= (\mathbf{B} \cdot \nabla) \mathbf{B} + (\nabla \cdot \mathbf{B}) \mathbf{B} - \frac{1}{2} \nabla B^2
\end{aligned} \tag{B.6}$$

Also note that

$$(\mathbf{u}_f \cdot \nabla) \mathbf{u}_f = (\mathbf{u}_f \cdot \nabla) \mathbf{u}_f + (\nabla \cdot \mathbf{u}_f) \mathbf{u}_f - (\nabla \cdot \mathbf{u}_f) \mathbf{u}_f \tag{B.7}$$

So we can now introduce a stress tensor of the form

$$T_{ij} \equiv \frac{m_f}{\alpha} \left(B_i B_j - \frac{1}{2} \delta_{ij} B^2 \right) - m_f n_f u_{f_i} u_{f_j} \tag{B.8}$$

such that

$$(\nabla \cdot \vec{\mathbf{T}})_j = \frac{m_f}{\alpha} \left[(\mathbf{B} \cdot \nabla) B_j + (\nabla \cdot \mathbf{B}) B_j - \frac{1}{2} \nabla_j B^2 \right] - m_f n_f [(\mathbf{u}_f \cdot \nabla) \mathbf{u}_f + (\nabla \cdot \mathbf{u}_f) \mathbf{u}_f] \tag{B.9}$$

Now B.6 can be rewritten to give the following conservation expression

$$\sum_{k=1}^{N_i} m_p \frac{d\mathbf{v}_k}{dt} + m_f n_f \int \frac{\partial \mathbf{u}_f}{\partial t} d^3x = \oint_S \vec{\mathbf{T}} \cdot d\mathbf{a} - m_f n_f \int (\nabla \cdot \mathbf{u}_f) \mathbf{u}_f d^3x \tag{B.10}$$

The total change in momentum of the system is therefore equal to the maxwell stress on the boundaries plus an error term for the assumption of incompressibility. Figure B.1 shows the momentum conservation diagnostic output from the large G9 simulation which includes particle and fluid bulk flow momentum, maxwell stresses at the boundary surfaces, and the input particle momentum.

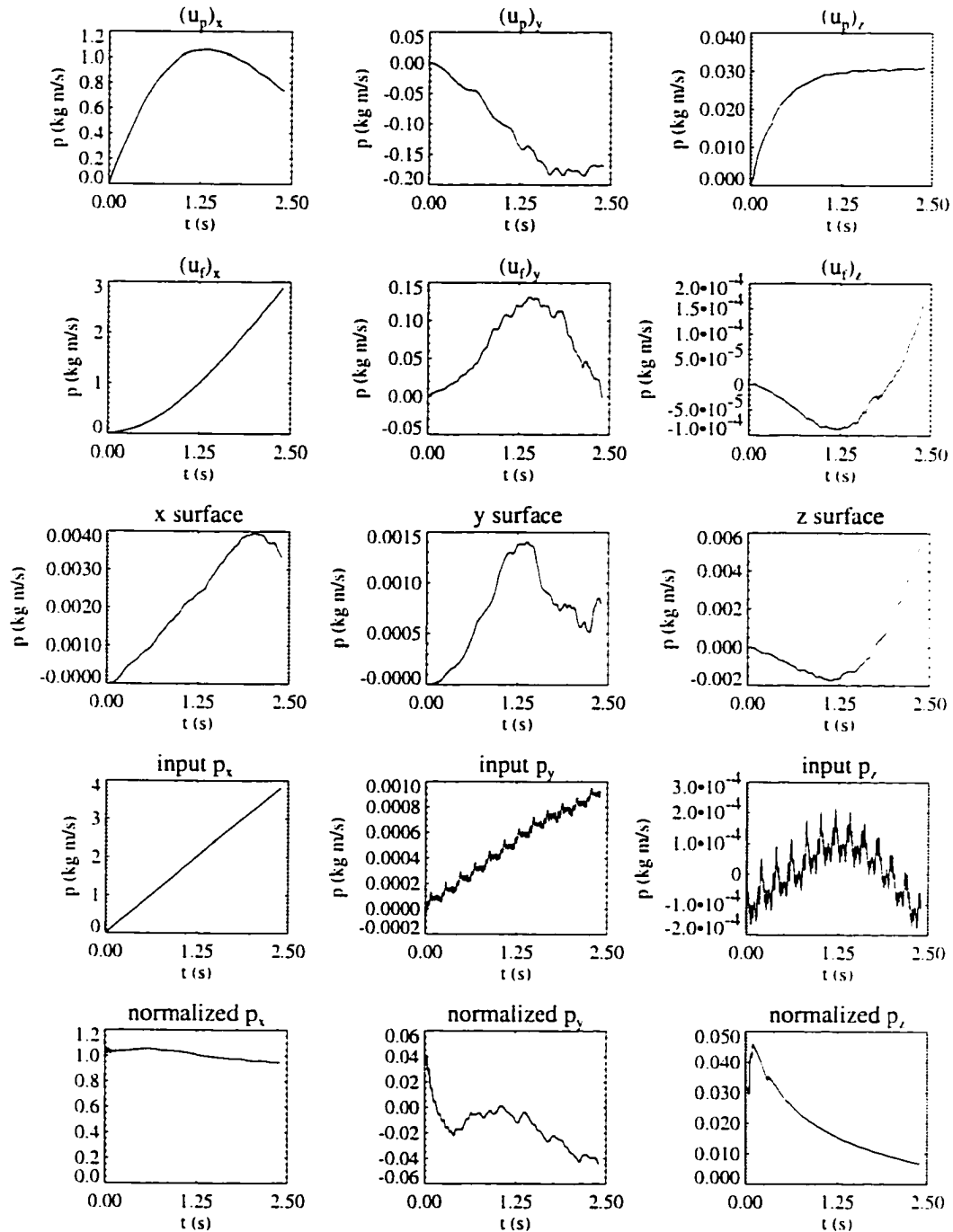


Figure B.1: Momentum conservation for the large G9 simulation. Columns 1, 2, and 3 show the x, y, and z components of the momentum respectively. The respective rows show the momentum associated with the particle bulk flow, fluid flow momentum, maxwell stresses at the boundary surfaces, input particle momentum, and the normalized momentum which is the sum of the of rows 1-3 divided by the input momentum.

Appendix C

Inertial Alfvén waves

The dispersion relation for electromagnetic waves in a cold plasma is [Stix, 1992]

$$n^2 = \frac{B \pm F}{2A} \quad (\text{C.1})$$

where

$$F^2 = (RL - PS)^2 \sin^4 \theta + 4P^2 D^2 \cos^2 \theta \quad (\text{C.2})$$

$$B = RS \sin^2 \theta + PS(1 + \cos^2 \theta)$$

$$A = S \sin^2 \theta + P \cos^2 \theta$$

and where

$$P = 1 - \frac{\omega_{pe}^2}{\omega^2} - \frac{\omega_{pi}^2}{\omega^2} \quad (\text{C.3})$$

$$R = 1 - \frac{\omega_{pe}^2}{\omega(\omega - \Omega_e)} - \frac{\omega_{pi}^2}{\omega(\omega + \Omega_i)}$$

$$L = 1 - \frac{\omega_{pe}^2}{\omega(\omega + \Omega_e)} - \frac{\omega_{pi}^2}{\omega(\omega - \Omega_i)}$$

$$S = \frac{1}{2}(R + L)$$

$$D = \frac{1}{2}(R - L)$$

The angle θ is the angle between \mathbf{B}_0 and \mathbf{n} where $\mathbf{n} = kc/\omega$.

We will first assume that $\omega \sim \Omega_i$ and later look at the limiting case where $\omega \ll \Omega_i$. It follows that $\Omega_e \gg \Omega_i$, $\Omega_e \gg \omega$, and $\omega_{pe} \gg \omega$. For typical ionospheric plasma parameters

note that $\omega_{ps} \gg \Omega_s$. Using these approximations we have that

$$P = -\frac{\omega_{pe}^2}{\omega^2} \quad (\text{C.4})$$

$$\begin{aligned} R &= -\frac{\omega_{pe}^2}{\omega(\omega - \Omega_e)} - \frac{\omega_{pi}^2}{\omega(\omega + \Omega_i)} \quad (\text{C.5}) \\ &= \frac{\omega_{pe}^2}{\omega\Omega_e} - \frac{\omega_{pi}^2}{\omega(\omega + \Omega_i)} \\ &= \frac{\omega_{pi}^2}{\omega\Omega_i} - \frac{\omega_{pi}^2}{\omega(\omega + \Omega_i)} \end{aligned}$$

$$= \frac{\omega_{pi}^2}{\Omega_i(\omega + \Omega_i)}$$

$$L = -\frac{\omega_{pe}^2}{\omega(\omega + \Omega_e)} - \frac{\omega_{pi}^2}{\omega(\omega - \Omega_i)} \quad (\text{C.6})$$

$$= -\frac{\omega_{pe}^2}{\omega\Omega_e} - \frac{\omega_{pi}^2}{\omega(\omega - \Omega_i)}$$

$$= -\frac{\omega_{pi}^2}{\omega\Omega_i} - \frac{\omega_{pi}^2}{\omega(\omega - \Omega_i)}$$

$$= \frac{\omega_{pi}^2}{\Omega_i(\Omega_i - \omega)}$$

$$S = \frac{\omega_{pi}^2}{\Omega_i^2 - \omega^2} \quad (\text{C.7})$$

$$D = \frac{\omega_{pi}^2}{\Omega_i} \frac{\omega}{(\omega^2 - \Omega_i^2)} \quad (\text{C.8})$$

In the limiting case where $\omega \ll \Omega_i$ we have that $R \sim L \sim \omega_{pi}^2/\Omega_i^2$, so $D \sim 0$. The dispersion relation is

$$n^2 = \frac{RL\sin^2\theta + PS(1 + \cos^2\theta) \pm (RL - PS)\sin^2\theta}{2S\sin^2\theta + 2P\cos^2\theta} \quad (\text{C.9})$$

Consider the - sign first, so

$$\begin{aligned} n^2 &= \frac{RL\sin^2\theta + PS(1 + \cos^2\theta) + PS\sin^2\theta}{2S\sin^2\theta + 2P\cos^2\theta} \quad (\text{C.10}) \\ &= \frac{\frac{\omega_{pi}^4}{\Omega_i^2(\Omega_i^2 - \omega^2)}\sin^2\theta - \frac{\omega_{pe}^2}{\omega^2} \frac{\omega_{pi}^2}{\Omega_i^2 - \omega^2} (1 + \cos^2\theta) + \frac{\omega_{pe}^2}{\omega^2} \frac{\omega_{pi}^2}{\Omega_i^2 - \omega^2} \sin^2\theta}{2\frac{\omega_{pi}^2}{\Omega_i^2 - \omega^2} \sin^2\theta - 2\frac{\omega_{pe}^2}{\omega^2} \cos^2\theta} \end{aligned}$$

Now in the limit where $\omega^2 \ll \Omega_i^2$ and using $\frac{\Omega_i^2}{\omega_{pi}^2} = \frac{V_A^2}{c^2}$ we have

$$\frac{k^2 c^2}{\omega^2} = \frac{-\frac{c^2 \omega_{pe}^2}{V_A^2 \omega^2}}{\frac{c^2}{V_A^2} \sin^2 \theta - \frac{\omega_{pe}^2}{\omega^2} \cos^2 \theta} \quad (\text{C.11})$$

Given the electron inertial length, $\lambda_e = \frac{c}{\omega_{pe}}$, the dispersion relation for inertial Alfvén waves is

$$\omega^2 = \frac{V_A^2 k_x^2}{1 + k_x^2 \lambda_e^2} \quad (\text{C.12})$$

where $k_x^2 = k^2 \sin^2 \theta$ and $k_z^2 = k^2 \cos^2 \theta$. For perpendicular propagation with size scales on the order of electron inertial lengths, the dispersion relation is modified by the second term in the denominator.

Now look at the polarization. From *Stix* [1992]

$$\begin{aligned} \frac{E_z}{E_x} &= \frac{\cos \theta \sin \theta}{\sin^2 \theta - P/n^2} \\ &= \frac{c^2 \omega^2}{V_A^2 \omega_{pe}^2} \tan \theta \end{aligned} \quad (\text{C.13})$$

Thus for $\theta > 0$, E_z will always be nonzero.

Bibliography

Alfvén, H., *On the Origin of the Solar System*. Oxford University Press, New York, 1954.

Banks, P. M. and G. Kockarts, *Aeronomy*. Academic Press, New York, 1973.

Bernhardt, P. A., Probing the magnetosphere using chemical releases from the CRRES satellite, *Phys. Fluids B*, 4, 2249, 1992.

Bernhardt, P. A., J. D. Huba, M. B. Pongratz, D. J. Simons, and J. H. Wolcott, Plasma irregularities caused by cycloid bunching of the CRRES G-2 barium release, *J. Geophys. Res.*, 98(A2), 1613, 1993.

Biasca, R., D. Hastings, and D. Cooke, Upper bound estimates of anomalous ion production in space based critical ionization velocity experiments, *J. Geophys. Res.*, 98, 17569, 1993.

Birk, G. T. and A. Otto, The resistive tearing instability for generalized resistivity models, *Phys. Fluids B*, 3(7), 1746, 1991.

Blaunstein, N. S., G. P. Milinevsky, V. A. Savchenko, and E. V. Mishin, Formation and development of striated structure during plasma cloud evolution in the Earth's ionosphere, *Planet. Space Sci.*, 41, 453, 1993.

Brenning, N., Review of impact experiments on the critical ionization velocity, in *Rep. TRITA-EPP-82-14*. R. Inst. of Technology, Stockholm, 1982.

Brenning, N., Review of the CIV phenomenon, *Space Sci. Rev.*, 59, 209, 1992.

Brenning, N., Current limitations in Alfvén wings, TRITA-ALP-1995-02.

- Brenning, N., M. C. Kelley, J. Providakes, H. C. Stenbaek-Nielsen, and C. Swenson, Barium swarm: an ionospheric alternating current generator in CRIT I, *J. Geophys. Res.*, 96, 9735, 1991a.
- Brenning, N., C. G. Fälthammar, G. Haerendel, M. C. Kelley, G. Marklund, R. Pfaff, J. Providakes, H. C. Stenbaek-Nielsen, C. Swenson, R. Torbert, and E. M. Wescott, Interpretation of the electric fields measured in an ionospheric critical ionization velocity experiment, *J. Geophys. Res.*, 96, 9719, 1991b.
- Buneman, O., Dissipation of currents in ionized media, *Phys. Rev.*, 115(3), 503, 1959.
- Cameron, S., Lunar transient phenomena, *Sky & Telescope*, 1991.
- Carlsten, J. L., Photoionization of barium clouds via the ³D metastable levels, *Planet. Space Sci.*, 23, 53, 1975.
- Danielsson, L., Review of the critical velocity of gas-plasma interaction, I: experimental observations, *Astrophysics and Space Science*, 24, 459, 1973.
- Davis, T. N., Chemical releases in the ionosphere, *Rep. Prog. Phys.*, 42, 1565, 1979.
- Davis, T. N., G. J. Romick, E. M. Wescott, R. A. Jeffries, D. M. Kerr, and H. M. Peek, Observations of the development of striations in large barium ion clouds, *Planet. Space Sci.*, 22, 67, 1974.
- Deehr, C. S., E. M. Wescott, H. C. Stenbaek-Nielsen, G. H. Romick, T. J. Hallinan, and H. Föppl, A critical velocity interaction between fast barium and strontium ions in the terrestrial ionospheric plasma, *Geophys. Res. Lett.*, 9, 195, 1982.
- Delamere, P. A., H. C. Stenbaek-Nielsen, E. M. Wescott, and D. L. Hampton, Optical observations of the early ($t < 5$ s) ion dynamics of the CRRES G1, G9, and G11A releases, *J. Geophys. Res.*, 101, 17243, 1996.
- Drapatz, S. W., The radiative transfer problem in freely expanding gaseous clouds and its application to barium clouds, *Planet. Space Sci.*, 20, 663, 1972.
- Fletcher, C. A. J., *Computational Techniques for Fluid Dynamics*, volume 1. Springer-Verlag, Berlin, 1991.

- Formisano, V., A. A. Galeev, and R. Z. Sagdeev, The role of the critical ionization velocity phenomena in the production of inner coma cometary plasma, *Planet. Space Sci.*, 30, 491, 1982.
- Galeev, A. A. and I. C. Chabibrachmanov, Origin and energetics of the Io plasma torus, *Adv. Space Res.*, 3, 71, 1983.
- Galvez, M. and J. E. Borovsky, The expansion of polarization charge layers into a magnetized vacuum: Theory and computer simulations, *Phys. Fluids B*, 3, 1892, 1991.
- Gatsonis, N. A. and D. E. Hastings, A three-dimensional model and initial time numerical simulation for an artificial plasma cloud in the ionosphere, *J. Geophys. Res.*, 96, 7623, 1991.
- Gatsonis, N. A. and D. E. Hastings, Evolution of the plasma environment induced around space, *J. Geophys. Res.*, 97, 14989, 1992.
- Genoni, T. C., L. A. Wright, and D. L. Cooke, CIV model for ARGOS xenon release, SM42A-1, *Transac. Am. Geophys. Union (EOS)*, 76, S255, 1995.
- Gokhman, E. M. and V. B. Ivanov, The generation of small-scale inhomogeneities in ionized barium clouds, *Geomagnetism and Aeronomy*, 31, 151, 1991.
- Goldman, S. R., L. Baker, S. L. Ossakow, and A. J. Scannapieco, Striation formation associated with barium clouds in an inhomogeneous ionosphere, *J. Geophys. Res.*, 81, 5097, 1976.
- Haerendel, G., Alfvén's critical velocity effect tested in space, *Z. Naturforsch.*, 37a, 728, 1982.
- Haerendel, G., Active plasma experiments, in *AMPTE Scientific Preprints*, volume 49. Max-Planck-Institute für Physik und Astrophysik, 1986.
- Hallinan, T. J., Observed rate of ionization in shaped-charge releases of barium in the ionosphere, *J. Geophys. Res.*, 93, 8705, 1988.
- Hampton, D. L., *Optical Observations of Critical Ionization velocity chemical releases in the ionosphere: The role of collisions*, Ph.D. thesis, University of Alaska Fairbanks, 1996.

- Harned, D. S., Quasineutral hybrid simulation of macroscopic plasma phenomena, *J. Comput. Phys.*, 47, 452, 1982.
- Hasegawa, A. and C. Uberoi, *The Alfvén Wave*, DOE Critical Review Series. Technical Information Center, U. S. Department of Energy, 1982.
- Hoch, E. L. and T. J. Hallinan, Measurements of the time constant for steady ionization in shaped-charge barium releases, *J. Geophys. Res.*, 98, 7765, 1993.
- Huba, J. D., P. A. Bernhardt, and J. G. Lyon, Preliminary study of the CRRES magnetospheric barium releases, *J. Geophys. Res.*, 97, 11, 1992a.
- Huba, J. D., H. G. Mitchell, J. A. Fedder, and P. A. Bernhardt, 'Skidding' of the CRRES G-9 barium release, *Geophys. Res. Lett.*, 19, 1085, 1992b.
- Hunton, D. E., Space shuttle glow, *Scientific American*, 1989.
- Hunton, D. E., Long-term expansion characteristics of CRRES barium release clouds, *Geophys. Res. Lett.*, 20, 563, 1993.
- Hunton, D. E., Charge transfer reactions of metastable Ba(I) and Sr(I) in the CRRES G-11b chemical release experiment, *Geophys. Res. Lett.*, 22, 2115, 1995.
- Hunton, D. E., P. J. Wolf, and T. M. Shadid, Ionization mechanisms in CRRES chemical releases, 1. In-situ measurements and model results, *submitted to J. Geophys. Res.*, 1997.
- Iizuka, S. K., K. Saeki, N. Sato, and Y. Hatta, Buneman instability, Pierce instability, and double layer formation in a collisionless plasma, *Phys. Rev. Lett.*, 43, 404, 1979.
- Jacoby, G. H., D. A. Hunter, and C. A. Christian, A library of stellar spectra, *Ap. J. Suppl.*, 56, 257, 1984.
- Johnson, M. H. and J. Kierein, Combined Release and Radiation Effects Satellite (CRRES): Spacecraft and mission, *Journal of Spacecraft and Rockets*, 29, 556, 1992.
- Kindel, J. M. and C. F. Kennel, Topside current instabilities, *J. Geophys. Res.*, 96, 3055, 1971.
- Koons, H. C. and M. B. Pongratz, Electric fields and plasma waves resulting from a barium injection experiment, *J. Geophys. Res.*, 86, 1437, 1981.

- Koons, H. C. and J. L. Roeder, Observations of ELF fields near the low-altitude CRRES chemical releases, *J. Geophys. Res.*, 100, 5801, 1995.
- Linson, L. M. and J. B. Workman, Formation of striations in ionospheric plasma clouds, *J. Geophys. Res.*, 75, 2279, 1970.
- Liou, K., R. B. Torbert, and G. Haerendel, Momentum coupling in the CRIT II experiment, *J. Geophys. Res.*, 101, 19,649, 1996.
- Lysak, R. L. and C. W. Carlson, The effect of microscopic turbulence on magnetosphere-ionosphere coupling, *GRL*, 8(3), 269, 1981.
- Ma, T. Z. and R. W. Schunk, A two-dimensional model of plasma expansion in the ionosphere, *Planet. Space Sci.*, 38, 723, 1990.
- Ma, T. Z. and R. W. Schunk, Plasma cloud expansion in the ionosphere: three-dimensional simulation, *J. Geophys. Res.*, 96, 5793, 1991.
- Ma, T. Z. and R. W. Schunk, Ionization and expansion of barium clouds in the ionosphere, *J. Geophys. Res.*, 98, 323, 1993.
- Ma, T. Z. and R. W. Schunk, Dynamics of three-dimensional plasma clouds with coupling to the background ionosphere, *J. Geophys. Res.*, 99, 6331, 1994.
- Machida, S., A simulation study of the critical ionization velocity process, *J. Geophys. Res.*, 91, 1986.
- Maggs, J. E., Coherent generation of VLF hiss, *JGR*, 81(10), 1707, 1976.
- McBride, J. B., E. Ott, J. P. Boris, and J. H. Orens, Theory and simulation of turbulent heating by the modified two-stream instability, *Phys. Fluids*, 15, 2367, 1972.
- Milnevsky, G. P., A. I. Kashirin, Y. A. Romanovsky, H. C. Stenbaek-Nielsen, and M. C. Kelley, Long-lived artificial ion clouds in the Earth's ionosphere, *Geophys. Res. Lett.*, 20, 1019, 1993.

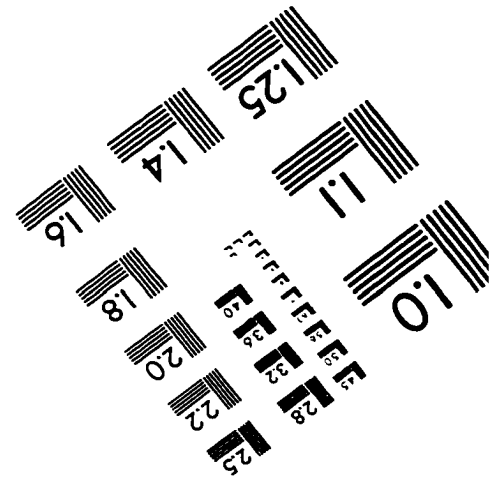
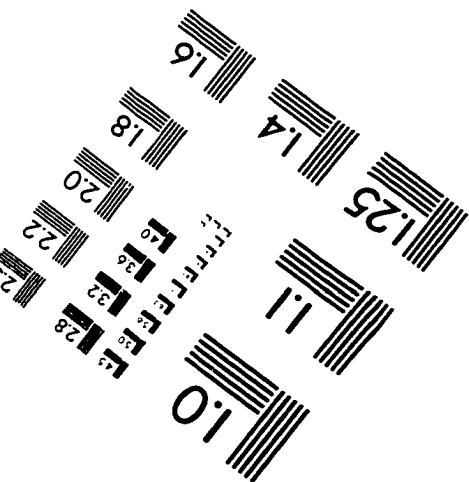
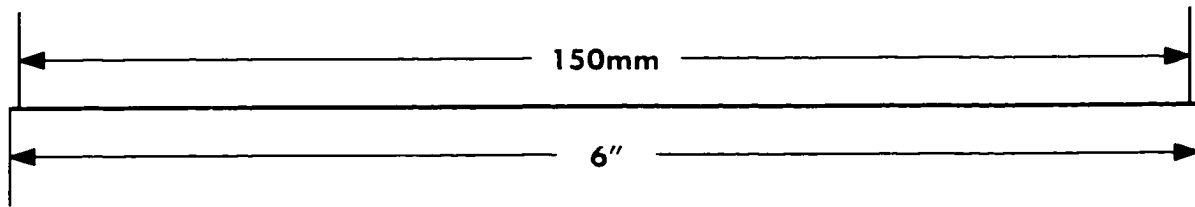
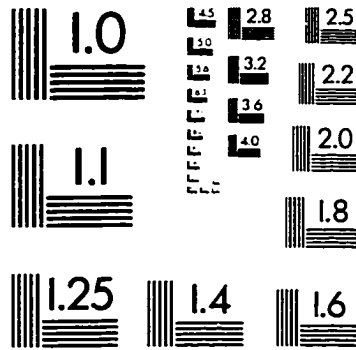
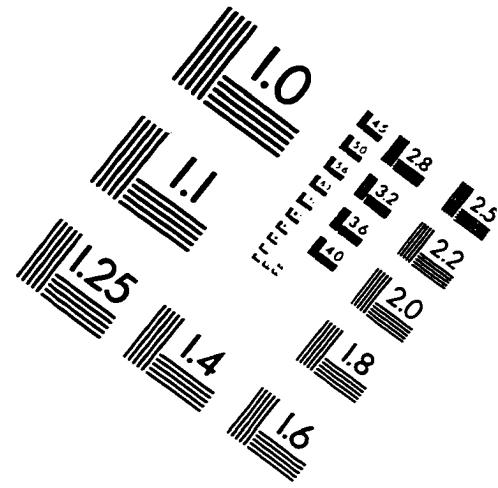
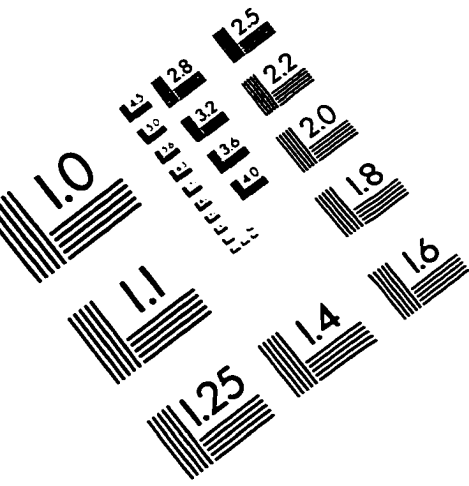
- Milnevsky, G. P., A. M. Evtushevsky, V. A. Kravchenko, and S. N. Zaitsev, The high-speed front of a glow in the initial structure of the CRRES Caribbean barium cloud, presented in London (21AM), 1994.
- Möbius, E., Critical velocity experiments in space, Active experiments in space, symposium at Alpbach, 1983, (ESA SP-195, July 1983).
- Moghaddam-Taaheri, E. and C. K. Goertz, Numerical quasi-linear study of the critical ionization velocity phenomenon, *J. Geophys. Res.*, *98*, 1443, 1993.
- Neubert, T., M. J. Mandell, S. Sasaki, B. E. Gilchrist, P. M. Banks, P. R. Williamson, W. J. Raitt, N. B. Meyers, K. I. Oyama, and I. Katz, The sheath structure around a negatively charged rocket payload, *J. Geophys. Res.*, *95*, 6155, 1990.
- Neubert, T., R. H. Miller, O. Buneman, and K. I. Nishikawa, The dynamics of low- β plasma clouds as simulated by a three-dimensional, electromagnetic particle code, *J. Geophys. Res.*, *97*, 12057, 1992.
- Newell, P. T., Review of the critical ionization velocity effect in space, *Rev. Geophys.*, *23*, 93, 1985.
- Persoon, A. M., D. A. Gurnett, W. K. Peterson, J. J. H. Waite, J. L. Burch, and J. L. Green, Electron density depletions in the nightside auroral zone, *J. Geophys. Res.*, *93*(A3), 1871, 1988.
- Piel, A., Review of laboratory experiments on Alfvén's critical ionization velocity, *Adv. Space Res.*, *10*(7), 47, 1990.
- Potter, D., *Computational Physics*. John Wiley & Sons Ltd., 1977.
- Raadu, M. A., The physics of double layers and their role in astrophysics, *Physics Reports*, *178*(2), 26, 1988.
- Reasoner, D. L., Chemical-release mission of CRRES, *Journal of Spacecraft and Rockets*, *29*, 580, 1992.
- Scales, W. A. and P. A. Bernhardt, Simulation of high-speed (orbital) releases of electron attachment materials in the ionosphere, *J. Geophys. Res.*, *96*, 13815, 1991.

- Schunk, R. W. and E. P. Szuszczewicz, Plasma expansion characteristics of ionized clouds in the ionosphere: Macroscopic formulation, *J. Geophys. Res.*, 96, 1337, 1991.
- Singer, H. J., CRRES: High altitude chemical releases and new observations in the inner magnetosphere, in E. A. Essex and J. D. Whitehead (eds.), *South Pacific STEP Workshop Proceedings*, p. 23, Melbourne, Australia. 1992.
- Stenbaek-Nielsen, H. C., Calculated emission rates for barium releases in space, *Planet. Space Sci.*, 37, 1441, 1989.
- Stenbaek-Nielsen, H. C., E. M. Wescott, D. Rees, A. Valenzuela, and N. Brenning, Non-solar UV produced ions observed optically from the "CRIT-II" critical ionization velocity experiment, *J. Geophys. Res.*, 95, 7749, 1990a.
- Stenbaek-Nielsen, H. C., E. M. Wescott, G. Haerendel, and A. Valenzuela, Optical observations on the CRIT-II critical ionization velocity experiment, *Geophys. Res. Lett.*, 17, 1601, 1990b.
- Stenbaek-Nielsen, H. C., E. M. Wescott, and T. J. Hallinan, Observed barium emission rates, *J. Geophys. Res.*, 98, 17491, 1993.
- Stix, T. H., *Waves in Plasmas*. American Institute of Physics, New York, 1992.
- Swenson, C. M., *In situ observations of an ionospheric critical velocity experiment*, Ph.D. thesis, Cornell University, 1992.
- Swift, D. W., Use of a hybrid code to model the earth's magnetosphere, *Geophys. Res. Lett.*, 22, 311, 1995.
- Swift, D. W., Use of a hybrid code for global-scale plasma simulation, *J. Comput. Phys.*, 126, 109, 1996.
- Torbert, R. B., Review of critical velocity experiments in the ionosphere, *Adv. Space Res.*, 10(7), 47, 1990.
- Torbert, R. B., C. A. Kletzing, K. Liou, and D. Rau, Prompt ionization in the CRIT II barium releases, *Geophys. Res. Lett.*, 19, 973, 1992.

- Valenzuela, A., G. Haerendel, H. Föppl, F. Melzner, H. Neuss, E. Rieger, J. Stöcker, O. Bauer, H. Höfner, and J. Loidl, The AMPTE artificial comet experiments, *Nature*, 320(6064), 700, 1986.
- Wescott, E. M., E. P. Rieger, H. C. Stenbaek-Nielsen, T. N. Davis, H. M. Peek, and P. H. Bottoms, The L=6.7 quiet time barium shaped charge injection experiment "Chachalaca", *J. Geophys. Res.*, 80, 2738, 1975.
- Wescott, E. M., H. C. Stenbaek-Nielsen, T. Hallinan, H. Föppl, and A. Valenzuela, Star of Condor: a strontium critical velocity experiment, Peru, 1983, *J. Geophys. Res.*, 91, 9933, 1986a.
- Wescott, E. M., H. C. Stenbaek-Nielsen, T. Hallinan, H. Föppl, and A. Valenzuela, Star of Lima: overview and optical diagnostics of a barium Alfvén critical velocity experiment, *J. Geophys. Res.*, 91, 9923, 1986b.
- Wescott, E. M., H. C. Stenbaek-Nielsen, D. W. Swift, A. Valenzuela, and D. Rees, SR90, strontium shaped-charge critical ionization velocity experiment, *J. Geophys. Res.*, 95, 21069, 1990.
- Wescott, E. M., H. C. Stenbaek-Nielsen, D. L. Hampton, and P. A. Delamere, Results of critical velocity experiments with barium, strontium, and calcium releases from CRRES satellite, *J. Geophys. Res.*, 99, 2145, 1994.
- Wolf, P. H. and D. E. Hunton, Ionization mechanisms in CRRES chemical releases, 2. strontium photoionization and Ba^+ / Sr^+ collisional ionization cross section calculations, *submitted to J. Geophys. Res.*, 1997.
- Wright, A. N. and D. J. Southwood, Stationary Alfvénic structures, *J. Geophys. Res.*, 92(A2), 1167, 1987.
- Zaitsev, S. N., G. P. Milinevsky, and A. M. Evtushevsky, Simulation of the initial evolution of the CRRES G-9 barium release in the ionosphere, *J. Atmos. Terr. Phys.*, 58(16), 1895, 1996.

Zalesak, S. T., Fully multidimensional flux-corrected transport algorithms for fluids, *J. Comput. Phys.*, 31, 335, 1979.

IMAGE EVALUATION TEST TARGET (QA-3)



APPLIED IMAGE, Inc
1653 East Main Street
Rochester, NY 14609 USA
Phone: 716/482-0300
Fax: 716/288-5989

© 1993, Applied Image, Inc.. All Rights Reserved